HOLOGRAPHIC AUGMENTED REALITY

Towards Near-to-Eye Electroholography via Guided-Wave Acousto-Optics

by Sundeep Jolly

S.M., Media Arts and Sciences, Massachusetts Institute of Technology (2012)
M.S., Electrical and Computer Engineering, Georgia Institute of Technology (2009)
B.S., Physics, Georgia Institute of Technology (2008)
B.S., Electrical Engineering, Georgia Institute of Technology (2008)

Submitted to the Program in Media Arts and Sciences,
School of Architecture and Planning
in partial fulfillment of the requirements for the degree of

Doctor of Philosophy in Media Arts and Sciences

at the

MASSACHUSETTS INSTITUTE OF TECHNOLOGY

September 2019

Signature redacted

Author .....
Sundeep Jolly
Program in Media Arts and Sciences
School of Architecture and Planning
August 9, 2019

Signature redacted

Certified by .....
V. Michael Bove, Jr., Ph.D.
Principal Research Scientist
Thesis Supervisor
MIT Media Lab

Signature redacted

Accepted by .....
Tod Machover
Academic Head, Program in Media Arts and Sciences

HOLOGRAPHIC AUGMENTED REALITY

Towards Near-to-Eye Electroholography via Guided-Wave Acousto-Optics

by Sundeep Jolly

Submitted to the Program in Media Arts and Sciences,
School of Architecture and Planning
in partial fulfillment of the requirements for the degree of

Doctor of Philosophy in Media Arts and Sciences

at the Massachusetts Institute of Technology

ABSTRACT

Near-to-eye displays act to directly project imagery into a viewer's eye and can range in instantiation from extremely simple (such as an optical viewfinder) to more complex immersive displays for applications in virtual and augmented reality. Many current schemes for near-to-eye display employ stereoscopic techniques; however, such instantiations do not consistently present correct accommodation and vergence cues to the viewer, limiting their potential for seamless, comfortable augmented reality applications. Recent techniques based around light-field display methods show promise in the delivery of consistent depth cues although their applicability in presenting scenery with jointly high spatial and angular resolution is limited.

Electroholographic displays have been shown to provide the highest degree of visual realism and consistency amongst cues to depth relative to all competing technologies for 3-D display, and several recent instantiations based around pixelated spatial light modulators have shown their utility for near-to-eye display applications. However, constraints on available space-bandwidth product in such pixelated modulators limit the usable system étendue, resulting in reduced eyebox or field of view. In contrast, waveguide spatial light modulators offer the potential for displays with extremely high space-bandwidth product, compact form factors, and full-color operation via frequency-division multiplexing.

This dissertation aims to assess the feasibility of waveguide-based electroholography for near-to-eye augmented reality display. In particular, such feasibility is assessed through (1) a static set of near-to-eye holograms computed via iterative Fresnel domain techniques and fabricated via grayscale electron-beam lithography and (2) the design and analysis of a fully monolithic photonic platform for transparent, flat-panel holographic display requiring no supporting optics and implemented via anisotropic leaky-mode coupling in conjunction with integrated Bragg-regime diffractive combiner optics in lithium niobate. Furthermore, this dissertation presents a fabrication modality for multiscale, transparent, flat-panel holographic video displays based around femtosecond direct laser writing. Methods for and results in the integration of anisotropic waveguides, volume Bragg reflection holograms, and surface acoustic wave transducers in a lithium niobate substrate are depicted.

Thesis Supervisor: V. Michael Bove, Jr.
Title: Principal Research Scientist

This work has been supported in part by consortium funding at the MIT Media Laboratory and by Air Force Research Laboratory contract FA8650-14-C-6571.

HOLOGRAPHIC AUGMENTED REALITY
Towards Near-to-Eye Electroholography via Guided-Wave Acousto-Optics

by Sundeep Jolly

The following person served as a reader for this thesis:

Reader ... Signature redacted .....

Daniel Smalley, Ph.D.
Assistant Professor of Electrical and Computer Engineering
Department of Electrical and Computer Engineering
Brigham Young University

HOLOGRAPHIC AUGMENTED REALITY
Towards Near-to-Eye Electroholography via Guided-Wave Acousto-Optics

by Sundeep Jolly

The following person served as a reader for this thesis:

Signature redacted

Reader . . . . . .

Bahram Javidi, Ph.D.
Professor of Electrical and Computer Engineering
Department of Electrical and Computer Engineering
University of Connecticut

ACKNOWLEDGMENTS

This dissertation is the culmination and synthesis of several years of ideas and efforts, and I owe special thanks to so many who have helped along the way:

My advisor, Michael Bove, for providing me with the opportunity to come to the Media Lab, the freedom to explore new (sometimes crazy) ideas, and all of the guidance along the way.

To my committee members, Prof. Bahram Javidi and Prof. Daniel Smalley, for their careful mentorship and feedback on the ideas presented in this thesis and elsewhere.

Kristin Hall, for keeping Object-Based Media running smoothly and always being willing to help.

Linda Peterson, for always providing a helping hand and open ear and making sure that all of us in MAS are well taken care of.

MAS staff - including Keira Horowitz, Monica Orta, and Amanda Stoll - for all of the support.

The staff of the MIT Nanostructures Laboratory and the Microsystems Technology Laboratory (especially Mark Mondol and Jim Daley), for all the of guidance and technical help with micro- and nano-fabrication.

The Mazur Lab at Harvard University, for lending expertise and equipment that helped to lay the foundation for the explorations in this thesis.

The Center for Bits and Atoms (especially Prashant Patil, Will Langford, Thras Karydis, and Neil Gershenfeld) for the technical know-how and assistance with bringing up the laser micromachining system.

The Camera Culture group (especially Ramesh Raskar, Gordon Wetzstein, Achuta Kadambi, Genzhi Ye, Barmak Heshmat, and Matt Hirsch), for the fruitful collaborations and lots of fun late-night chats about imaging.

The Object-Based Media Group (Santiago, David, Dan N., Ali, Everett, Andrew, Pedro, Vik, Emily, and Carol), for being an especially invigorating group to be around and learn from.

James Barabas and Daniel Smalley, for being great mentors on the holovideo project and friends.

Pip Mothersill, for all of the wonderful chats about life over cocktails.

Laura Perovich, for all of the sagely advice and willingness to always provide a much-needed dose of perspective.

Ermal Dreshaj, for all the help with algorithms and long talks about life.

Ayush Bhandari, for always providing a useful sanity check and refreshing perspective on work and life, the inspiration on many ideas around signals and imaging, and all of the long walks around Boston and coffee breaks at Tatte.

Karthik Dinakar, for being not only a technical inspiration but also like a brother.

Edwina Portocarrero, for always being relentlessly supportive, the many long late-night chats over dinners, and all of the incredible memories.

Bianca Datta, for the infectious positivity, always being willing to find cheese, and being one of the best people I've ever had the privilege of calling my friend.

Jin Joo Lee, for being one of my closest friends for over 22 years and for always reminding me of my roots.

And finally, to my family, for their unwavering support throughout my academic endeavors.

CONTENTS

LIST OF FIGURES

1

INTRODUCTION & BACKGROUND

Near-to-eye displays act to directly project imagery into a viewer's eye and can range in instantiation from extremely simple (such as an optical viewfinder) to more complex immersive displays for applications in virtual reality. Although they are sometimes found in monocular configurations for display of two-dimensional imagery, near-to-eye displays often aim to recreate three-dimensional imagery for a viewer, typically through stereoscopic [1] or other multiscopic means (*e.g.*, multifocal or light-field [2] displays). Like all 3-D display systems, near-to-eye 3-D display systems need to meet the challenge of displaying imagery such that viewers correctly and comfortably perceive 3-D scenery. In addition, near-to-eye 3-D displays additionally have to be designed for maximal viewer comfort and preferably in such a manner that limits bulkiness and weight. Historically, near-to-eye 3-D displays have been implemented using techniques such as stereo disparity (employing simple magnifiers) [1], although more complex schemes for near-to-eye display based around lenticular imaging [2, 3] or factored light-field techniques [4] have recently emerged.

1.1 HUMAN FACTORS CONSIDERATIONS IN NEAR-TO-EYE DISPLAY DESIGN

Depth perception in the human visual system relies jointly on monocular cues – such as occlusion and linear perspective – and binocular cues, principally motion parallax, accommodation, vergence, and binocular disparity. Disparity refers to the notion that each of the left and right eyes image a slight horizontally offset version of the same scenery, with the offset dependent on distance from the viewer. Parallax refers to the notion of experiencing different vantage points of a 3-D scene with movement. Taken together, disparity and parallax can be used to create compelling 3-D experiences for users (e.g., ZSpace Motion Displays [5]), although accommodation-vergence mismatches as described below limit their potential in several application scenarios.

1.1.1 *Accommodation*

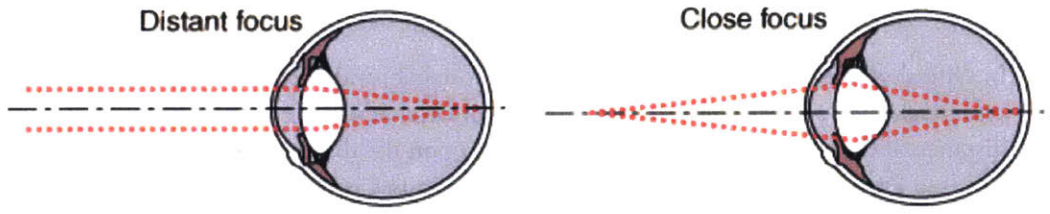

Figure 1: Adapted from [6]. Accommodation in the human eye. Ciliary muscles act to stretch or compress the flexible ocular lens to adjust its optical power for varying focal distances. For instance, focusing on distant objects or at infinity necessitates a low optical power and ciliary muscles stretch the lens; similarly, focusing on closer objects necessitates higher optical power and ciliary muscles act to contract the lens.

Accommodation refers to the ability of the human eye to adjust the optical power of its lens via the action of ciliary muscles in response to the environment (see Fig. 1). As a principal cue to depth, accommodation (in conjunction with stronger cues to depth) allows for some degree of depth perception, especially for objects at close distances (i.e., < 1 m) to the eye. However, the range of available optical powers is constrained by physiological limitations and therefore objects in close proximity to the eye (i.e., outside the *accommodation range*) are perceived as defocused by a viewer.

Unlike other displays, near-to-eye displays face a particular challenge because of the accommodation range of the human eye. This means that, e.g., unaided microdisplays, cannot be resolved by the human eye at very close distances unless supporting optics are used. Simple lenses have often been used in conjunction with microdisplays to create virtual images at focus planes falling at resolvable accommodation distances from the eye (see Fig. 2 (a), in which a magnified virtual image is created at a longer distance from the eye than the microdisplay); however, magnification of pixelated displays creates undesirable image artifacts due to decreased spatial resolution.

Near-to-eye 3-D displays based on stereoscopic principles, such as the consumer-grade Oculus Rift and Microsoft's Hololens, typically deal with accommodation range issues via the use of simple magnifiers. More complex near-to-eye 3-D displays (usually based around light field reconstruction principles) act to create the appearance of a virtual scene at scene distances that are resolvable by the eye via integral imaging [2, 3] or compressive display [4] techniques, regardless of the actual distance of the display system to the eye.

1.1.2 *Vergence*

Vergence refers to the triangulation, or inward and outward rotational motion between both eyes when viewing an object at some distance away in order to maintain binocular vision. For instance, the inward rotation of both eyes is small for distant objects (and zero for extremely distant objects or for a focus at "infinity") and becomes progressively larger for closer objects. Because the vergence angle necessarily maps to object depth, it is a prominent cue to depth. In most ordinary viewing situations (i.e., for natural reality), accommodation is directly coupled to vergence.

1.1.3 *Accommodation-Vergence Conflicts in 3-D Display*

In typical glasses-bound stereoscopic, autostereoscopic, and automultiscopic displays, the *accommodation-vergence conflict* refers to the notion that a viewer's eyes are focused at the distance of the screen while they are converged upon the distance to an apparent 3-D object (see Figs. 3 and 4 (a)). This mismatch often causes issues such as visual discomfort, fatigue, and distorted depth perception for the viewer [7]. In many current see-through near-to-eye displays for augmented reality applications, there exists an accommodation-vergence mismatch between the real-world scenery and the displayed imagery (which is typically presented on a flat 2-D surface) [3]. The viewer is often made to accommodate on displayed imagery and also to accommodate and converge upon objects in reality (see Fig. 4 (b)). This is typically difficult because the accommodation distances of the displayed imagery and the object in reality are far apart such that simultaneous accommodation on

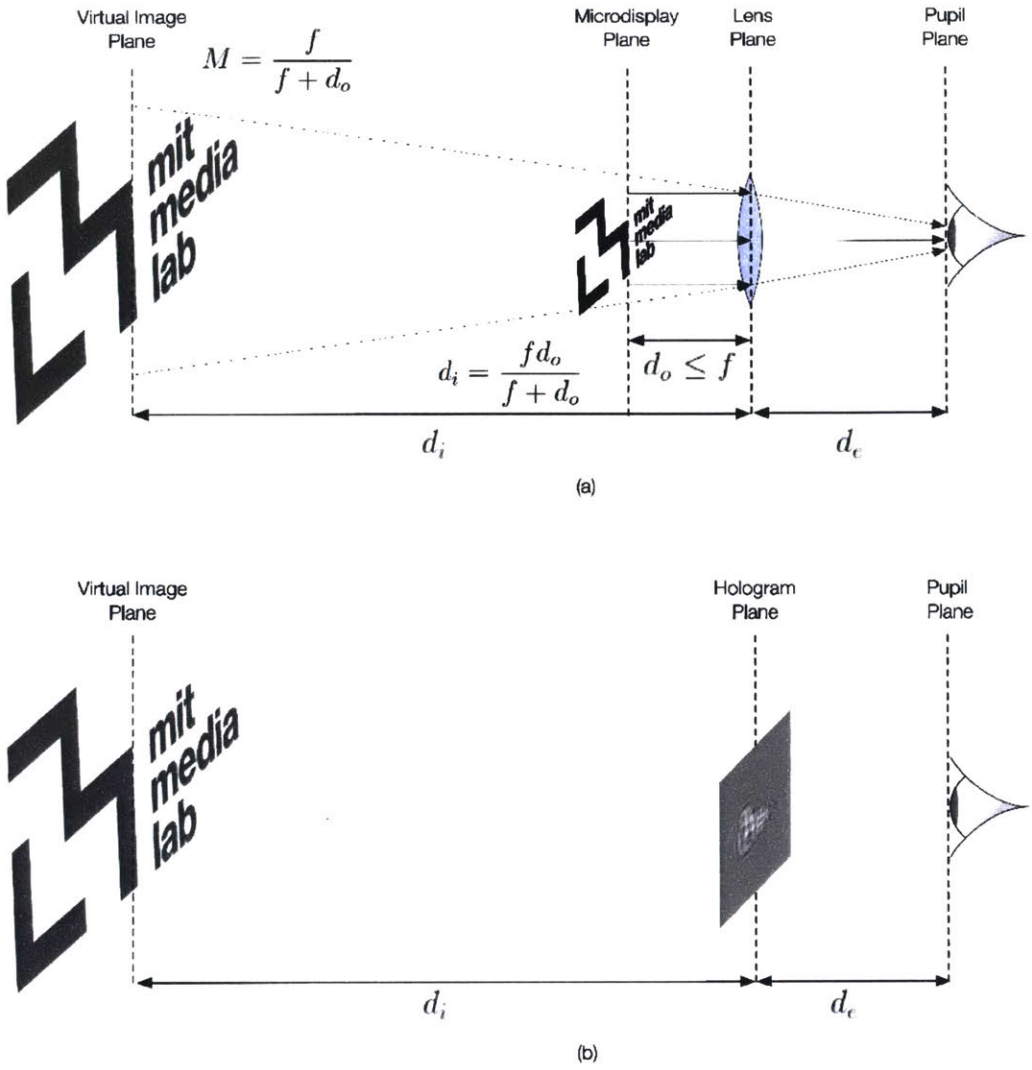

Figure 2: Virtual image formation in microdisplay-based near-to-eye displays and holographic near-to-eye displays. (a) Virtual image generation from a microdisplay via a simple lens. Light rays reflected off a microdisplay located at distance $d_e + d_o$ from the eye are incident upon a plano- or bi-convex lens located at d_e from the eye (*i.e.*, eye relief distance), which acts to create a magnified virtual image of the microdisplay at a distance $d_i + d_e$ from the eye, where $d_i = f d_o / (f + d_o)$ and the magnification is $M = d_i / d_o = f / (f + f_o)$. While the original distance of the microdisplay $d_e + d_o$ is not within the accommodation range of the eye, the virtual image distance $d_i + d_e > d_o + d_e$ does fall within the accommodation range and the virtual image is therefore resolvable. (b) Virtual image generation from a near-to-eye hologram. The hologram itself recreates a wavefront of the desired image plane at an perceived image distance $d_i + d_e$ from the eye, without the need for any additional optics. Note that the distance of the virtual image from the eye falls within the accommodation range and the virtual image is therefore resolvable.

both is impossible. For stereoscopic displays, a viewer focusing at the plane of the display will perceive all imagery – regardless of the apparent distance intended – as being in focus [8]. In addition to an accommodation-vergence mismatch, the utility of accommodation for depth perception – a moderately strong cue for objects closer than 1 m to the

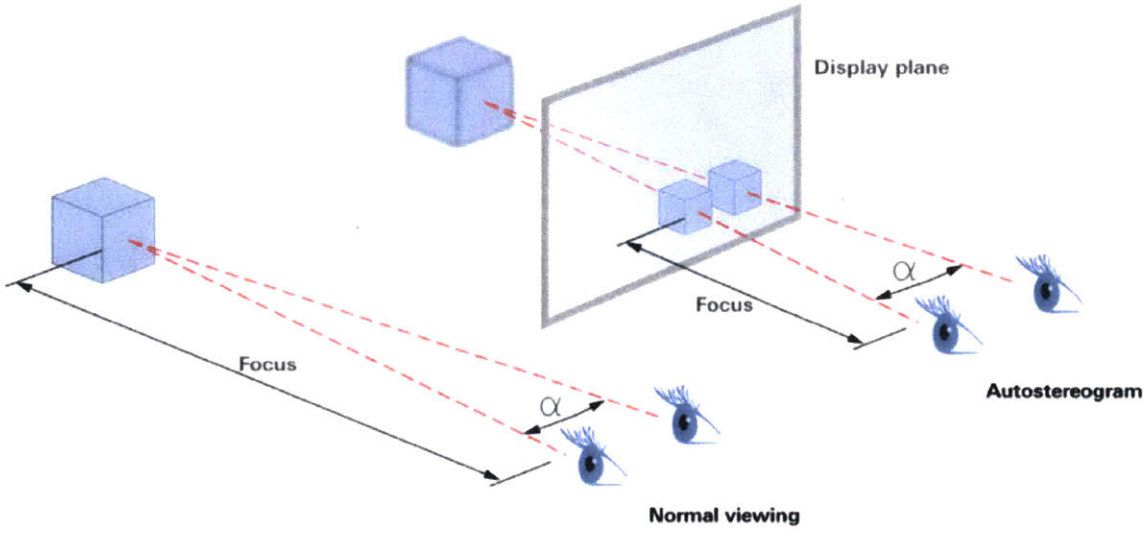

Figure 3: Adapted from [7]. (a) Matched accommodation and vergence distances in normal viewing, in which a viewer's eyes are both made to focus and converge at the distance to a real object. (b) Accommodation-vergence mismatch in a typical autostereogram, in which a viewer's eyes are made to focus at the physical screen distance but converge upon the apparent location of an object.

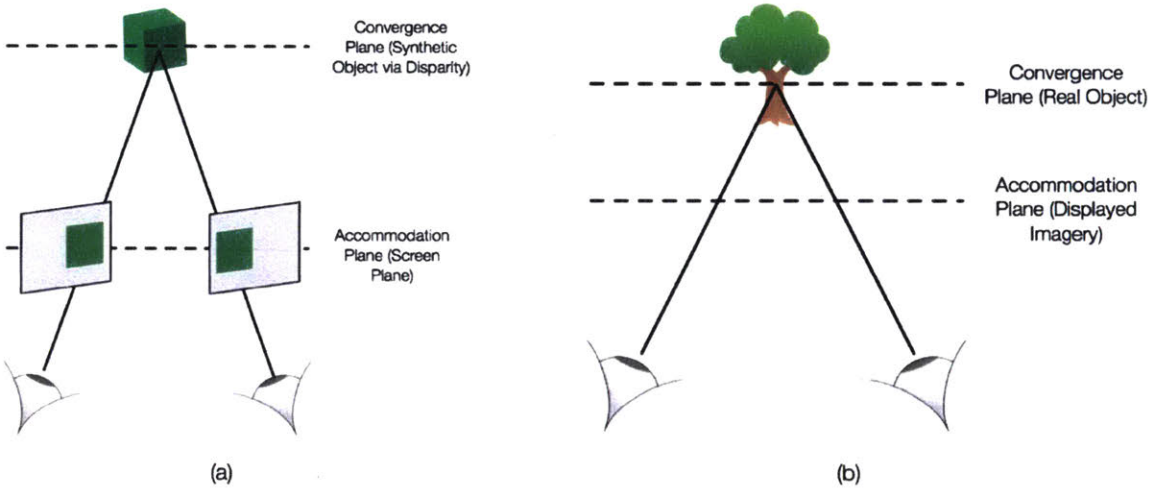

Figure 4: Accommodation-vergence mismatch scenarios in near-to-eye augmented reality displays. (a) Accommodation-vergence mismatch resulting from the display of synthetic 3-D imagery by presenting disparate views to both of the left and right eyes, in which the eyes are forced to accommodate on the screen plane but converge upon the apparent depth of the synthetic 3-D object. (b) Accommodation-vergence mismatch between, *e.g.*, a displayed 2-D plane of imagery at some apparent depth and a real-world object, in which the eyes are forced to accommodate on the displayed plane of imagery but converge upon the perceived depth of the real-world object.

eye – is greatly diminished in this situation.

Unlike other displays, near-to-eye displays additionally face a particular challenge because of the accommodation range of the human eye. This means that, *e.g.*, unaided microdisplays, cannot be resolved by the human eye at very close distances unless supporting optics are used. Simple lenses have often been used in conjunction with microdisplays to create virtual images at focus planes falling at resolvable accommodation distances from the eye (see Fig. 2 (a), in which a magnified virtual image is created at a longer distance from the eye than the microdisplay); however, magnification of pixelated displays creates undesirable image artifacts due to decreased spatial resolution.

1.2 TECHNIQUES FOR NEAR-TO-EYE 3-D DISPLAY

Immersive near-to-eye displays block out normal reality and are therefore appropriate for application in virtual reality whereas see-through near-to-eye displays act to augment a viewer's normal viewing of reality with overlaid content.

1.2.1 *Binocular Stereoscopic Display*

Stereoscopic 3-D displays rely principally on binocular disparity, and in some instantiations, motion parallax, to deliver the perception of depth to a viewer. Binocular stereoscopic display systems are typically implemented via microdisplays or LCD panels [9] in conjunction with magnifying lenses. Consumer products such as the Oculus Rift [10] employ basic stereoscopic principles in order to create the illusion of depth in displayed 3-D scenes and therefore suffer from accommodation-vergence mismatches common to stereoscopic 3-D displays [8].

1.2.2 *Binocular Light Field Display*

Light field display systems act to reconstruct plenoptic functions [11] (i.e., the set of all rays and associated intensities, typically as a function of spatial position, polar angles, and wavelength) corresponding to 3-D scenes for a viewer. Typical implementations include parallax-barrier and integral imaging display setups [12]. Light field display systems typically offer some subset of cues to depth for a 3-D viewer – principally vergence, motion parallax, and binocular disparity – and some recent light-field displays offer consistent accommodation cues, either via super-multiview [13] or compressive techniques [4, 14]. Recently, near-to-eye instantiations of light field displays have been demonstrated to mitigate vergence-accommodation problems associated with stereoscopic near-to-eye displays. These instantiations include prototypes based upon integral imaging techniques for immersive [2] and see-through [3] display and multi-layered LCD panels [4].

1.2.3 *Holographic Display*

Holographic display systems act to reconstruct light wavefronts emanating from 3-D scenes for a viewer and are naturally capable of handling all principal cues to depth – accommodation, vergence, motion parallax, and binocular disparity – in a visually and perceptually consistent manner [15]. Such affordances are principally due to the wavefront reconstructing nature of holography, thereby presenting all spatial and angular information of 3-D scenes. Fig. 5 depicts a general pipeline for holographic video display systems, comprised of 3-D data sourcing, computation pipelines, light modulation, and light processing [16].

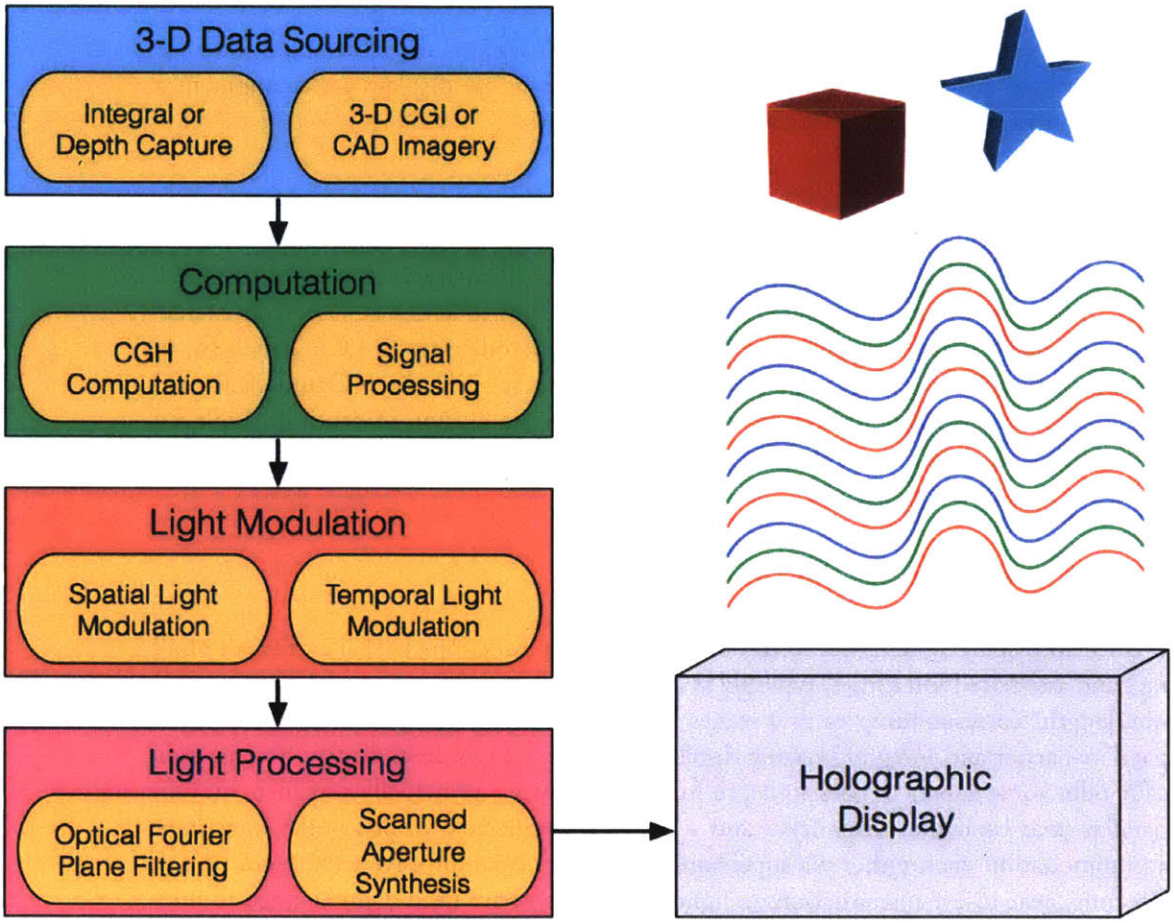

Figure 5: General pipeline for a holographic video display system.

Recent work has shown the potential of holographic display technologies in improving perceptual performance over competing techniques for 3-D display [17]. Because of naturally-matched accommodation and vergence cues and high reconstruction fidelity with correct or near-correct wavefront curvature, holography is well-poised as a contender for future near-to-eye 3-D displays.

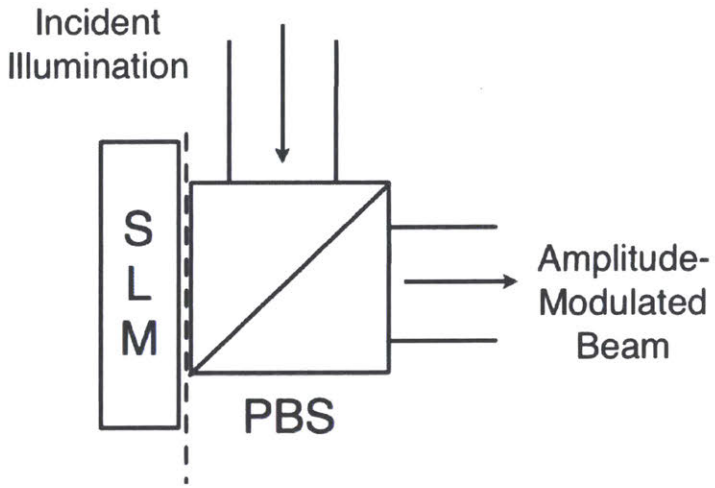

Figure 6: Architecture for LCoS-based holographic display.

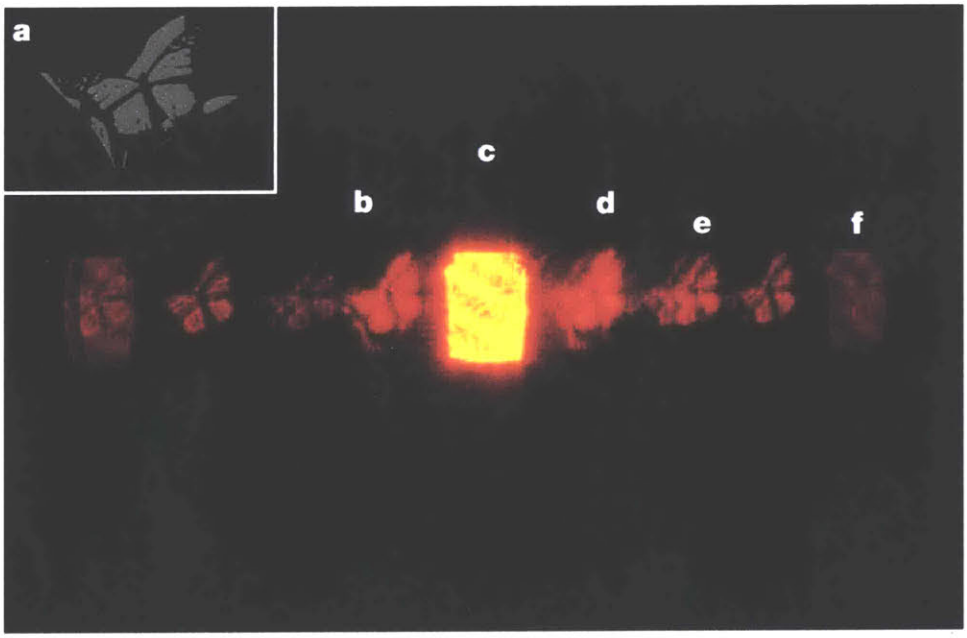

Figure 7: Adapted from [18, 19]. Artifacts in an LCoS-based holographic display system.

Holographic video display systems are built around spatial light modulators, which act to modulate either the amplitude or phase of light in some degree of partial coherence. Typically, such modulators are composed of discrete pixels (such as liquid-crystal-on-silicon – LCoS – modulators or digital micromirror devices). A typical scheme for LCoS-based light modulation is shown in Fig. 6, in which incident laser light is spatially modulated in

amplitude via the use of a polarizing beamsplitter. Because pixelated spatial light modulators diffract in the Raman-Nath regime, many diffractive orders in addition to the desired diffractive reconstruction order are formed as shown in Fig. 7, including conjugate orders, orders due to hologram quantization, and orders due to the pixelated microstructure of the spatial light modulator [19]. Additionally, such architectures are often limited in either field of view, spatial extent, or both due to the limited space-bandwidth product available to such modulators (this is discussed in detail in Section 1.4 below). Holographic display architectures based around acousto-optic modulators, including the MIT Mark I and Mark II systems [20], have employed scanned-aperture holography [21] in using the high temporal bandwidth of AOMs in combination with persistence of vision to increase the effective spatial extent and field of view of holographic displays.

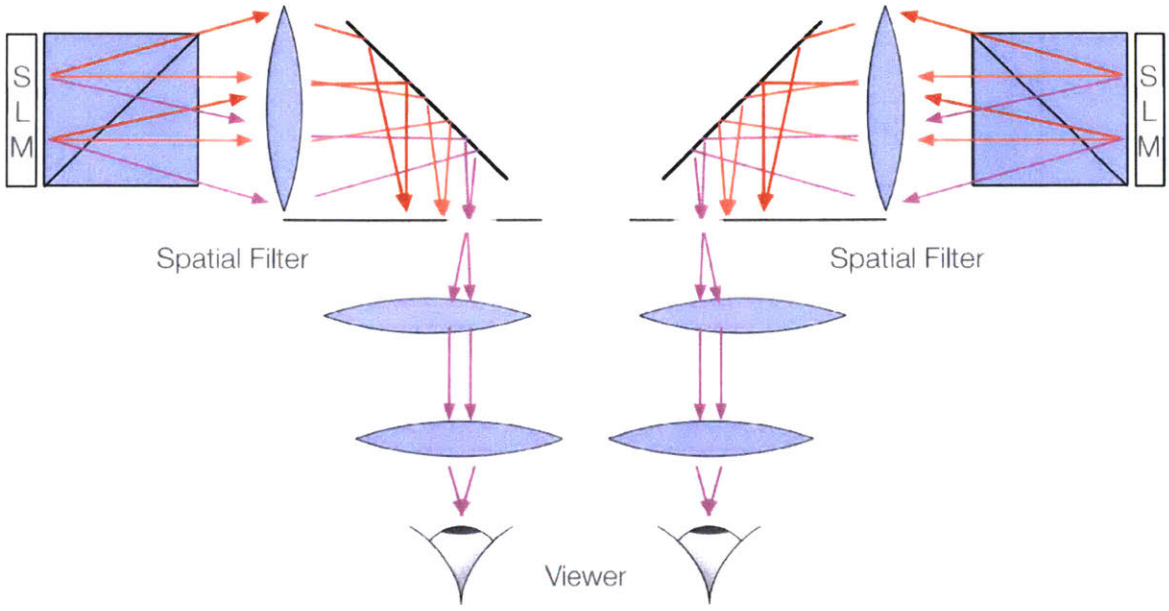

Figure 8: Sample architecture for LCoS-based see-through holographic display, in which the modulated light from a pixelated spatial light modulator is demagnified through an optical telescope and then viewed through a field lens. Ambient light passes through the optical path via a beamsplitter.

Recently, several groups have investigated the potential of holographic displays for near-to-eye display applications in virtual and augmented reality. Recent work by Hong, *et. al.* [22] and Moon, *et. al.* [23] has investigated the use of de-magnified, relayed images of LCoS spatial light modulators (see Fig. 8) for near-to-eye electroholography. Ambient light enters the optical path through a transparent beamsplitter and the final output is viewed through a field lens. Although this architecture is intuitive, constraints on the size of the usable eyebox, field of view, and overall bulkiness of the system limit the potential of the system in a headset application.

Other groups have investigated near-to-eye holographic displays via the use of light diffracted from pixelated spatial light modulators relayed through a transparent waveguide system (see Fig. 9). In such an approach, phase-modulated light from the Fresnel diffracted field of the displayed computer-generated hologram on the LCoS microdisplay encounters a volume reflection Bragg grating that acts to couple the light into a transparent waveguid-

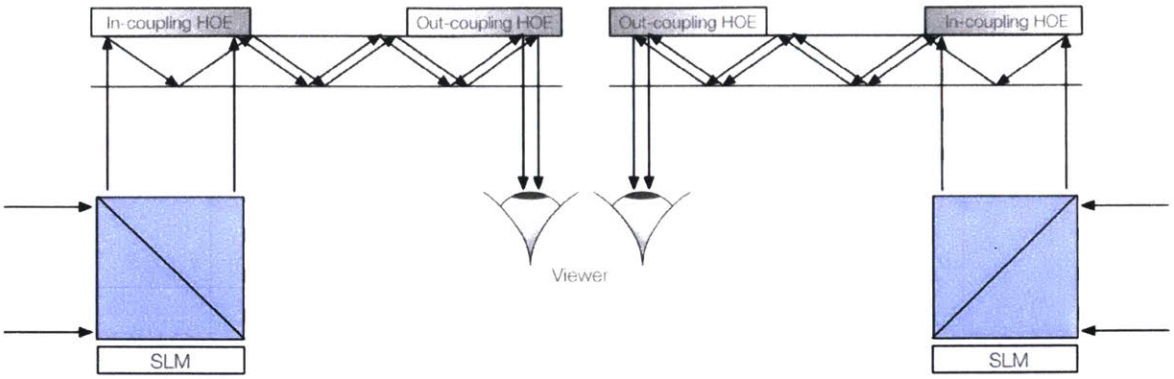

Figure 9: Adapted from [24]. Architecture for LCoS-based see-through holographic display, in which the modulated light from a pixelated spatial light modulator is relayed into a transparent waveguide via a volume holographic in-coupling grating. The light propagates down the guide until encountering a second volume holographic grating, which outcouples the light from the waveguide into the viewer's eye.

ing layer. The modulated, guided light then propagates through the waveguide until encountering a second volume reflection Bragg grating that acts to outcouple the light from the waveguide into a viewer's eye. These so-called holographic waveguides are transparent to the ambient light, and due to the fact that the coupling gratings operate in the Bragg regime, the ambient light is unaffected as it passes through the grating. In particular, Yeom *et. al.* employed this approach with an LCoS spatial light modulator alongside correction for possible astigmatic focusing introduced by the volume holographically-recorded coupling gratings [24].

In order to deliver a convincing and comfortable experience for the viewer of a near-to-eye 3-D display, all cues to depth should be presented in a visually consistent manner in order to minimize viewer discomfort and fatigue. In particular, near-to-eye 3-D displays face the unresolved challenge of minimizing the accommodation-vergence mismatch in order to maximize viewer comfort and minimize fatigue. Furthermore, ensuring proper placement of virtual scenery or augmented information at depth planes in order to satisfy the accommodation limits of the human visual system (while retaining small and lightweight form factors for the overall head-mounted unit) poses an additional challenge. Light field and holographic display techniques are well-poised to meet the challenges posed by delivering 3-D imagery to a viewer by a near-to-eye display; future advancements in these display techniques can reasonably be expected to help near-to-eye 3-D displays develop into a mature, market-ready technology.

1.3 SPACE-BANDWIDTH PRODUCT CONSIDERATIONS

The *space-bandwidth product* of a spatial light modulator dictates the achievable angular field-of-view and spatial extent for the output of a holographic video display built upon it. Briefly, this unitless number is typically a function of the number of pixels and the pixel pitch (which dictates the maximal diffracted angle, as mapped from maximal spatial frequency as $\theta_{max} = \sin^{-1}(f_{max}\lambda)$, where λ is the operating wavelength) for a pixelated spatial light modulator (such as an LCoS or DMD device) or a function of the temporal operating bandwidth for an analog acousto-optic modulator. Alternatively, one can consider directly the space-bandwidth required of a holographic display to support a viewing

configuration for a given viewer-display distance, viewer rotation angle, and desired field of view [26].

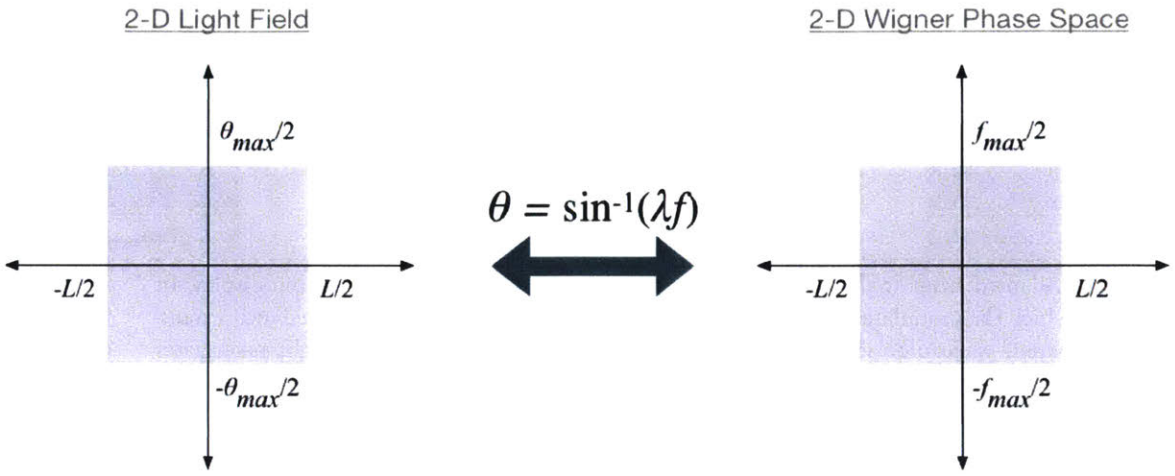

Figure 10: 2-D light field distribution and 2-D Wigner distribution function for a space-bandwidth product of a 1-D holographic line.

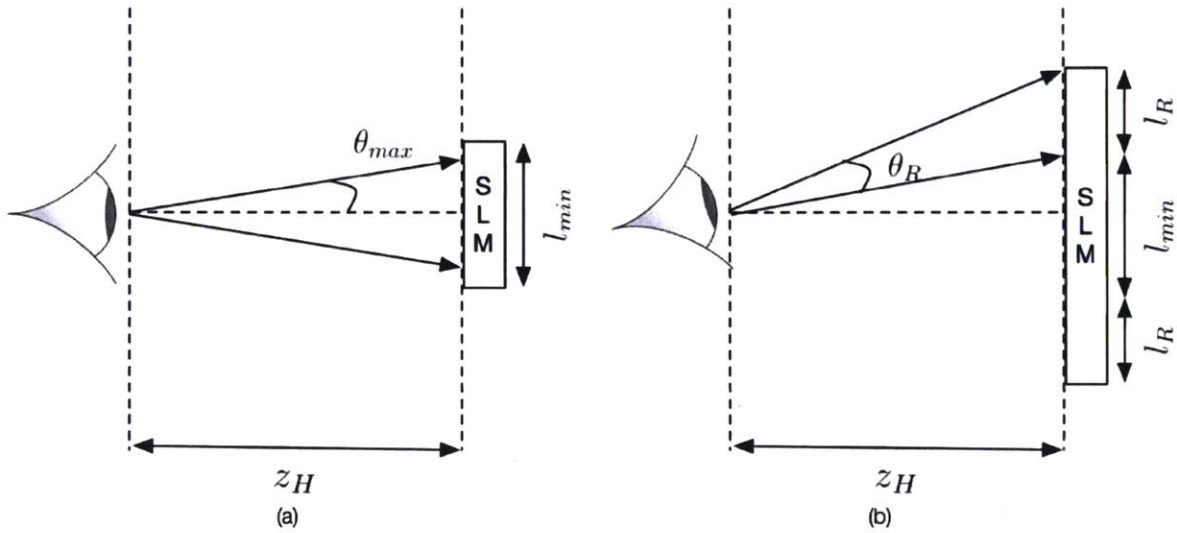

Figure 11: Adapted from [26]. Diagram depicting spatial and angular considerations on the requisite space-bandwidth product for a holographic display. (a) Spatio-angular diagram for a non-translating, non-rotating viewer. z_H is the distance of the spatial light modulator from the eye, l_min is the minimum required spatial extent of the spatial light modulator, and θ_{max} is the first order, half-cone maximal diffracted angle from the spatial light modulator (or equivalently, the ocular field of view). (b) Spatio-angular diagram for a non-translating, rotating viewer. l_R is the additional required spatial extent of the spatial light modulator given an eye rotation angle of θ_R.

In order to illustrate possible space-bandwidth product requirements of a near-to-eye holographic video display, we consider a field of view of 3°, which is consistent with the field of view in which retinal resolution is highest (*i.e.*, observations are made with *foveal acuity*) [27]. We also consider only the case in which the viewer can rotate but not translate laterally or axially relative to the display plane (*e.g.*, the eye can rotate but will be fixed both

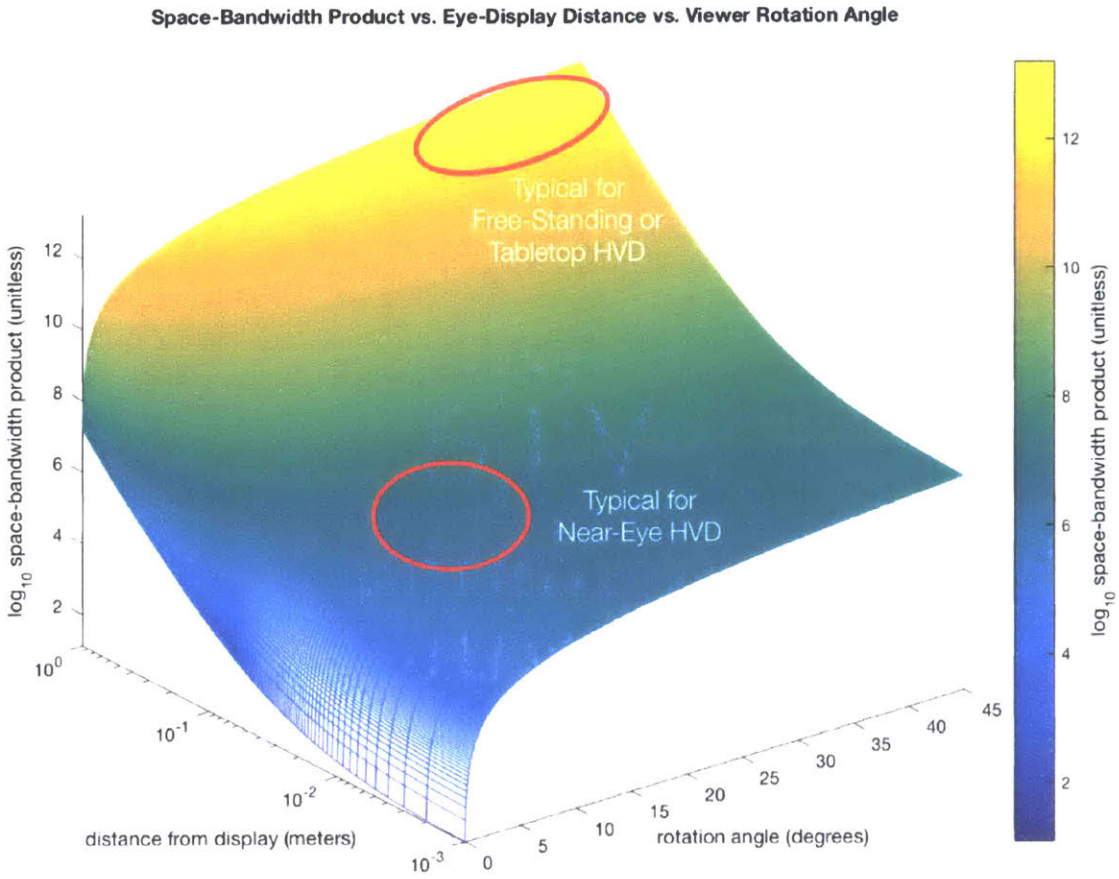

Figure 12: Space-bandwidth product (base-10 logarithm) as a function of eye-display distance (*i.e.*, eye relief) and viewer rotation angle for a fixed field of view $\theta_{max} = 3°$ and operating wavelength $\lambda = 600$ nm. Note that for a typical free-standing holographic video display located at close to 1 m from a viewer with an allowable viewer rotation of up to 45°, the SBP approaches values in excess of 10^{13}. However, for a typical near-to-eye instantiation of a holographic video display with an eye relief distance of approximately 15 mm and eye rotation angle of 15°, the SBP takes values between 10^7 and 10^8 – several orders of magnitude lower than that for a typical free-standing HVD.

laterally and axially relative to a head-mounted display) – this scenario is depicted in Fig. 11. Following the analysis in Onural *et. al.* [26], the total 1-D spatial extent of a spatial light modulator located a distance z_H away from a viewer (in the near-to-eye case, the eye) with an ocular field of view of $\theta_{max} = 3°$ and allowable eye rotation angle $\theta_R = 15°$ can be found as

$$l_{total} = 2z_H \tan(\theta_{max} + \theta_R) \tag{1}$$

and the maximal spatial frequency required for that ocular field of view and allowable eye rotation angle can be found as

$$f_{max} = \frac{\sin(\theta_{max} + \theta_R)}{\lambda} \tag{2}$$

where λ is the operating wavelength. For the two-dimensional case, the spatial extent becomes a circle of diameter l_{total} in the spatial domain and the bandwidth becomes a

circle of diameter $2f_{max}$ in the Fourier domain. Then, the 2-D space-bandwidth product is found as

$$SBP = \left[\pi\left(\frac{l_{total}}{2}\right)^2\right] \times \left[\pi\left(\frac{2f_{max}}{2}\right)^2\right] = \left[\frac{\pi z_H \sin(\theta_{max}+\theta_R)\tan(\theta_{max}+\theta_R)}{\lambda}\right]^2 \quad (3)$$

This expression is plotted against eye-display distance and viewer rotation angle in Fig. 12 for a fixed field of view $\theta_{max} = 3°$ and operating wavelength $\lambda = 600$ nm. Highlighted are regions of interest for typical near-to-eye holographic video displays and typical free-standing or tabletop holographic video displays. Note that the SBP requirement is mitigated from upwards of 10^{13} for a free-standing HVD to 10^7 for a near-to-eye instantiation – and thereby reveals that the problem of near-to-eye holographic video display – while perhaps not trivially easy – is considerably more manageable, from a light-modulation and computational perspective, relative to that of free-standing or tabletop HVDs.

Fig. 13 depicts the space-bandwidth product given in Eq. 3 as a function of field of view angle θ_{max} for a fixed eye relief distance $z_H = 15$ mm and maximal eye rotation angle $\theta_R = 15°$. While still remaining relatively manageable (in an order-of-magnitude sense), the SBP requirement increases monotonically for increasing field of view. One can therefore conclude that the most immersive near-to-eye holographic experiences will therefore require increased capability – both from a light-modulation and computational perspective – and that FOV should be an important consideration in the design of near-to-eye HVDs.

1.4 WAVEGUIDE HOLOGRAPHY AND WAVEGUIDE ELECTROHOLOGRAPHY

Waveguide holography typically refers to the use of holographic techniques for the control of guided-wave light in integrated optical devices (*e.g.*, grating couplers and distributed Bragg gratings for guided-wave optical filtering) and for general control of guided-wave light via diffraction. Image display via optically-recorded waveguide Bragg holograms has been explored [28,29]. Furthermore, computer-generated waveguide holography (CGWH) has been demonstrated for the generation of free-space spot arrays and for the integrated implementation of several optical functions [30]. Additionally, holographic optical elements have been used for near-to-eye wearable displays for the incoupling of microdisplay-modulated light into guided-wave modes and for the outcoupling of that light towards a viewer [31]; however, such displays rely on waveguide and holographic coupling techniques to relay the light from a microdisplay to a viewer and do not provide holographic imagery directly to a viewer.

Recently, a waveguide-based platform for acousto-optic spatial light modulation for holographic video displays has emerged [18,19] and shows several notable advantages over more conventional techniques for spatial light modulation for holographic video displays, such as the potential for no quantization noise or undesired diffracted orders upon reconstruction and full-color imagery via frequency-division mutliplexing (see Fig. 14). Although this modulation scheme has only to-date been demonstrated in a conventional scanning-type holographic display (see Fig. 15), the underlying surface acoustic wave technology

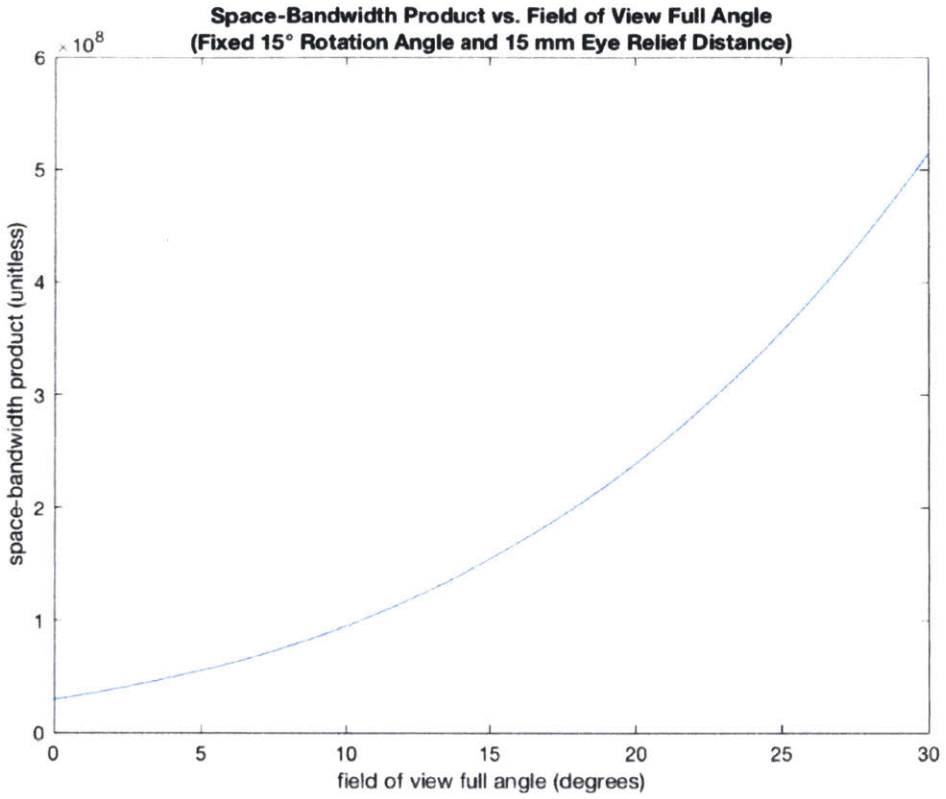

Figure 13: Space-bandwidth product as a function of field of view angle θ_{max} for a fixed eye relief distance $z_H = 15$ mm and maximal rotation angle of 15° (typical for most viewers). For more immersive applications requiring wide fields of view, SBP can increase by over an order of magnitude over a case in which field of view is limited to that of maximal retinal resolution for foveal acuity.

can be extended to support a display requiring no additional supporting optics, effectively operating as a transparent, flat-panel holographic display.

It should be noted that acousto-optic spatial light modulators of this type have an extremely high space-bandwidth product relative to pixelated spatial light modulators because of their inherently analog nature. As an example, a 1080p LCoS spatial light modulator that can be driven at a 60 Hz update rate can support up to 125 million pixels per second of information. In contrast, a guided-wave acousto-optic modulator driven with an analog signal having a 400 MPixel/s pixel clock can support 400 million pixels per second, and driven in parallel with, e.g., 50 channels on the same substrate, can support upwards of 20 billion pixels per second. This extremely high space-bandwidth product can allow for viewing geometries simultaneously supporting large eyeboxes and large fields-of-view.

1.5 MOTIVATION

The extremely high space-bandwidth product offered by guided-wave acousto-optic spatial light modulators, in addition to their other advantages for use in diffractive displays, make them an attractive candidate for use as transparent, flat-panel holographic displays (see Fig. 16). One such approach has already been depicted by Henrie *et. al.*, to use a leaky-

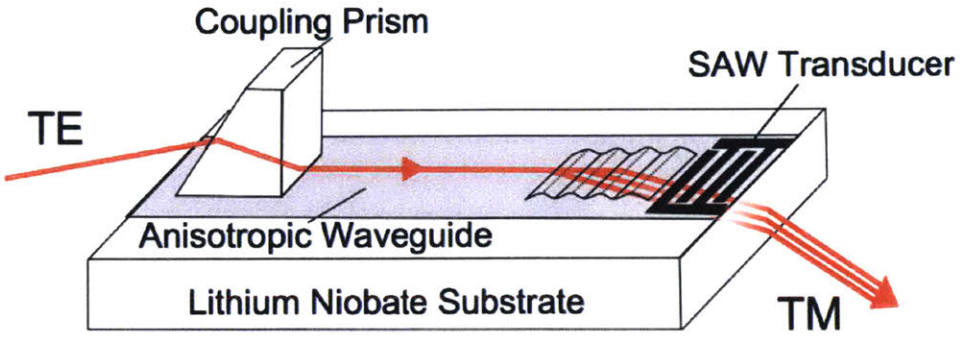

Figure 14: Adapted from [18, 19]. Structure of an anisotropic leaky-mode modulator, in which guided-mode light interacts with and is modulated by a nearly-collinear propagating surface acoustic wave containing holographic information. The interaction forces the guided-mode light to outcouple from the waveguide into a leaky-mode, which is then used as the spatially modulated light in a holographic display optical system.

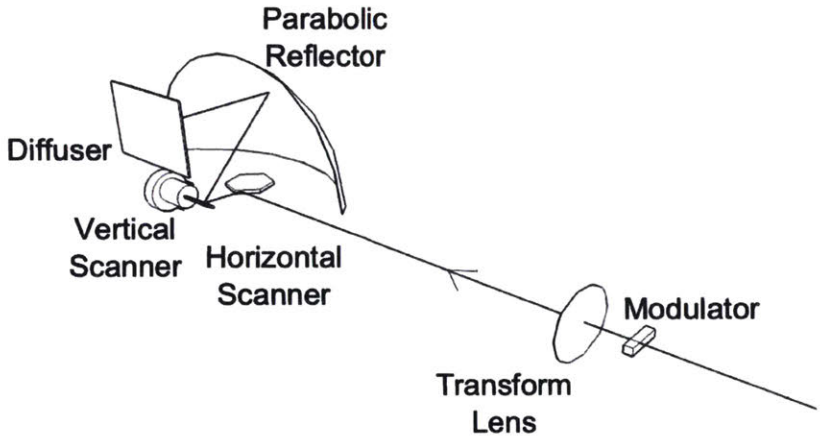

Figure 15: Adapted from [18, 19]. Modified Scophony optical geometry employed in the MIT Mark IV holographic display system.

Figure 16: Simulated depiction of holographic near-to-eye display requiring no supporting optics.

mode modulator in conjunction with a surface outcoupling grating to direct the otherwise edge-emitting light to a viewer through the back face of the monolithic device [?]. This dissertation aims to assess the feasibility of waveguide-based electroholography for transparent, flat-panel augmented reality display. In particular, such feasibility is assessed through (1) a static set of near-to-eye holograms computed via iterative Fresnel domain techniques and fabricated via grayscale electron-beam lithography and (2) the design and analysis of a fully monolithic photonic platform for transparent, flat-panel holographic display requiring no supporting optics and implemented via anisotropic leaky-mode coupling in conjunction with integrated volume Bragg-regime diffractive combiner optics (in contrast to surface gratings) in lithium niobate. Furthermore, this dissertation presents a fabrication modality for multiscale, transparent, flat-panel holographic video displays based around femtosecond direct laser writing.

1.6 RESEARCH QUESTIONS AND CONTRIBUTIONS

Having established a motivation for employing waveguide holography for near-to-eye augmented reality display and assessed the feasibility of such a solution from the perspective of the space-bandwidth product, this thesis aims to address the following research questions in support of future near-to-eye holographic video display solutions based around waveguide holography for augmented reality applications:

- How does one effectively compute holograms for the near-to-eye instantiation, given the limitations of the human visual system and the considerations on space-bandwidth product resulting from near-to-eye placement?
- How does one design a transparent, flat-panel near-to-eye holographic video display requiring no supporting optics or discrete microdisplays?
- What can rapid prototyping techniques such as femtosecond laser direct writing offer with respect to fabrication modalities for scalable integrated optics for transparent, flat-panel holographic video displays?

To address these questions, this thesis presents the following *contributions* in support of a near-to-eye holographic video display solution:

- An implementation and analysis of static computer-generated waveguide holograms for transparent, flat-panel holographic display fabricated via electron-beam lithography.
- A design and analysis of a surface acoustic wave device for guided-wave diffraction capable of operating as a scalable platform for transparent, flat-panel holographic video display.
- A rigorous model of end-to-end optical field transformations in such an implementation of near-to-eye transparent, flat-panel holographic video displays.
- Methods for and results in the application of femtosecond laser direct writing towards the goal of scalable, transparent, flat-panel holographic video displays based around guided-wave acousto-optics.

This document is organized as follows:

- Chapter 2 depicts the design and implementation of a static computer-generated waveguide hologram for transparent, flat-panel image holography.
- Chapter 3 depicts the design of a guided-wave acousto-optic device implemented in lithium niobate capable of operating as a scalable platform for transparent, flat-panel holographic video display.
- Chapter 4 depicts a fabrication methodology for rapid prototyping of such the depicted integrated optic device based around femtosecond laser micromachining in lithium niobate.
- Chapter 5 depicts modeling and simulation methodology and results for the collinear guided-to-leaky acousto-optic mode conversion of holographically modulated light in proton-exchanged and laser-written waveguides in lithium niobate. Additionally, it depicts design, modeling, and simulation methodology and results for volume Bragg reflection gratings in lithium niobate implemented via femtosecond laser micromachining.
- Chapter 6 depicts systems engineering considerations for the use of the aforementioned guided-wave acousto-optic device as a transparent, flat-panel holographic display, including simulated results relating to the use of strobed-source illumination.
- Chapter 7 depicts computational considerations and architectures for the use of the depicted guided-wave device as a transparent, flat-panel holographic display, especially considerations around efficient subsampling and modulation schemes for full-color displays via frequency-division multiplexing.
- Chapter 8 depicts current results in the integration and fabrication of anisotropic waveguides, volume Bragg holograms, and surface acoustic wave transducers in lithium niobate via femtosecond laser micromachining.
- Chapter 9 lays out a path forward for scalability and integration of the depicted methods for use in transparent, flat-panel electroholography for both near-to-eye and desktop-class applications and presents conclusions about the current work.

2

STATIC COMPUTER-GENERATED WAVEGUIDE HOLOGRAPHY

The information presented in this chapter draws from work initially presented in Sundeep Jolly, Nickolaos Savidis, Bianca Datta, V. Michael Bove, Jr., and Daniel Smalley, "Progress in off-plane computer-generated waveguide holography for near-to-eye 3D display," Proc. SPIE Practical Holography XXX: Materials and Applications, 9771, 2016. [32].

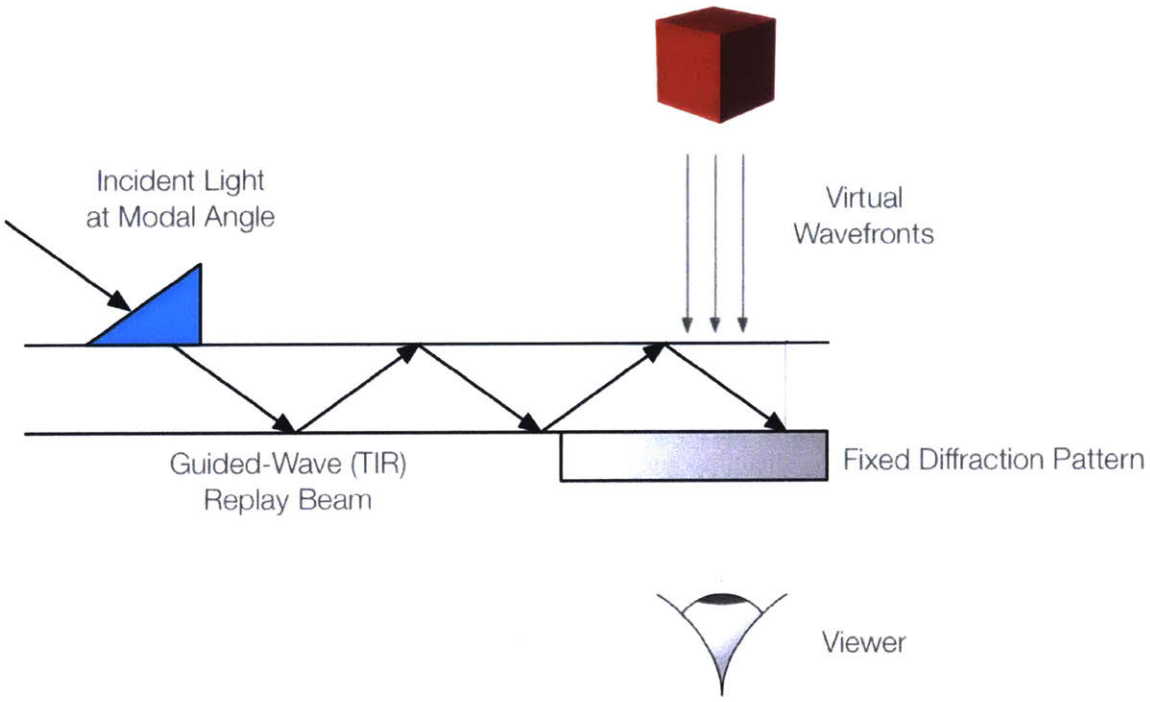

Figure 17: Static waveguide hologram geometry for replay and reconstruction.

Having established basic feasibility of near-to-eye holographic video display from the perspective of the space-bandwidth product, this chapter examines techniques for static, waveguide-based computer-generated holography for near-to-eye display. The schematic for the target device structure and function is depicted in Fig. 17.

2.1 FRESNEL HOLOGRAM COMPUTATION

For the purposes of the current experiment, the computer-generated holograms we employ are computed such that the displayed output consists of a 2-D plane of imagery. This geometry is depicted in Fig. 18.

The computation scheme employs the Fresnel-transforming Gerchberg-Saxton method for phase-only hologram computation [33]. This algorithm produces a phase-only CGH pattern that generates a desired plane of imagery at some distance from the hologram plane. A single loop of this iterative process is depicted in Fig. 19. Briefly, the iteration

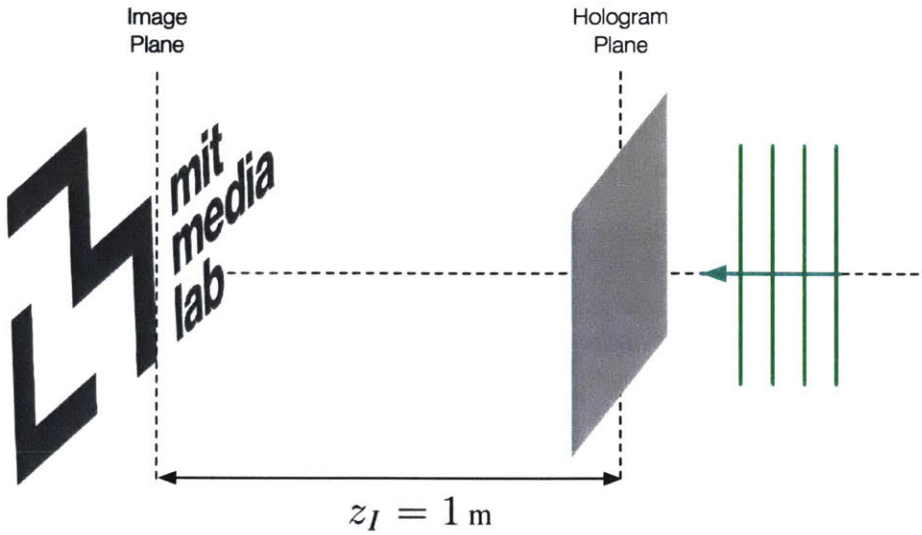

Figure 18: Diffraction geometry used in generating the CGH pattern. Assuming planar input illumination, the Fresnel field at the hologram plane is enforced to be phase-only via the Gerchberg-Saxton algorithm. The desired imagery is generated at a distance z_I from the hologram plane.

loop begins with a complex field consisting of a randomly-initialized phase pattern having unit amplitude. This phase pattern is Fresnel transformed to yield the propagated field at the image plane. The Fresnel field arriving at the image plane is Fresnel transformed via the 2-D Fresnel diffraction integral:

$$U_o(x,y,\Delta z) = \frac{e^{jk\Delta z}}{j\lambda\Delta z} e^{\frac{jk}{2\Delta z}(x^2+y^2)} \int_{Y'}\int_{X'} U_i(x',y')\, t(x',y') \, e^{\frac{jk}{2\Delta z}(x'^2+y'^2)} e^{-\frac{j2\pi}{\lambda\Delta z}(xx'+yy')} dx'dy' \quad (4)$$

where $U_o(x,y,\Delta z)$ is the Fresnel field arriving at the hologram plane, $U_i(x,y)$ is the plane wave illumination field with form $U_p(x,y) = A_0 \exp(jk\phi_0)$, $t(x,y)$ is the amplitude transmittance function of the diffracting aperture (*i.e.*, the planar image), $k = 2\pi/\lambda$ is the wavenumber, Δz is the propagation distance, (x,y) are the spatial coordinates at the output plane, and (x',y') are the spatial coordinates at the input plane [34]. This integral is evaluated as a discrete Fourier transform using the Fast Fourier Transform algorithm.

At this point, the first estimate of the approximated intensity profile at the image plane is found via the squared-modulus of the complex Fresnel field at the image plane. On subsequent iteration loops, this estimate is compared to the desired image reconstruction and the results of comparison are used as a basis for ending the optimization (*i.e.*, $||I_{desired} - I_{estimate}||_2^2 < \epsilon$, where $I_{desired}$ is the intensity profile of the desired 2-D imagery, $I_{estimate}$ is the approximated intensity profile arriving at the image plane via Fresnel transform of the optimized phase CGH pattern, $||\cdot||_2^2$ indicates the square of the ℓ-2 norm, and ϵ is a small error threshold). If the criterion for ending the optimization is not met, the target intensity is used to amplitude-enforce the Fresnel field at the image plane (*i.e.*, the square root of the target intensity is set to be the new amplitude) and that field is inverse Fresnel-transformed to find the complex Fresnel field arriving at the hologram

plane. In order to meet fabrication constraints, the number of allowable phase levels is set to 8 and the constrained phase profile is the resulting phase CGH after an iteration. On a new iteration, the constrained phase profile is equalized with a unit-amplitude plane wave and that complex field is the input for a Fresnel transform again to the image plane. Here, another image comparison takes place.

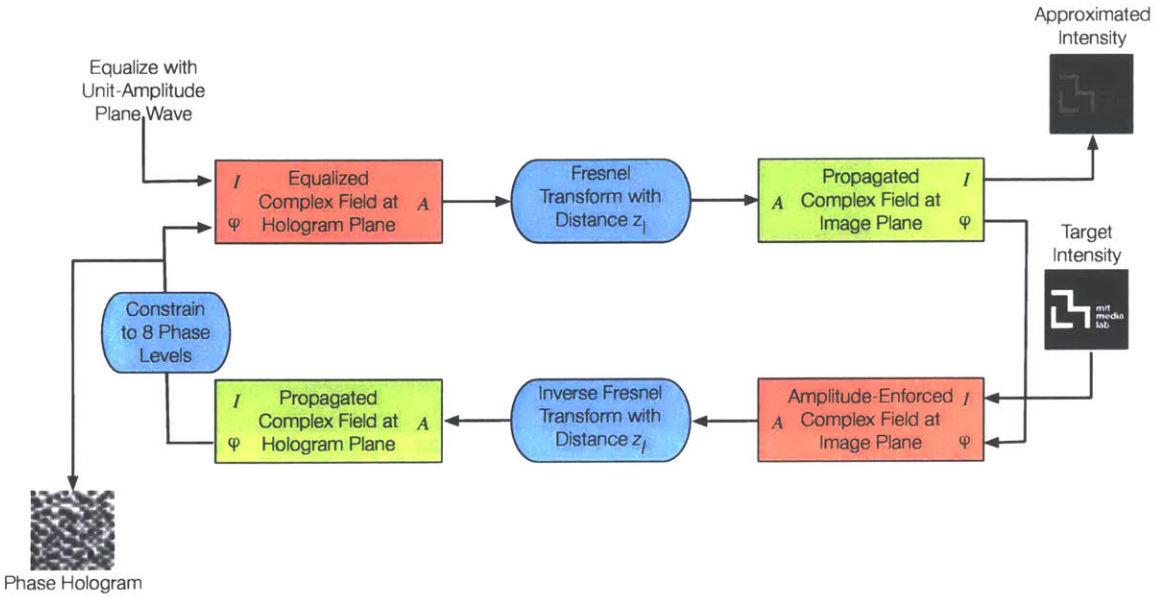

Figure 19: Iteration loop for phase-only CGH computation via the Fresnel-transforming Gerchberg-Saxton method. Beginning with a random phase profile with unit amplitude, this complex hologram is Fresnel transformed to find the complex field arriving at the image plane. The intensity profile is compared with the desired imagery, and if the error criterion is not satisfied, the iteration loop continues as the target imagery is used to amplitude-enforce the Fresnel field at the image plane. The field is then inverse Fresnel-transformed to find the field at the hologram plane. After constraining the phase-profile to 8 phase levels, the resulting phase-only CGH is equalized with a unit-amplitude plane wave and a new iteration loop begins.

Using target imagery of the MIT Media Lab logo, the Fresnel-transforming Gerchberg-Saxton algorithm was employed over 50 iterations. The resulting phase CGH profile and approximated intensity arriving at the image plane are depicted in Figs. 20 and 21.

2.2 FABRICATION: RAMAN-NATH CGH VIA ELECTRON-BEAM LITHOGRAPHY

In order to prototype computer-generated waveguide holograms for near-to-eye applications, the approach presented here employs electron-beam lithographic techniques to fabricate phase-retarding diffractive patterns in PMMA on quartz substrates. Fig. 22 depicts a typical fabrication process for such a prototype. After beginning with a quartz (SiO_2) substrate, 600 nm poly(methyl methacrylate) (PMMA) is spin-coated on and post-baked. In order to avoid charging of the substrate via the electron-beam write process, 10 nm of chrome is deposited on top of the PMMA via evaporation. Using an Elionix ELS-F125 electron-beam lithography system operating at 125 KeV and employing a beam current of 100 nA, the grayscale phase CGH is written in the PMMA with a base dose of 1400

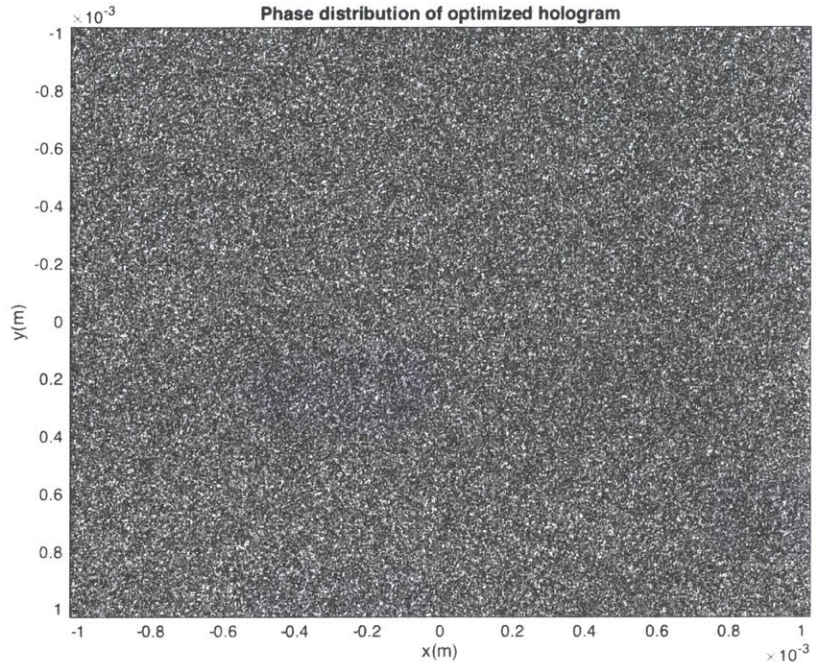

Figure 20: Optimized phase profile at hologram plane after 50 iteration of the Fresnel-transforming Gerchberg-Saxton algorithm with desired imagery of the MIT Media Lab logo.

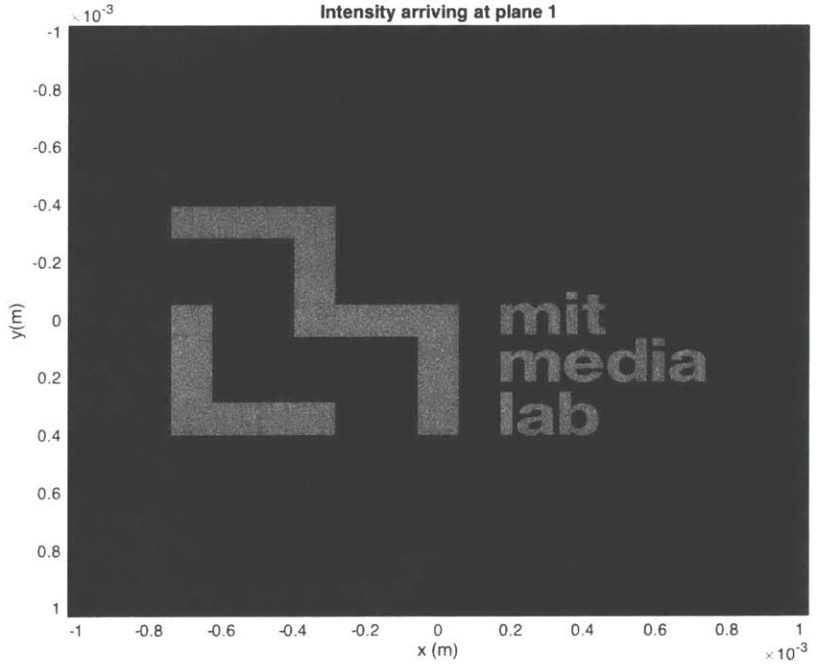

Figure 21: Approximated intensity of the MIT Media Lab logo arriving at the image plane after Fresnel-transforming the optimized phase profile in Fig. 20 found after 50 iterations of the Fresnel-transforming Gerchberg-Saxton algorithm.

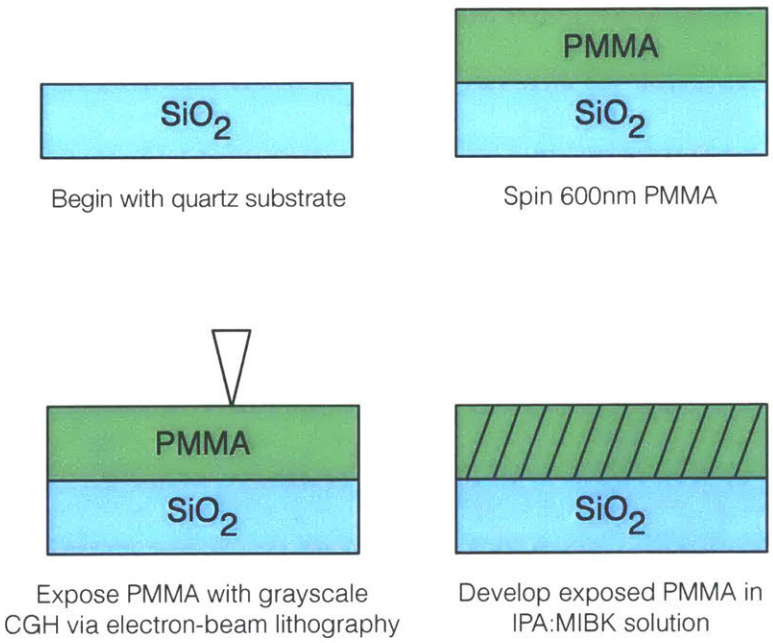

Figure 22: Fabrication process for a static off-plane computer-generated waveguide hologram. (a) Single-crystal quartz or fused silica is used as the substrate. (b) 600 nm of PMMA is deposited via spin-coating and post-baking. (c) The PMMA is exposed via grayscale electron-beam lithography. (d) The exposed PMMA is developed in an IPA:MIBK solution.

$\mu C/cm^2$ (note the actual dosage varies from that base dose according to the gray level of the phase CGH). The chrome layer is removed via a chrome etchant and the exposed PMMA is developed in a solution of 4:1 isopropanol:methylisobutylketone for 30 s. An SEM image of a portion of an example written CGH in PMMA on top of silicon is shown in Fig. 23.

The replay process for the written computer-generated waveguide holograms is depicted in Fig. 24. Briefly, laser light is edge-coupled into the quartz substrate onto which the CGH is written at an angle higher than the critical angle for the air-quartz interface (for single crystal quartz with $n = 1.54$, $\theta_c = \sin^{-1}(1.00/1.54) \approx 40.49°$). By definition, the quartz substrate acts as a multi-modal waveguide and confines the illumination light via total internal reflection. When the totally internally reflected light encounters the written CGH, it is outcoupled in a similar manner to waveguided light that encounters a grating outcoupler. The CGH acts as a Fourier sum of many single-frequency grating outcouplers and is therefore well-suited to outcouple (and spatially phase modulate) the guided light. The diffracted light from the CGWH then propagates away from the device for viewing.

Fig. 25 depicts the edge-coupled laser light in the quartz substrate, the outcoupling via the CGH towards a screen, and the formation of strongly-scattered diffracted orders. Note that this diffraction results from a non-image forming CGH and is intended to depict the outcoupling performance of a CGWH. Fig. 26 depicts the optical reconstruction of the phase CGH depicted in Fig. 20. Aside from some strong zero-order diffracted scatter, the reconstruction presents good discriminability and verifies the computational and fabrication processes.

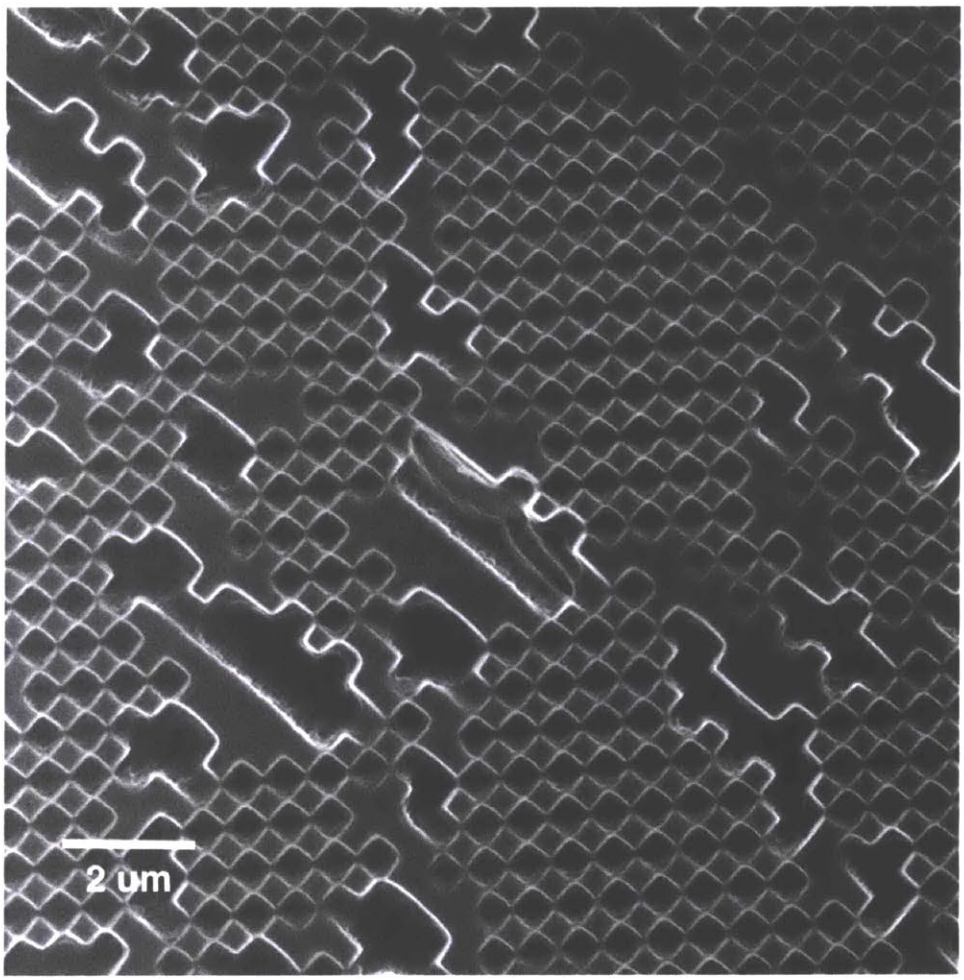

Figure 23: Scanning electron micrograph of a sample lithographed phase-only CGH in PMMA resist on silicon substrate. Square pixels are 500 nm in dimension.

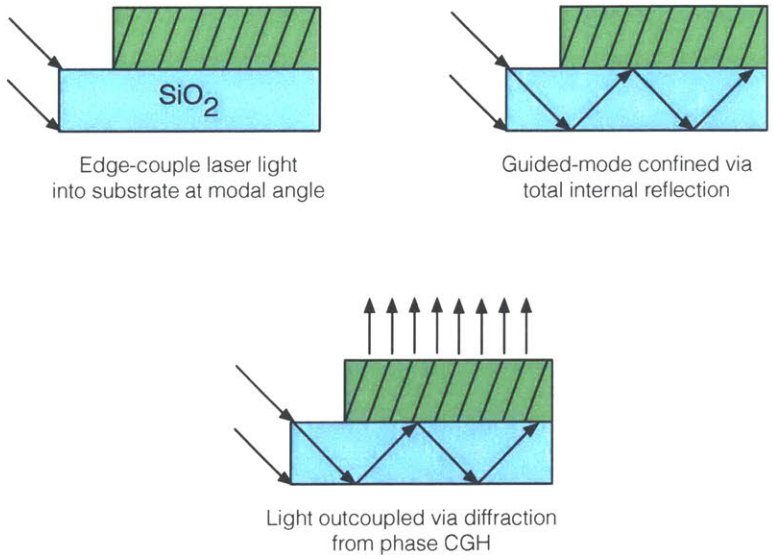

Figure 24: Replay process for a static off-plane computer-generated waveguide hologram. (a) Laser light is edge-coupled into the glass substrate at an angle higher than the critical angle. (b) The coupled light is confined into a guided-mode via total internal reflection. (c) The coupled light encounters the CGH and is outcoupled from the substrate and modulated with the holographic information, enabling reconstruction.

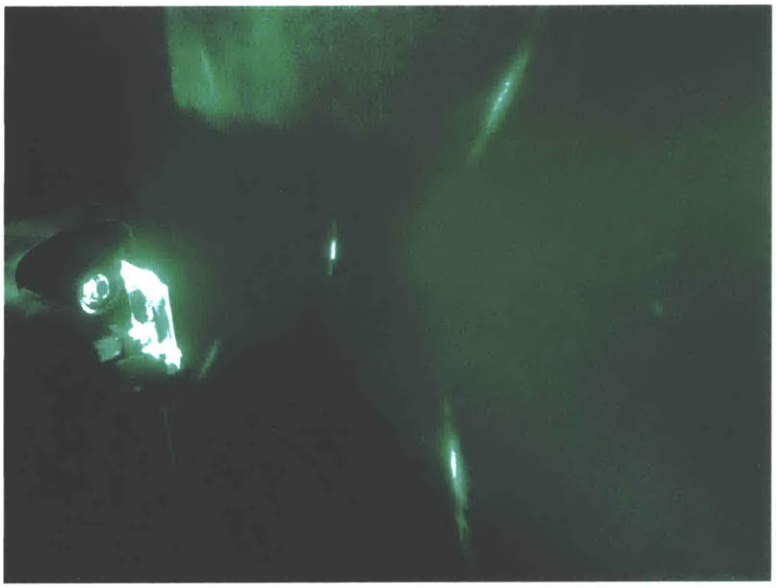

Figure 25: Diffractive outcoupling from edge-lit computer-generated waveguide hologram, depicting total internal reflection of edge-coupled illumination light and the formation of strongly-scattered diffracted orders on a screen.

Figure 26: Diffractive reconstruction of phase-only CGH computed using the Fresnel-transforming Gerchberg-Saxton algorithm and fabricated in PMMA on a quartz substrate via e-beam lithography.

3

NEAR-TO-EYE ELECTROHOLOGRAPHY VIA GUIDED-WAVE ACOUSTO-OPTICS: OPTICAL PRINCIPLES

The information presented in this chapter draws from work initially presented in Sundeep Jolly, Nickolaos Savidis, Bianca Datta, Daniel Smalley, and V. Michael Bove, Jr., "Near-to-eye electroholography via guided-wave acousto-optics for augmented reality," Proc. SPIE Practical Holography XXXI: Materials and Applications, 10127, 2017 [35].

Near-to-eye *electroholography* refers to the creation of dynamic, three-dimensional imagery for a single viewer via the use of a head-mounted display system that reconstructs light wavefronts via diffraction. As of the time of this writing, only a very small number of such systems have been prototyped, all of which reconstruct imagery via the use of a single [36] or binocular pair [22–24, 30] of pixelated spatial light modulators. Furthermore, while some investigations into optimizing optical geometries for near-to-eye holographic display systems [30] and optimizing computational techniques for the generation of CGHs for near-to-eye display geometries [22], the generation of near-to-eye holographic displays with large space-bandwidth product, large field of view, and high visual acuity has so far been limited. Furthermore, recent advances in integrated optics for holographic video displays [18, 19] have not yet been investigated for their potential in near-to-eye display scenarios.

The system explored in this thesis employs a guided-wave acousto-optic platform implemented in lithium niobate ($LiNbO_3$) in order to realize a fully-monolithic, transparent, flat-panel holographic video display. Such a system can be viewed as the direct dynamic analog of aforementioned waveguide holograms for static display [29, 37].

3.1 BASIC OPTICAL PRINCIPLES

The optical design utilizes several concepts that have already been explored in other contexts: (1) the use of anisotropic guided-wave acousto-optics for spatial light modulation in holographic video displays [18, 19] via a guided-to-leaky mode transition in birefringent $LiNbO_3$ [38, 39], (2) the use of a Bragg grating to introduce illumination into a waveguide [41], (3) the use of beam strobing in order to "freeze" the acousto-optic pattern and eliminate the need for de-scanning the propagating acoustic wave [42], and (4) the use of a volume holographic Bragg reflection grating in order to reflect the leaky diffracted toward a viewer with high efficiency [44, 45]. Note that all elements – including the in-coupling grating, anisotropic waveguide, and output volume hologram – can be realized within a single $LiNbO_3$ substrate without the need for any additional supporting optics. Therefore, the proposed platform provides a path towards a fully monolithic, integrated optic platform for transparent holographic video display for near-to-eye display.

Figs. 27 and 28 depicts the basic structure of the proposed guided optical wave surface acoustic device. Note that for x-cut $LiNbO_3$, the z-axis is the extraordinary axis. The incident light is linearly polarized in the TE orientation and is reflected off a surface Bragg grating which couples it into the anisotropic waveguide. The waveguide has an extraor-

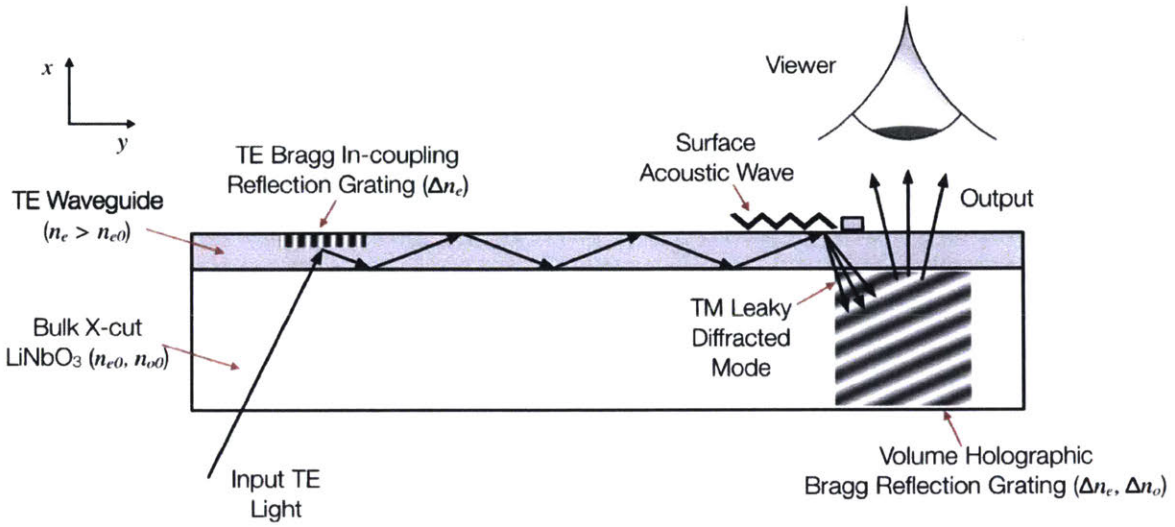

Figure 27: $x - y$ cross-section (side view) of proposed guided optical wave SAW device with integrated Bragg gratings.

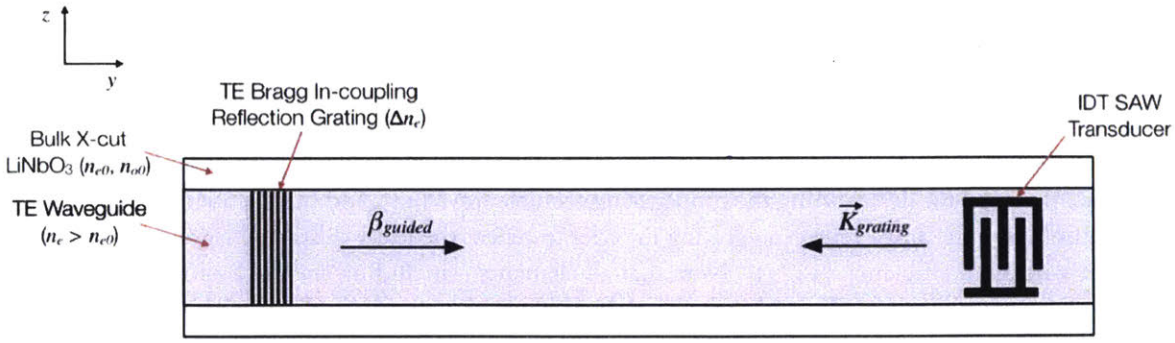

Figure 28: $z - y$ cross-section (top view) of SAW Device. For x-cut uniaxial $LiNbO_3$, the z-axis is the extraordinary axis.

dinary index perturbation of Δn_e relative to the substrate but no ordinary index change. When excited by an RF signal containing the holographic information, the interdigitated electrodes (pictured in Fig. 28) launch a surface acoustic wave. The guided-mode light interacts with the SAW and is mode-converted into a diffracted TM mode which exits the waveguide as a leaky mode. Upon entering the substrate region, the leaky mode is incident upon a reflection mode volume holographic Bragg grating with grating vector nearly parallel to the center wavevector of the incident leaky mode's angular fan. Due to the volume hologram's wide angular acceptance range (see the analysis in Chapter 5 and Fig. 57 in particular), the leaky mode is reflected to exit the substrate through the waveguide towards the viewer. In Fig. 28, β_{guided} is the propagation constant of the guided-mode TE light in the waveguide and $\overrightarrow{K}_{grating}$ is the acoustic grating's wavevector. Note that established frequency-division mutliplexing schemes for full-color operation [18, 19] can similarly be applied to the depicted device (this is expounded upon in Ch. 8). It should also be noted that the device depicted here can also be operated for use in a scanning retinal display [46].

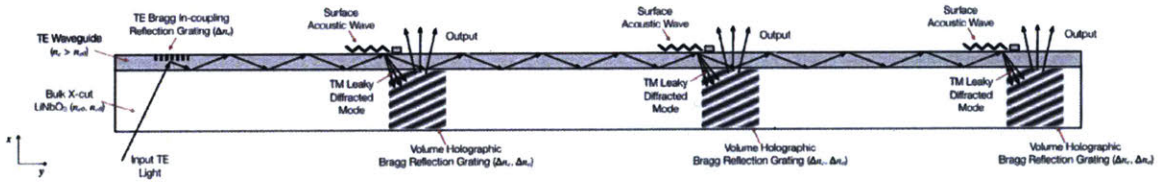

Figure 29: $x - y$ cross-section (side view) of multi-element SAW device.

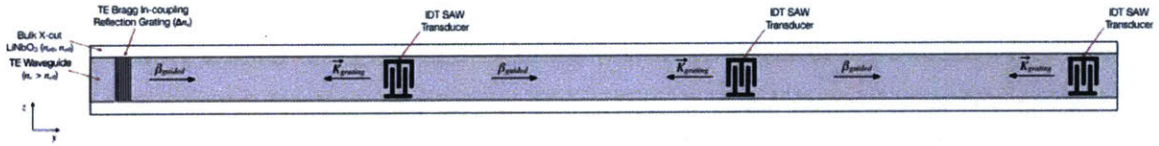

Figure 30: $z - y$ cross-section (top view) of multi-element SAW Device.

The integrated optic device depicted here can be employed for the generation of both real and virtual image points via the use of positively or negatively chirped acoustic gratings. This functionality is depicted in Fig. 31.

Note that the device pictured in Figs. 27 and 28 represents a single acousto-optic element capable of modulating only some portion of a holographic image (*i.e.*, in an elemental hologram sense). This is due to the fact that the surface acoustic wave has only a limited interaction length with the guided-mode light before the efficiency of the interaction approaches zero. Therefore, placement of several acousto-optic transducers on the same waveguide is necessary in order to obtain a longer holographic line in a scaled-up device. This type of scheme is depicted in Figs. 29 (side view) and 30 (top view). Structurally, a multi-element device is comprised of multiple elements depicted in Fig. 27. Guided-mode light that is undiffracted by a surface acoustic wave continues to propagate in the waveguide and is available for diffraction for subsequent surface acoustic waves. Multiple SAW transducers are positioned along the waveguide axis and interact progressively with guided-wave light in a resonant fashion. Volume holographic Bragg gratings are positioned for reflection of every leaky mode exiting the waveguide.

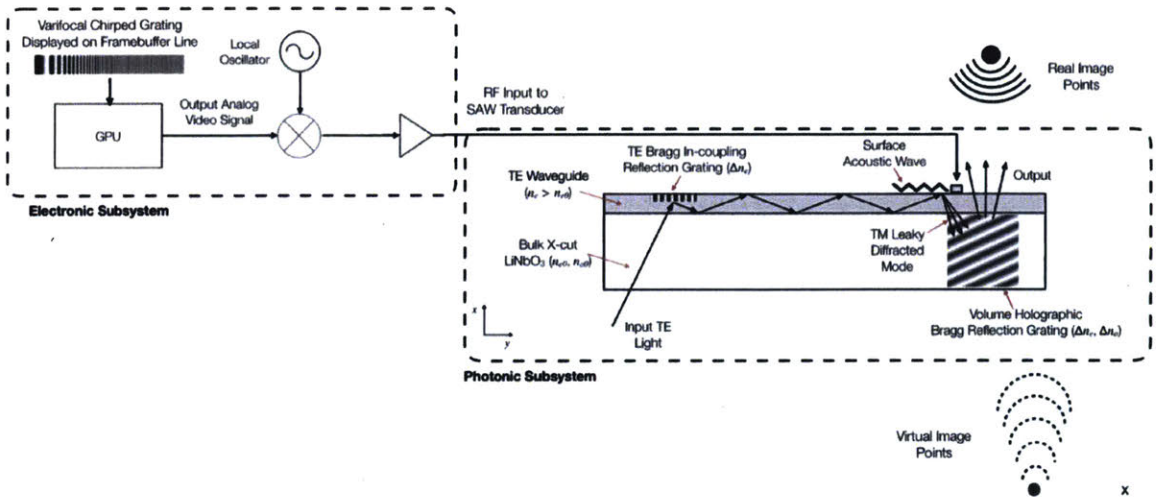

Figure 31: Real and virtual image points generated by depicted architecture.

3.2 SYSTEMS ENGINEERING

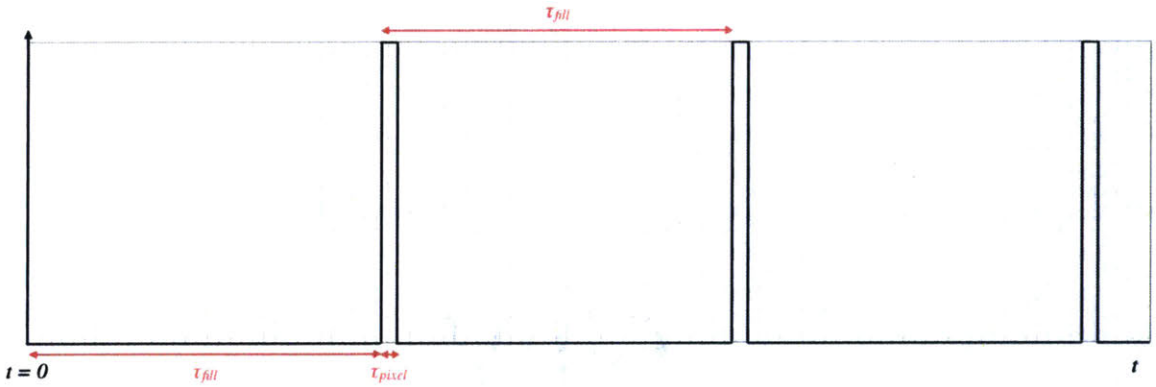

Figure 32: Timing diagram for pulsed laser illumination of SAW devices.

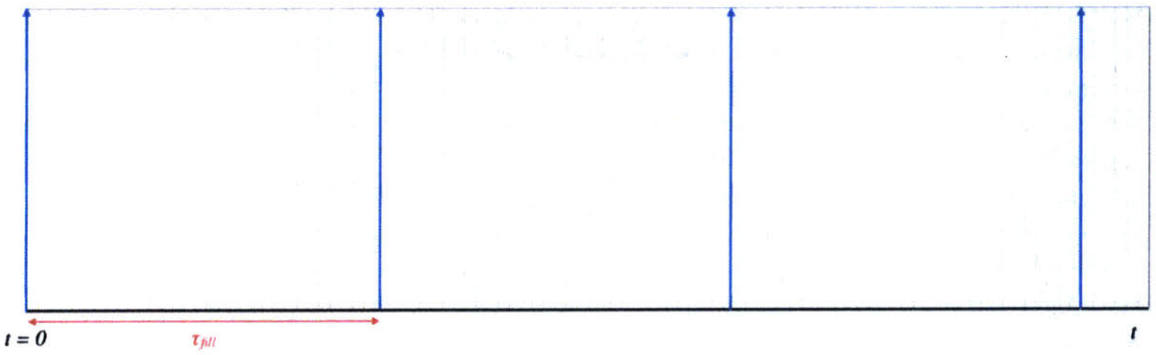

Figure 33: Timing diagram for hsync pulses. τ_{fill} is the time duration over which the aperture is filled by the acoustic pixel stream.

Strobed operation has been presented as a solution to overcoming non-stationarity in acousto-optic modulators when used for beam shaping applications [42]. Note that such a scheme can be used in place of polygonal mirror scanning techniques that have been applied previously for scanned-aperture holographic video displays based around acousto-optic modulators [18–21]. An example timing diagram for strobed operation of the proposed device is depicted in Fig. 32. τ_{fill} is the time duration over which the aperture is filled by the acoustic pixel stream and τ_{pixel} is the time duration over which a single pixel is acoustically drawn. The duty cycle is then $D = \tau_{pixel} / \tau_{fill}$. τ_{fill} can be found as $\tau_{fill} = l/v$, where l is the interaction length and v is the velocity of the propagating surface acoustic wave. For x-cut $LiNbO_3$, $v = 3909$ m/s; assuming an interaction length $l = 1$ cm, $\tau_{fill} = 2.558$ μs. For a 400 Mpixel/s pixel clock from a modern graphics processing unit, $\tau_{pixel} = 1/400$ Hz = 2.5 ns. Note that each illumination pulse would be tied to the length taken for the graphics processing unit to output one filled aperture's worth of pixels; this can readily be set to be one horizontal line on the GPU framebuffer and hence the pulses can be triggered on the GPU's hsync pulses (depicted in Fig. 33).

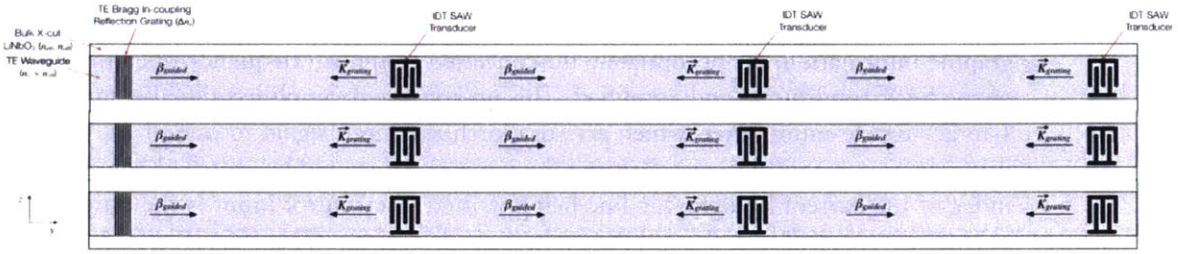

Figure 34: $z - y$ cross-section (top view) of multi-element, multi-channel SAW device.

Each waveguide (being driven with either a single or multiple SAW transducers) is responsible for delivering a single horizontal parallax-only holographic line to the viewer. In order to deliver imagery with greater vertical resolution, multiple such holographic lines are required in the output. Scanned-aperture displays based around bulk-wave acousto-optic modulators [20, 21] or guided-wave acousto-optic devices [18, 19] employ scanning galvanometers to optically scan multiple holographic lines within the persistence time of the human eye. However, a flat-panel holographic video display requires that no supporting optics be used. Therefore, increased vertical resolution can only be achieved via the use of additional waveguide channels [18]. Such a scheme is depicted in Fig. 34. In this scheme, light is coupled into all waveguides simultaneously via in-coupling Bragg gratings that are positioned on top of each waveguide. As in Figs. 29 and 30, multiple SAW transducers and reflection Bragg gratings are positioned along the length of each waveguide.

In order to electrically drive the entire multi-element, multi-channel device depicted in Fig. 34 with holographic information with the limited temporal bandwidth available from modern GPUs, it is proposed that each *column* of SAW elements spanning multiple waveguides be driven by a single analog output channel of a graphics processing unit in a time-sequential fashion. This would allow for the possibility of coherence amongst surface acoustic waves generated by multiple SAW transducer elements on a single waveguide (*i.e.*, all the holographic information spanning multiple SAW transducers on a single holographic line is drawn at the same time) as well as reduce the number of analog GPU channels needed. Such a scheme can be implemented via the use of an analog RF demultiplexer as shown in Fig. 35. Here, the output analog signal from the graphics card (containing holo-

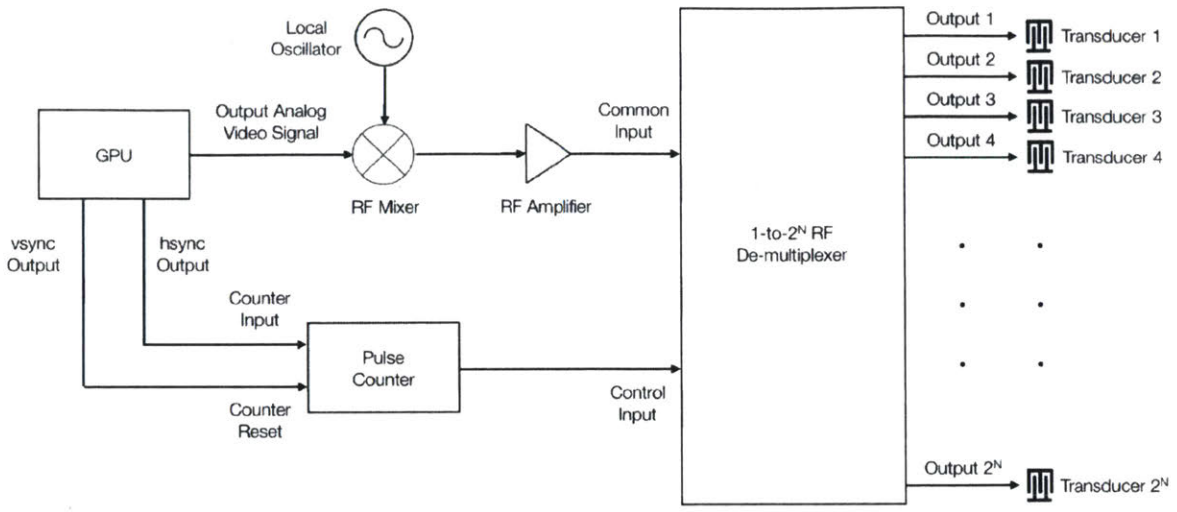

Figure 35: Electrical path for GPU signal output, RF up-conversion and amplification, and switching amongst holographic lines for driving multiple holographic lines in sequence.

graphic information) is appropriately up-converted to the RF frequency operating band of the SAW transducers and amplified. This up-converted, amplified signal is input to a 1-to-2^N RF de-multiplexer, which acts to switch the input signal to one of 2^N outputs depending on a control input. Because the input signal should be switched based on the index of the current holographic line being written, the control input is the output of a counter that accumulates the number of hsync pulses output from the GPU. This control scheme necessitates that the holographic information driving a single transducer is contained on a single framebuffer line in the GPU's memory. During the duration between hsync pulses, the holographic information for the ith holographic line is drawn; after drawing is completed, the GPU fires a hsync pulse, incrementing the pulse counter, and thereby switching the output to a transducer on the next holographic line. After all lines have been switched to and drawn, the counter is reset upon receiving a vsync pulse from the GPU and the de-multiplexer is therefore reset to output to the first holographic line's transducer.

Note that all independent sequential transducers per holographic line would be addressed by independent GPU channels and de-multiplexing hardware. In this way, multiple transducers per holographic line are addressed in a parallel fashion while separate holographic lines are addressed in a serial fashion.

3.3 RADIOMETRY, STAGE-WISE EFFICIENCIES, AND EYE SAFETY

It is expected that a multi-element, multi-channel SAW device of the type pictured in Fig. 34 will be optically illuminated with a coherent laser light source. It is important that the perceived brightness of the displayed imagery is calibrated for comfortable viewing and that the total optical power entering the eye conforms to published safety standards [47]. The power of a source should be chosen such that the output power entering the viewer's eye meets such criteria after all losses in the system are accounted for. Employing the analysis in [48] and [49], as a starting point, 50 μW is assumed as a desirable time-averaged display optical power entering the eye.

To characterize typical losses in the SAW device, a total optical efficiency η_{total} can be calculated. Assuming an input grating coupling efficiency of $\eta_C = 0.5$, a guided-to-leaky mode coupling efficiency of $\eta_{MC} = 0.05$, and a diffraction efficiency of $\eta_R = 0.95$ for the Bragg reflection grating, $\eta_{total} = \eta_C \eta_{MC} \eta_R = 0.0238$ for a single transducer per waveguide. For multiple transducers per waveguide (*i.e.*, a multi-element configuration), η_{MC} applies per transducer. The total efficiency of all N transducers per waveguide (*i.e.*, the ratio of the power of all diffracted light from all transducers on a waveguide channel to the total power input to that waveguide) is a geometric series as:

$$\begin{aligned}\eta_{MC,N} = \\ \eta_{MC} + (1-\eta_{MC})\eta_{MC} + (1-\eta_{MC})(1-\eta_{MC})\eta_{MC} + \ldots + (1-\eta_{MC})^{N-1}\eta_{MC} \\ = \eta_{MC} \sum_{i=0}^{N-1} (1-\eta_{MC})^i = \eta_{MC} \frac{1-(1-\eta_{MC})^N}{\eta_{MC}} = 1-(1-\eta_{MC})^N \end{aligned} \quad (5)$$

$\eta_{total,N}$ for a single channel with, *e.g.*, $N = 5$ transducer elements is then $\eta_{total,N} = \eta_C \eta_{MC,N} \eta_R = \eta_C \eta_R (1-(1-\eta_{MC})^N) = 0.1075$. For M waveguide channels, the total input power is split evenly amongst all waveguide channels, and therefore for a given input power P_{input}, the power entering each channel is $P_{channel} = P_{input}/M$. The total output power from the composite M-channel, N-element device is then $P_{out} = MP_{channel}\eta_{total,N} = P_{input}\eta_{total,N}$. Note that the total efficiency does not depend on the number of waveguide channels but only on the number of transducer elements.

For a desired output power entering the eye of $P_{out} = 50\ \mu$W, $P_{in} = 0.46$ mW for a 5 transducer element device. Lasers at such output power levels and operating in pulsed configurations are readily available.

3.4 TRANSDUCER DESIGN AND TEST PATTERNS

The information presented in this section draws from work initially presented in Bianca Datta, Nickolaos Savidis, Michael Moebius, Sundeep Jolly, Eric Mazur, and V. Michael Bove, Jr., "Direct-laser metal writing of surface acoustic wave transducers for integrated-optic spatial light modulators in lithium niobate," Proc. SPIE Advanced Fabrication Technologies for Micro/-Nano Optics and Photonics X, 10115, 2017 [79].

Interdigital transducers are utilized to excite propagating surface acoustic waves in piezoelectric materials and are commonly employed for guided-wave acousto-optic devices [41]. Fig. 36 depicts a schematic for an interdigital surface acoustic wave transducer excited by an RF electrical source. A series of interdigitated "fingers" are evenly spaced for a desired transducer period Λ and a total number of fingers N. In combination, these parameters influence the acoustic response of the transducer, chiefly dictating its acoustic center frequency and bandwidth as:

$$f_c = v_a/\Lambda \quad (6)$$

where f_c is the acoustic center frequency of the transducer, v_a is the acoustic wave speed of the piezoelectric substrate, and Λ is the transducer period. The effective range of RF excita-

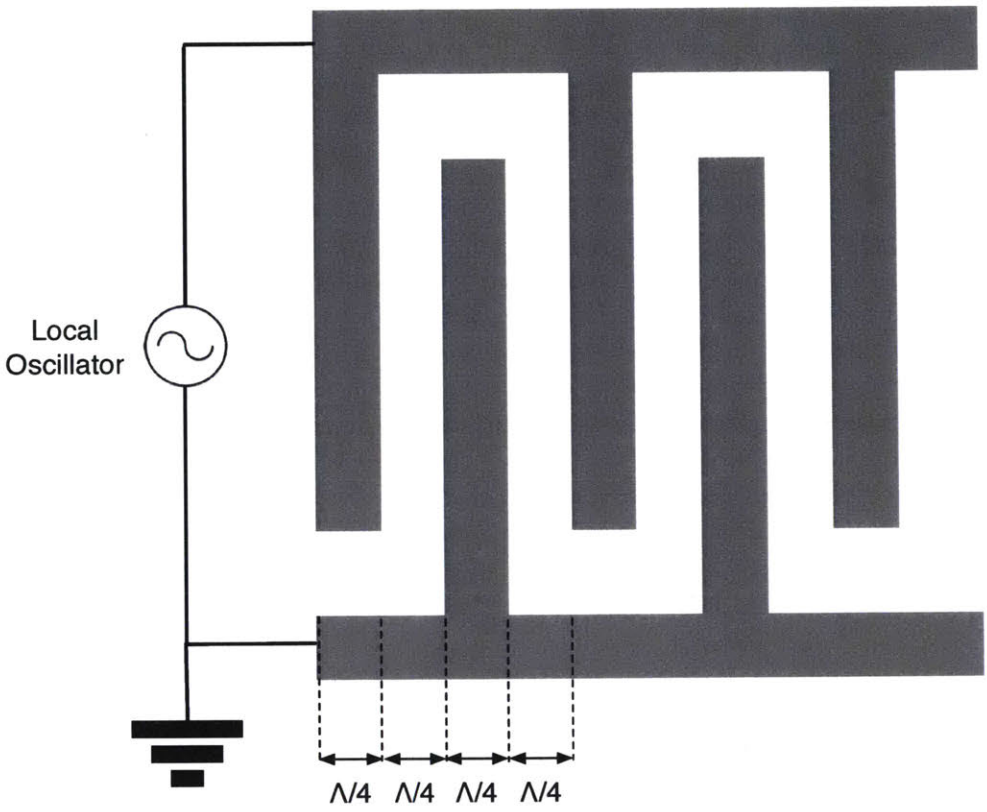

Figure 36: Schematic of an interdigital surface acoustic wave transducer. A uniform, interdigitated SAW transducer is comprised of a series of spaced "fingers," each of which has width $\Lambda/4$ and inter-finger spacing $\Lambda/4$. The overall period of the transducer Λ and the number of finger pairs N dictate the transducer center frequency and acoustic bandwidth. The transducer is excited by an RF electrical source as shown.

tion frequencies over which the transducer produces an acoustic response is approximately given by:

$$\Delta f \approx f_c / N \tag{7}$$

where Δf is the RF and acoustic bandwidth and N is the number of finger pairs in the transducer [41]. As an example, a sample design for a transducer with $\Lambda = 50$ μm and $N = 10$. For x-cut, y-propagating geometries of $LiNbO_3$, the acoustic propagation velocity is $v_a = 3909$ m/s [38, 39]. The designed transducer then has $f_c = 78.1$ MHz and $\Delta f = 7.8$ MHz around the center frequency. It should also be noted that other transducer geometries, such as those with linearly-chirped transducer periods along the active length, can be designed to enable other acoustic passband functions for the RF excitation [41].

4

METHODS IN FEMTOSECOND LASER MICROMACHINING

The information presented in this chapter draws from work initially presented in

1. *Nickolaos Savidis, Sundeep Jolly, Bianca Datta, Michael Moebius, Thrasyvoulos Karydis, Eric Mazur, Neil Gershenfeld, and V. Michael Bove, Jr., "Progress in fabrication of waveguide spatial light modulators via femtosecond laser micromachining," Proc. SPIE Advanced Fabrication Technologies for Micro/Nano Optics and Photonics X, 10115, 2017 [50].*

2. *Sundeep Jolly, Nickolaos Savidis, Bianca Datta, Thrasyvoulos Karydis, Will Langford, Neil Gershenfeld, and V. Michael Bove, Jr., "Progress in fabrication of anisotropic Bragg gratings in lithium niobate via femtosecond laser micromachining," Proc. SPIE Advanced Fabrication Technologies for Micro/Nano Optics and Photonics XI, 10554, 2018 [51].*

In recent years, direct laser writing has emerged as a promising alternative for the generation of embedded passive and active photonic structures within various optically transparent media [54]. The use of femtosecond laser micromachining in $LiNbO_3$ has recently been proposed for fabrication of index-structures including waveguides [55, 63, 70], multiplexing and de-multiplexing architectures [64], diffraction gratings [65–68], and active metal layers [69], and volume holographic elements. For the purposes of rapidly prototyping integrated optic devices for spatial light modulation, femtosecond laser micromachining offers a compelling alternative to traditional lithographic processing because of the ease with which fabrication parameters can be adjusted. The integrated optic device described in Chapter 3 can be fabricated entirely via a femtosecond laser micromachining process, and in particular, volume Bragg gratings with arbitrary fringe geometries are more readily rapidly-prototyped using direct laser writing rather than conventional holographic recording. In this chapter, methods for the integration of refractive index features and for the metal patterning of interdigitated transducers and channel waveguide masks are presented.

4.1 INTEGRATION OF DENSIFIED REFRACTIVE INDEX FEATURES IN $LINBO_3$

Traditional processing schemes for the generation of integrated photonic structures within $LiNbO_3$ substrates have typically included conventional resist-based photolithographic and electron-beam lithographic techniques alongside wet- [57] or dry-etching [58]. Furthermore, ion-diffusion techniques such as titanium indiffusion [59] and proton exchange [60] are commonly used to create high-contrast anisotropic waveguides for the generation of active integrated acousto-optical [61] and electro-optical [62] devices.

Femtosecond laser structuring of transparent media is widely used to create 2-D and 3-D profiles in refractive index within the volume of transparent media [54] (see Fig. 37 for a depiction of this processing), subject to limitations imposed on resolution and achievable modulation by the diffraction-limited waist size of the focusing objective and material

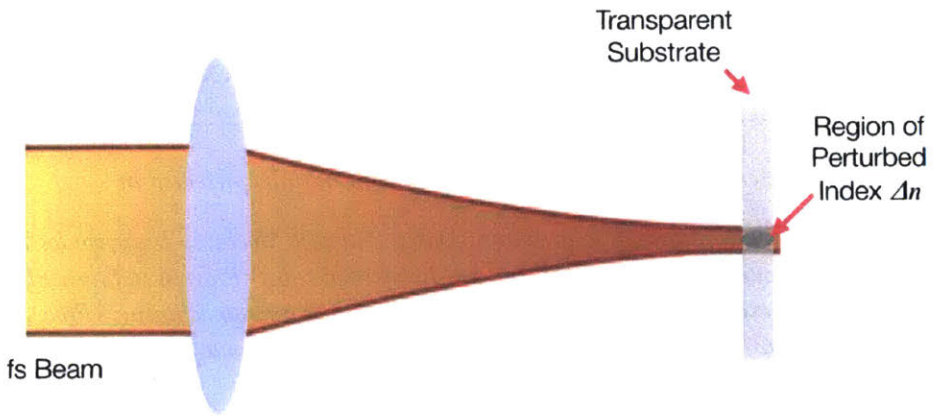

Figure 37: Femtosecond laser-based volumetric index perturbation in transparent media. The femtosecond beam is focused through an objective into the volume of the transparent media, creating a localized effect. Depending on the beam energy density, localized changes in refractive index can occur via densification.

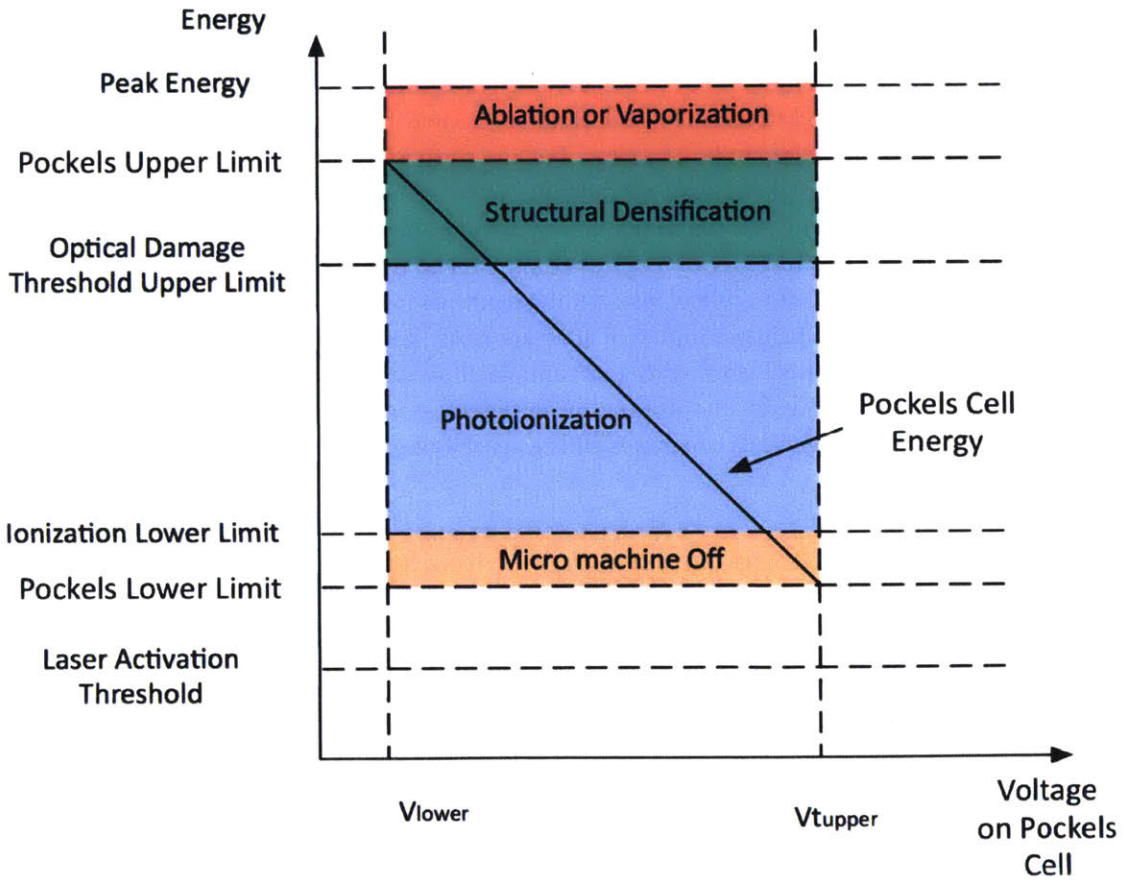

Figure 38: Adapted from [52]. Energy regimes in femtosecond laser micromachining. Depending on the energy density of the focused femtosecond beam at the focal region, densification, photoionization, or ablation can occur in the medium.

thresholds for densification and available dynamic range (see Fig. 38 for a depiction of energy thresholds in focal regions, as a function of beam attenuation depicted via an external Pockels cell intensity modulator). Previous studies of femtosecond laser micromachining in lithium niobate have focused on the integration of embedded photonic structures on the surface or within the volume of the crystalline substrate, usually by means of a permanent change of birefringent refractive index via lattice densification [55], although techniques exploiting volumetric photorefractive modifications have also been utilized [56].

4.1.1 *Direct Laser Writing of Volumetric Features in $LiNbO_3$*

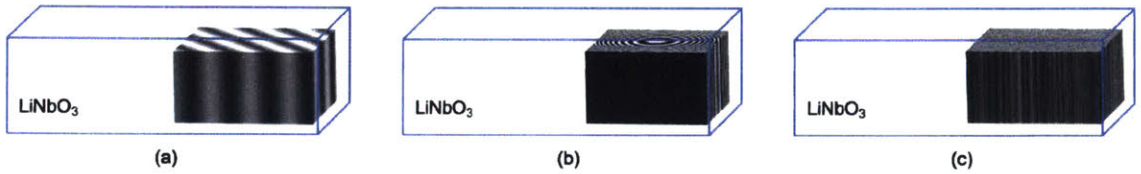

Figure 39: Volumetric grating structures achievable in $LiNbO_3$ via femtosecond laser processing. (a) Volume Bragg gratings having arbitrary fringe geometries, (b) Volume Bragg gratings having optical power (e.g., spherical-beam or cylindrical-beam volume holograms), (c) Aperiodic optical structures having arbitrary modulation of refractive index at each voxel location.

Permanent refractive index modulation via densification in lithium niobate is often classified into two types of modifications: Type I, in which the extraordinary index is decreased but the ordinary index is unchanged via a femtosecond pulse train, and Type II, in which both uniaxial indices are decreased via a pulse train with pulse durations over 1 ps [70]. Previous studies have indicated the feasibility of fabricating Raman-Nath and volume Bragg gratings in $LiNbO_3$ [66–68]. Although volumetric grating structures are achievable via photorefractive recording in $LiNbO_3$, the recording of arbitrary fringe geometries in angle and periodicity is often cumbersome due to the sometimes extreme propagation angles required of either beam in two-beam holographic recording. In contrast to optical holographic recording, femtosecond laser micromachining offers the ability to embed arbitrary fringe geometries without the need to adjust optical paths for two-beam interference, diffractive lenses having optical power, photonic crystal structures, or completely aperiodic volumetric structures in refractive index (see Fig. 39).

4.1.2 *Direct Laser Writing of Channel Waveguides in $LiNbO_3$*

Similar to the process for inducing permanent volumetric changes in refractive index, femtosecond laser micromachining can be used to induce slightly sub-surface features in $LiNbO_3$ and therefore can be used for the creation of waveguides. This process has been explored by Burghoff *et. al.*, who report a possible index variation on the order of $\Delta n_e \sim 10^{-3}$ [55, 70] (see Fig. 41). Note that while the proton exchange process in $LiNbO_3$ increases the extraordinary index (see Fig. 42) while decreasing the ordinary index ($\Delta n_0 \sim 10^{-2}$) ($\Delta n_e \sim 10^{-3}$), femtosecond laser micromachining can induce only

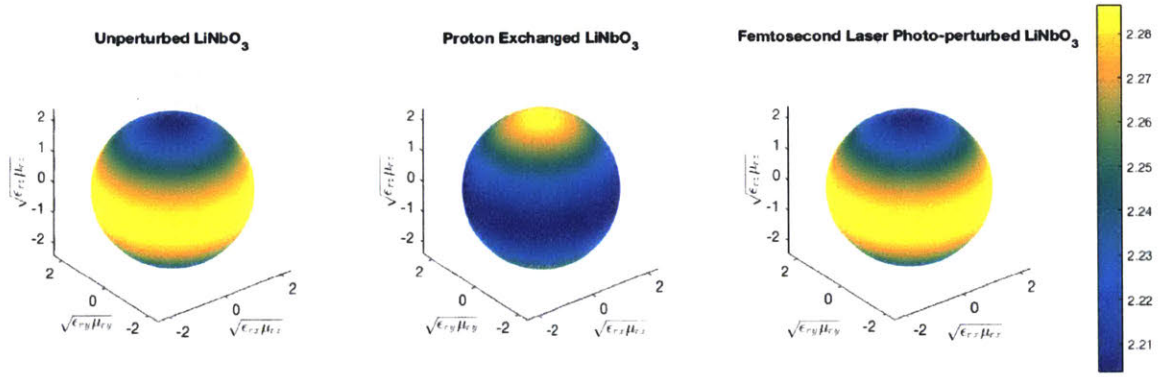

Figure 40: Index ellipsoids for uniaxial lithium niobate. (a) Unperturbed $LiNbO_3$. (b) Proton exchanged $LiNbO_3$. (c) Femtosecond laser photo-perturbed $LiNbO_3$.

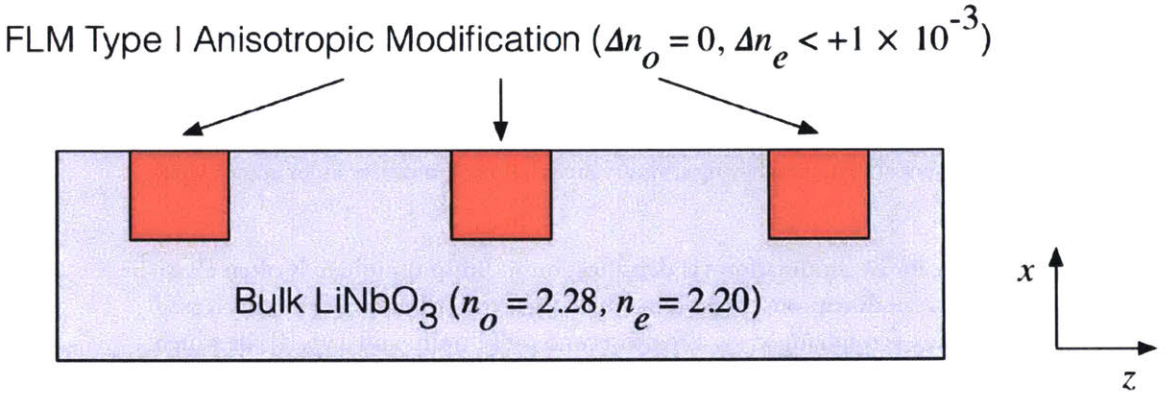

Figure 41: Anisotropic index changes in direct laser-written waveguides in uniaxial lithium niobate.

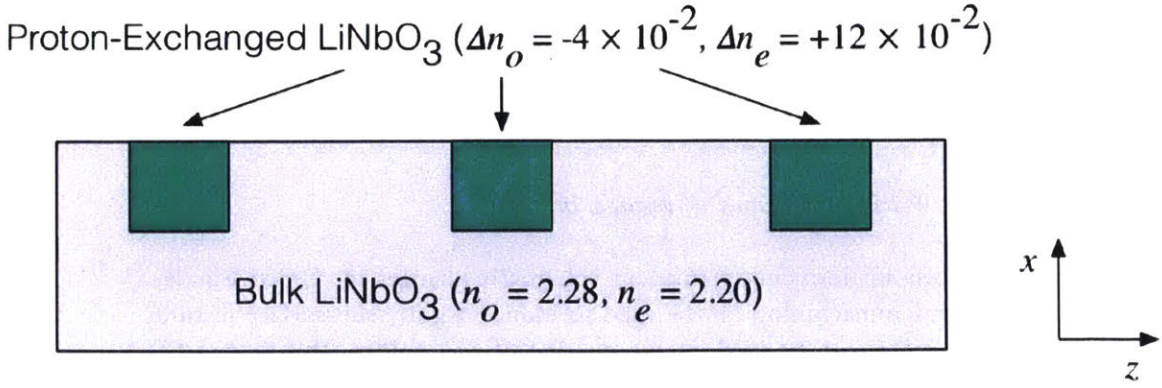

Figure 42: Anisotropic index changes in proton-exchanged waveguides in uniaxial lithium niobate.

a smaller increase in extraordinary index only ($\Delta n_e \sim 10^{-3}$) (see Fig. 40) when creating so-called Type I waveguides [55, 70]. We theoretically examine the role of such reduced index contrast for the performance of the acousto-optic application in direct laser-written waveguides in Ch. 5.

4.2 DIRECT LASER METAL PATTERNING ON LINBO3 SUBSTRATES

With respect to metal patterning, two separate approaches have been explored as part of this work: 1) femtosecond laser-induced forward-transfer, and 2) ablative patterning of thin films. These methods are described here.

4.2.1 *Femtosecond Laser-Induced Forward Transfer for Interdigitated Transducers*

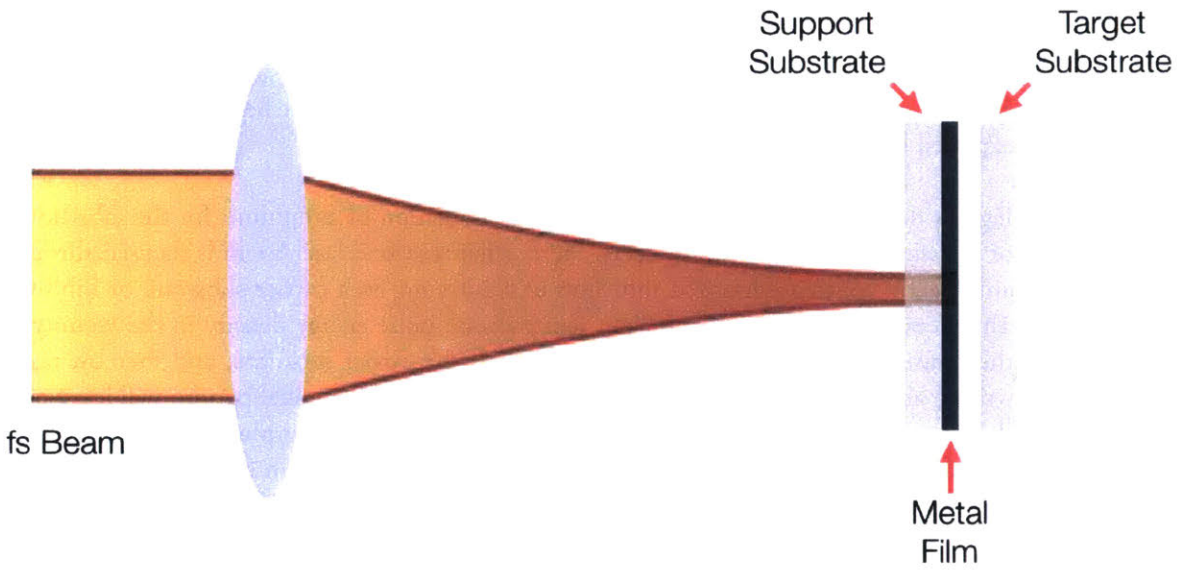

Figure 43: Femtosecond laser-induced forward transfer. A femtosecond beam is focused through an objective into a donor substrate coated with a thin-film of metal. The focused energy thermally ablates the metal, causing it to be transferred onto a target substrate placed in contact with the donor.

Laser-induced forward transfer is a method wherein a transparent donor substrate, coated with a thin film of metal, is placed in contact with the receptor target substrate onto which the metal is to be patterned. The femtosecond beam is focused through the volume of the donor substrate and focused on the metal thin film, causing the metal to thermally ablate and transfer locally onto the target substrate (see Fig. 43 [79]. We have experimented with laser-induced forward-transfer for the fabrication of SAW transducers [79], and some sample results and discussion are presented in Ch. 8 of this thesis.

4.2.2 *Ablative Fabrication of Interdigitated Transducers*

Because of issues related to transducer morphology, roughness, and metal-substrate adhesion, we have additionally examined laser ablation of aluminum as an alternative for the

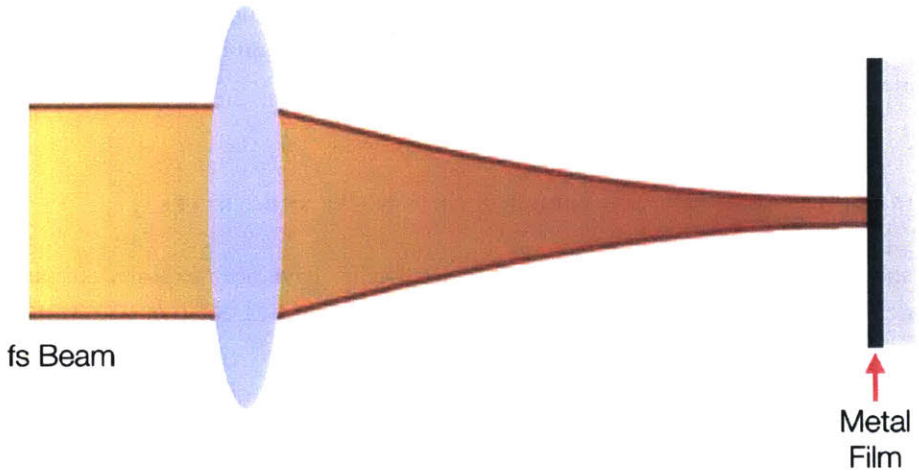

Figure 44: Process for femtosecond laser ablation of aluminum.

fabrication of surface acoustic wave transducers. Such a technique has also been previously explored by Gertus *et. al.* [69].

Fig. 44 depicts a process for femtosecond laser ablation of aluminum for the fabrication of surface acoustic wave transducers. Here, a femtosecond laser beam is focused through an objective onto a deposited thin film of aluminum on a carrier substrate of $LiNbO_3$. The metal in the region of sufficient femtosecond pulse energy density in the vicinity of the nominal beam focus position is ablated off the carrier substrate, and thereby, raster writing an "inverse" pattern relative to the desired remaining metal pattern will leave only the desired pattern while preserving the original thin film's morphology, thickness, and adhesion to the substrate. This thesis presents ablative fabrication of IDTs as a preferred method, and sample results of their fabrication are presented in Ch. 8.

4.2.3 *Ablative Fabrication of Channel Waveguide Masks for Indiffusion*

Using the process depicted in Fig. 44, it is also possible to create channel masks for an indiffusion process for fabricating indiffused-waveguides in $LiNbO_3$. This method has the advantages of retaining the higher index contrast achievable with indiffusion while eliminating the need for conventional lithographic patterning.

4.3 EXPERIMENTAL METHODOLOGY

4.3.1 *Experimental Setup for Laser Micromachining*

The setup presented here for femtosecond laser micromachining is depicted in Figs. 45 and 46. A femtosecond beam from a Yb:KGW femtosecond laser source (Light Conversion Pharos 15W, fundamental operating wavelength $\lambda = 1030$ nm with available harmonics at $\lambda = 515$ nm and $\lambda = 343$ nm) is input to a polarizer and $\lambda/2$ plate for control of beam attenuation. The beam is input to a periscope and reflected off a beamsplitter into the

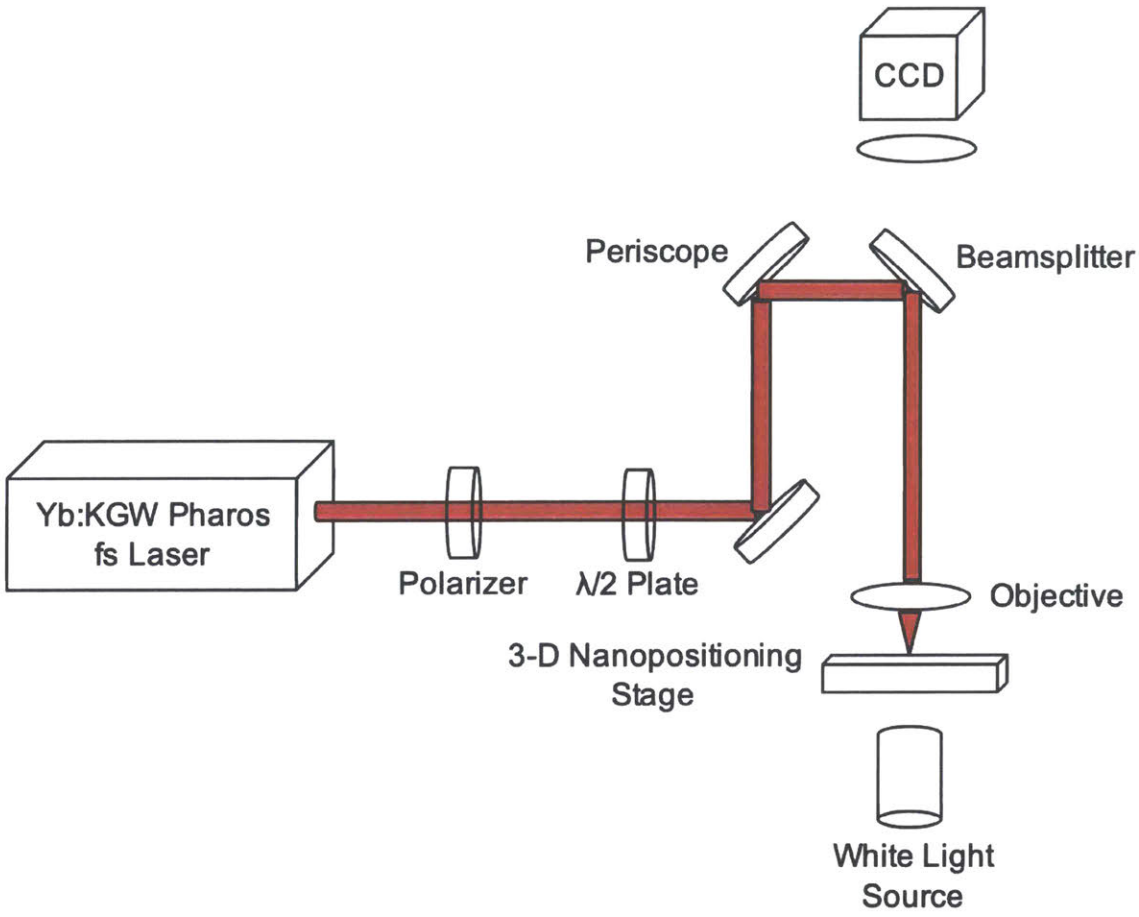

Figure 45: Setup schematic for femtosecond laser micromachining.

Figure 46: Setup for femtosecond laser micromachining.

entrance pupil of a microscope objective (Mitutoyo 10X NA=0.28 infinity-corrected plan apochromatic for features with diffraction limited spot size $d = 1.22\lambda/NA = 2.25\ \mu$m for $\lambda = 515$ nm, or Mitutoyo 100X NA = 0.7 infinity-corrected plan apochromatic for features with diffraction limited spot size $d = 1.22\lambda/NA = 0.89\ \mu$m for $\lambda = 515$ nm) that acts to focus the beam into the volume of the $LiNbO_3$ substrate for volumetric integration, onto the surface for surface densification or ablation, or onto a thin film for metal ablation or laser-induced forward transfer. The sample is mounted on a computer-controlled 3-axis nanopositioning stage (SmarAct, GMBH) with 1 nm resolution and repeatability < 200 nm To control the grating exposure, interfaces to both the laser and stage are controlled via custom software that triggers the beam on while the stage is moving along an area to be densified or ablated and off in other regions during the stage translation.

A white light source is added underneath the transparent sample in order to use the objective along with a CCD camera for imaging simultaneously with writing within the medium with the femtosecond beam. For non-transparent media, the white light illumination is condensed through a condenser lens and launched through the objective for parfocal, epi-illumination.

4.3.2 *Fabrication Parameters and Considerations*

4.3.2.1 *Refractive Index Modulation*

For the purposes of writing gratings and directly-written waveguides, x-cut $LiNbO_3$ wafers with thickness of 1 mm are used. The femtosecond laser source lases with an operating wavelength at the fundamental $\lambda = 1030$ nm, and we observed best results for a repetition rate of 100 kHz, a > 700 nJ pulse energy, and with the stage translating at between 1 mm/s and 5 mm/s while writing any particular grating finger.

Because of focal shift issues associated with writing inside the volume of high-index media, the actual depth at which the stage is translated should be adjusted by a factor $n_{air}/n_s\Delta z$, where n_s is the refractive index of the lithium niobate, n_{air} is the refractive index of air, and Δz is the desired depth inside the volume for writing.

Note that direct laser writing in birefringent media is highly sensitive to the polarization angle of the writing beam relative to the crystal's *c*-axis [70]; for the current experiments, we achieved the highest modulation for beam polarizations parallel to the $LiNbO_3$ *z*-axis. This polarization direction is tunable with the inclusion of a half-wave plate in the writing setup.

4.3.2.2 *Ablative Metal Patterning*

In our trials, we employ a 200 nm thick layer of aluminum, deposited on the $LiNbO_3$ substrate by electron-beam evaporation. A pulse energy in excess of 1.5 μJ using an NA=0.28 microscope objective with a stage translation velocity of 1 mm/s is sufficient to ablate aluminum in this configuration. For best ablative quality, slowing down the stage translation velocity to 0.1 mm/s can provide better results.

5

PHOTONIC MODELING: DEVICE PHYSICS

In this chapter, a comparative analysis of the collinear acousto-optic interaction in both proton-exchanged waveguides and direct laser-written waveguides on $LiNbO_3$ is presented along with an analysis of volume holographic gratings in $LiNbO_3$ for the volume reflection application.

5.1 COLLINEAR GUIDED-TO-LEAKY MODE ACOUSTO-OPTIC INTERACTION

Typical guided-wave acousto-optic devices implemented in $LiNbO_3$ employ anisotropic waveguides that are fabricated using indiffusion processes such as proton exchange, which results in a large increase in extraordinary index relative to the substrate. Because femtosecond laser micromachining is a new modality for fabrication of channel waveguides, it is of interest to theoretically examine the mode-coupling interaction efficiency for a laser-written waveguide relative to that of a proton-exchanged waveguide. Chiefly, the principal difference between a proton-exchanged guide and a laser-written guide is one of index contrast, with proton-exchanged guides exhibiting an extraordinary index increase on the order of 10^{-1} and direct laser-written waveguides exhibiting an increase in the extraordinary index on the order of 10^{-3} - a relative difference of two orders of magnitude. In addition to the influence on waveguide propagation losses, the index contrast differences also dramatically affect the efficiency of the guided-to-leaky mode-coupling interactions.

5.1.1 *Allowable Transition Frequencies*

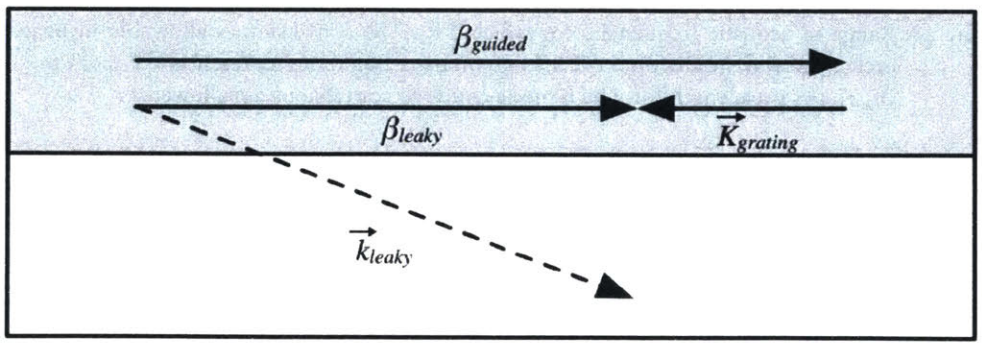

Figure 47: Adapted from [19]. Conservation of momentum in a nearly collinear acousto-optic guided-to-leaky mode transition.

Fig. 47 depicts a conservation relationship between the guided-mode and leaky-mode wavevectors (conservation of momentum), where β_{guided} is the guided-mode effective wavevector in the waveguide, $K_{grating}$ is the counterpropagating acoustic grating wavevector, β_{leaky} is the leaky-mode effective wavevector collinear to the acoustic grating and guided-mode effective wavevector, and k_{leaky} is the leaky-mode total wavevector. Note that k_{leaky} represents an outcoupling from the waveguide at an angle γ relative to the

waveguide axis. From this geometrical picture, the relationship between the guided-mode momentum and the leaky-mode momentum is as follows:

$$\beta_{guided} - K_{grating} = \beta_{leaky} = k_{leaky} n_s \gamma \tag{8}$$

where n_s is the substrate bulk index for lithium niobate for the TM polarization and ordinary ellipsoid axis [40]. From this relationship, it can be observed that the mode-coupling only occurs for $\beta_{leaky} <= k_0 n_{og}$, where n_{og} is the refractive index in the waveguiding region.

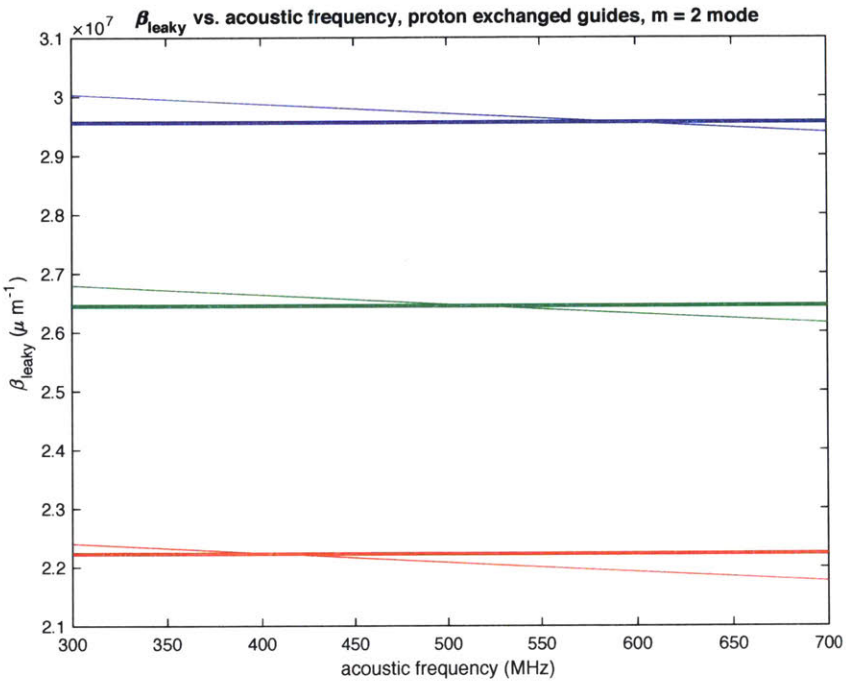

Figure 48: Range of acoustic frequencies for which TE->TM conversion is allowable in proton exchanged waveguides on x-cut lithium niobate. Bold lines represent the upper limit of β_{leaky} per wavelength for which mode-coupling conversions are allowed.

In Figs. 48 and 49, the bold lines represent $k_0 n_{og}$ and the light lines represent β_{leaky}. Based on these results, TE to TM conversions are allowable for more frequencies in DLW guides than in proton exchanged guides.

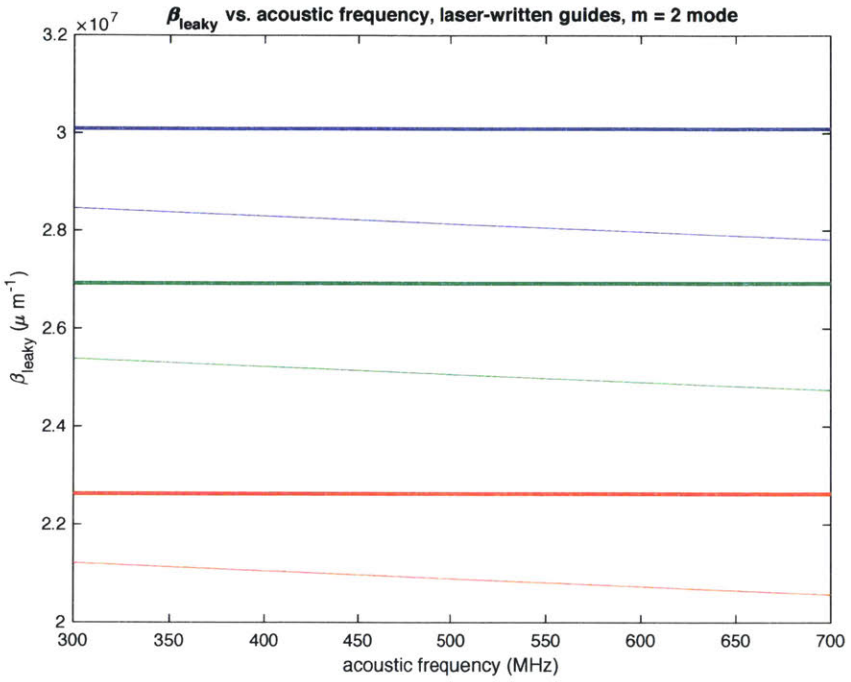

Figure 49: Range of acoustic frequencies for which TE->TM conversion is allowable in laser-written waveguides on x-cut lithium niobate. Bold lines represent the upper limit of β_{leaky} per wavelength for which mode-coupling conversions are allowed.

5.1.2 *Field Overlap Integral*

The propagation of surface acoustic waves is governed by the following mechanical coupled mode equations describing Rayleigh wave propagation [39]:

$$c_{ijkl}\frac{\partial^2 u_k}{\partial x_i \partial x_l} + e_{kij}\frac{\partial^2 \phi}{\partial x_i \partial x_k} = \rho\frac{\partial^2 u_j}{dt^2} \tag{9}$$

and

$$e_{ikl}\frac{\partial^2 u_k}{\partial x_i \partial x_l} - \epsilon_{ik}\frac{\partial^2 \phi}{\partial x_i \partial x_k} = 0 \tag{10}$$

where c_{ijkl} are the elastic stiffness coefficients, u_k is the strain field, e_{ijkl} are the material piezoelectric tensor coefficients, ϵ_{ik} are the dielectric permittivity coefficients, and ϕ is the electric potential. Following Matteo *et. al.*, the SAW-induced permittivity change can be derived and is utilized in the calculation of the overlap integral between the guided-mode and leaky-mode optical fields below.

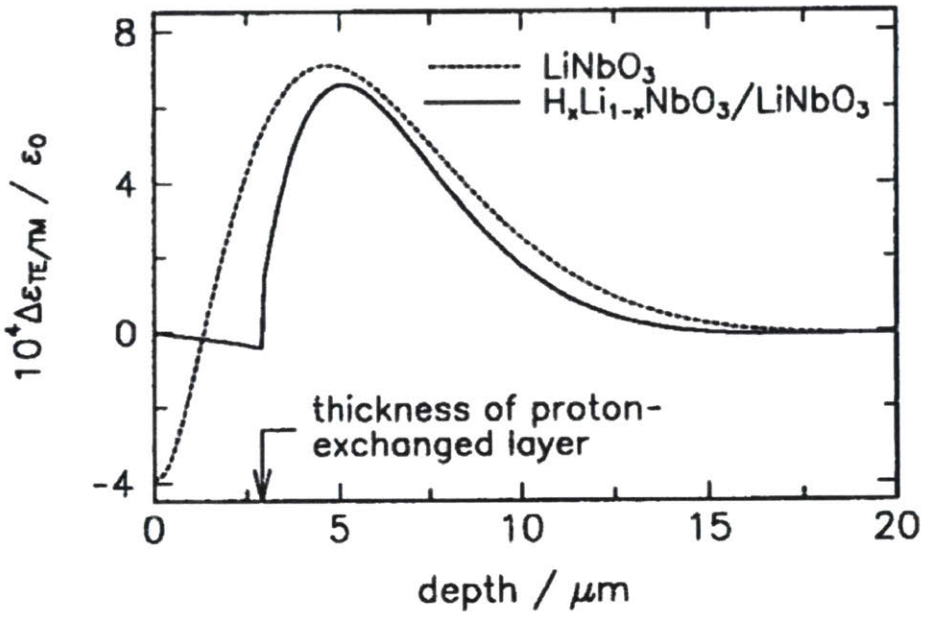

Figure 50: Adapted from [72]. Depth dependence of modulation amplitude for $\Delta\epsilon_{TE/TM}$ for virgin $LiNbO_3$ and proton-exchanged lithium niobate $H_xLi_{1-x}NbO_3$

For the purposes of the current analysis, we adapt the earlier modeling of Rust *et. al.* [72] for numerical values of the modulation amplitude of the permittivity tensor $\Delta\epsilon_{TE/TM}$ in proton-exchanged guides shown in Fig. 50. For the case of laser-written guides, empirical data about the effect of the laser-written index perturbations on the mechanical properties of the $LiNbO_3$ substrate is not readily available, so in this analysis, we assume that the the modulation amplitude of the permittivity tensor closely approximates that of virgin $LiNbO_3$. Then the comparative analysis of the mode-coupling efficiency presented here is based solely on index contrast of the laser-written guides and neglects possible effects of the femtosecond laser-induced perturbations on the mechanical properties of the $LiNbO_3$.

Following Marcuse *et. al.* [96] and Matteo *et. al.* [40], the overlap integral between the guided-mode and leaky-mode optical fields is given by:

$$K_{gl} = \frac{\omega\epsilon_0}{4} \int U_l(x)\Delta[\epsilon(x)]U_g(x)dx \tag{11}$$

where K_{gl} is the coupling coefficient between guided and leaky modes, ω is the acoustic frequency, ϵ_0 is the free-space permittivity, $U_l(x)$ is the leaky mode field, $U_g(x)$ is the guided mode field, and $\Delta\epsilon(x)$ is the depth dependence on permittivity modulation induced by the propagating surface acoustic wave. This overlap integral dictates the amount of energy transferred between the guided-mode field and the leaky-mode field due to the interaction of the surface acoustic wave with the guided-mode optical field.

With respect to modeling the leaky-mode interaction over the device interaction length, the radiative decay coefficient is given by:

$$\alpha_R = |K_{gl}|^2 \cot\gamma dx \tag{12}$$

where γ is the angle of the exiting leaky mode, and its influence on overall device diffraction efficiency is provided as:

$$\eta_D = 1 - e^{-2\alpha_R L} \tag{13}$$

where L is the interaction length between the guided-mode optical field and the surface acoustic wave [40].

Based on Eqs. 11 and 12, the radiative decay coefficients for the mode-coupling interaction as a function of acoustic frequency, for both proton-exchanged waveguides (solid lines) and for laser written waveguides (dotted lines) for three separate wavelengths are computed (see Appendix A for MATLAB code) and plotted in Figs. 51 and 52. This is a key metric for looking at overall device efficiency, and the relative efficiency of the interaction for proton-exchanged waveguides vs. laser-written waveguides is related to the overall device efficiency. Note that the peak value of the radiative decay coefficient across the considered acoustic spectral range is roughly one order of magnitude higher for PE waveguides relative to laser-written waveguides. This implies roughly an order of magnitude lower device efficiency based around the negative exponential relationship for device diffraction efficiency, even at the acoustic frequencies for which the device performance peaks. Furthermore, note for DLW guides, all three wavelengths of interest peak in efficiency over a wider range of acoustic frequencies - this is in contrast to the case for proton exchanged guides, in which it is possible to engineer different acoustic spectral ranges that correspond to distinct peaks for the separate wavelengths being considered. This phenomenon is the basis of frequency-division multiplexing in proton exchanged guides used in earlier guided-wave devices [19],

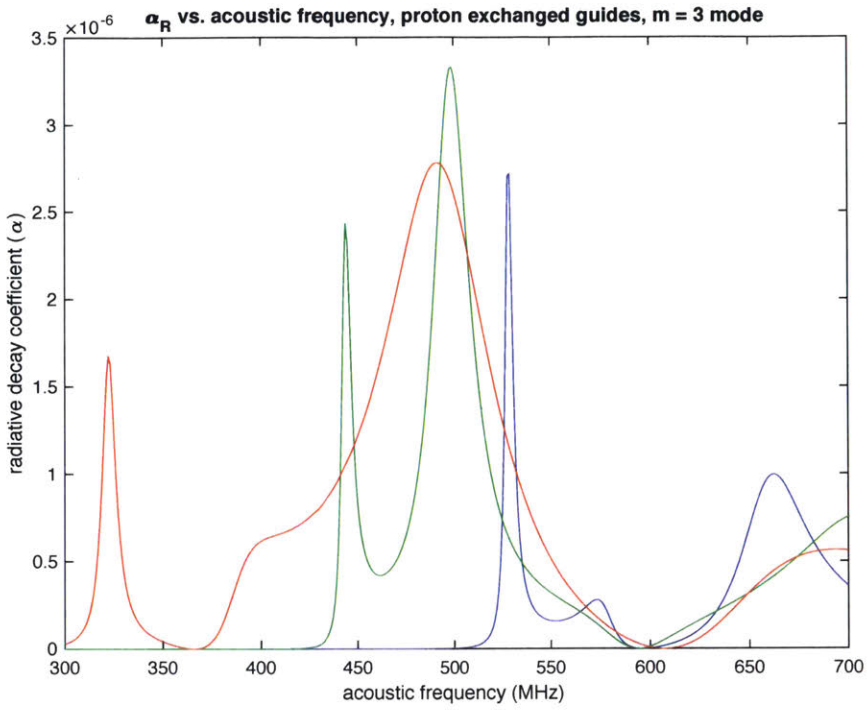

Figure 51: Radiative decay coefficient for proton-exchanged waveguides in x-cut $LiNbO_3$. Thick lines represent the wavenumber boundary below which TE-to-TM mode transitions are allowable.

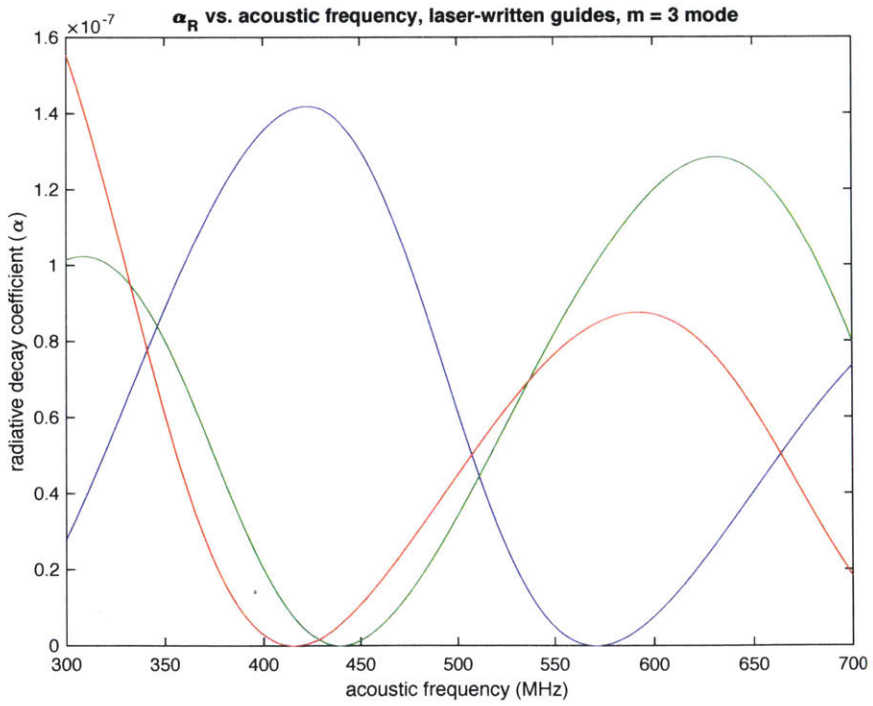

Figure 52: Radiative decay coefficient for laser-written waveguides in x-cut $LiNbO_3$. Thick lines represent the wavenumber boundary below which TE-to-TM mode transitions are allowable.

and therefore this analysis predicts that exploiting the same phenomenon for color displays based around direct laser-written guides is less manageable due to the lower waveguide index contrast achievable.

5.2 PHOTONIC MODELING: LASER-WRITTEN VOLUME PHASE HOLOGRAPHIC GRATINGS

The information presented in this section draws from work initially presented in

1. *Sundeep Jolly, Nickolaos Savidis, Bianca Datta, Daniel Smalley, and V. Michael Bove, Jr., "Near-to-eye electroholography via guided-wave acousto-optics for augmented reality," Proc. SPIE Practical Holography XXXI: Materials and Applications, 10127, 2017 [35].*
2. *Sundeep Jolly, Nickolaos Savidis, Bianca Datta, Thrasyvoulos Karydis, Will Langford, Neil Gershenfeld, and V. Michael Bove, Jr., "Progress in fabrication of anisotropic Bragg gratings in lithium niobate via femtosecond laser micromachining," Proc. SPIE Advanced Fabrication Technologies for Micro/Nano Optics and Photonics XI, 10554, 2018 [51].*

5.2.1 *Kogelnik Analysis in Volume Phase Holography*

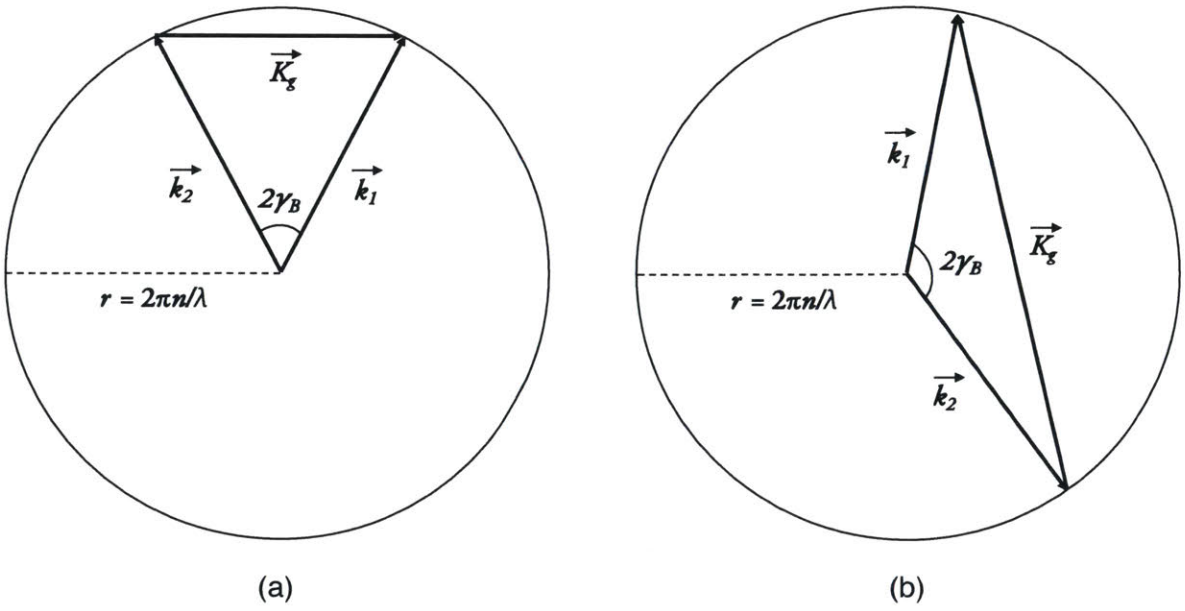

Figure 53: Conservation of momentum in Bragg (a) transmission and (b) reflection gratings.

The fabrication of a volume Bragg grating with desired diffractive behavior is dependent on the grating vector $\vec{K_g}$ that dictates the input and output beams. This relationship is depicted on the Descartes sphere (shown in 2-D for simplicity) for transmission and reflection volume holographic gratings in Fig. 3. Due to conservation of momentum, the relationship $\vec{K_g} = \vec{k_2} - \vec{k_1}$ dictates the diffracted output wavevector $\vec{k_1}$ for a given Bragg-matched input wavevector $\vec{k_2}$ and grating vector $\vec{K_g}$. From a geometrical perspective, the

Bragg angle can be backcalculated from the grating period for a given illumination wavelength as $\gamma_B = \sin^{-1}(\lambda/2\Lambda)$.

According to Kogelnik's coupled-wave theory [44, 73, 75], we present several analyses of the the influence of overall grating thickness on device performance in both transmission and reflection geometries for $LiNbO_3$ with an average unmodulated refractive index $n_{av} = 2.28$ and assuming a maximal achievable femtosecond laser-induced index modulation of $\Delta n = 5 \times 10^{-4}$ (as is consistent with bounds reported in the literature [55, 70]). Figs. 54 and 55 depict the influence of the angular incidence relative to the fully Bragg-matched condition on diffraction efficiency for transmission and reflection volume gratings, respectively. For femtosecond laser micromachined gratings in $LiNbO_3$, the effect of the number of grating layers (having axial thickness of 5 μm) on the diffraction efficiency of the reflection grating is depicted in Fig. 56. Note that the axial thickness used for this simulated result is consistent with those expected with typical objectives used in the experimental setup.

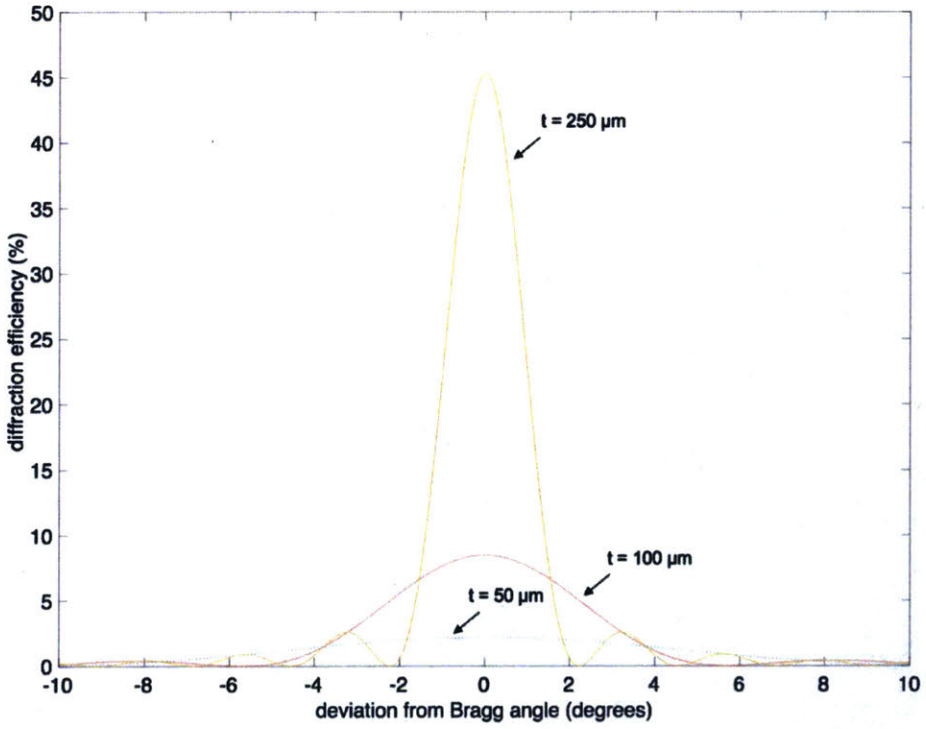

Figure 54: Diffraction efficiency for an unslanted volume transmission grating with $\Lambda = 10$ μm as a function of Bragg mismatch angle for $\lambda = 532$ nm illumination and $t = 50$ μm, $t = 100$ μm, and $t = 250$ μm.

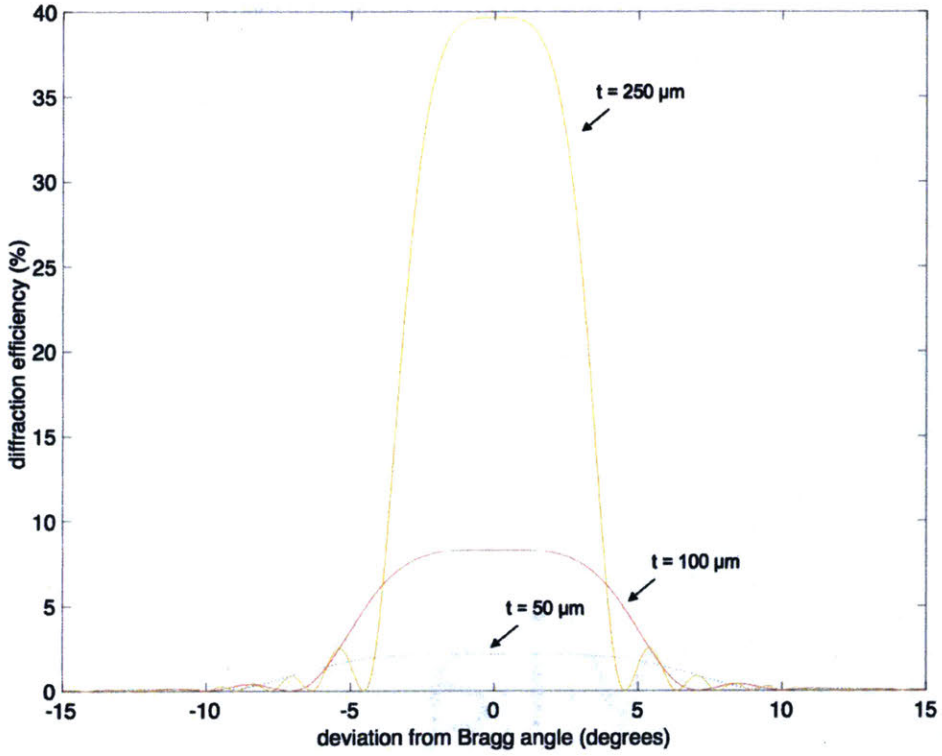

Figure 55: Diffraction efficiency for an unslanted volume reflection grating with $\Lambda = 10\ \mu$m as a function of Bragg mismatch angle for $\lambda = 532$ nm illumination and $t = 50\ \mu$m, $t = 100\ \mu$m, and $t = 250\ \mu$m.

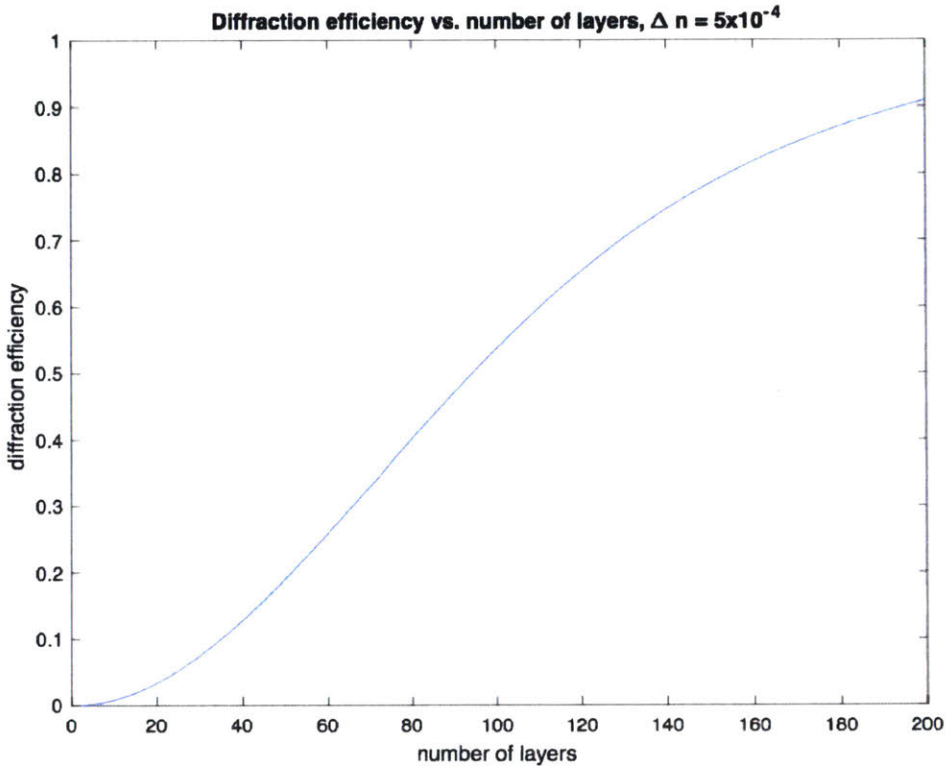

Figure 56: Influence of number of micromachined grating layers on diffraction efficiency for an unslanted volume reflection grating with $\Lambda = 10$ μm and for $\lambda = 532$ nm illumination, assuming a 5 μm axial resolution in the writing spot.

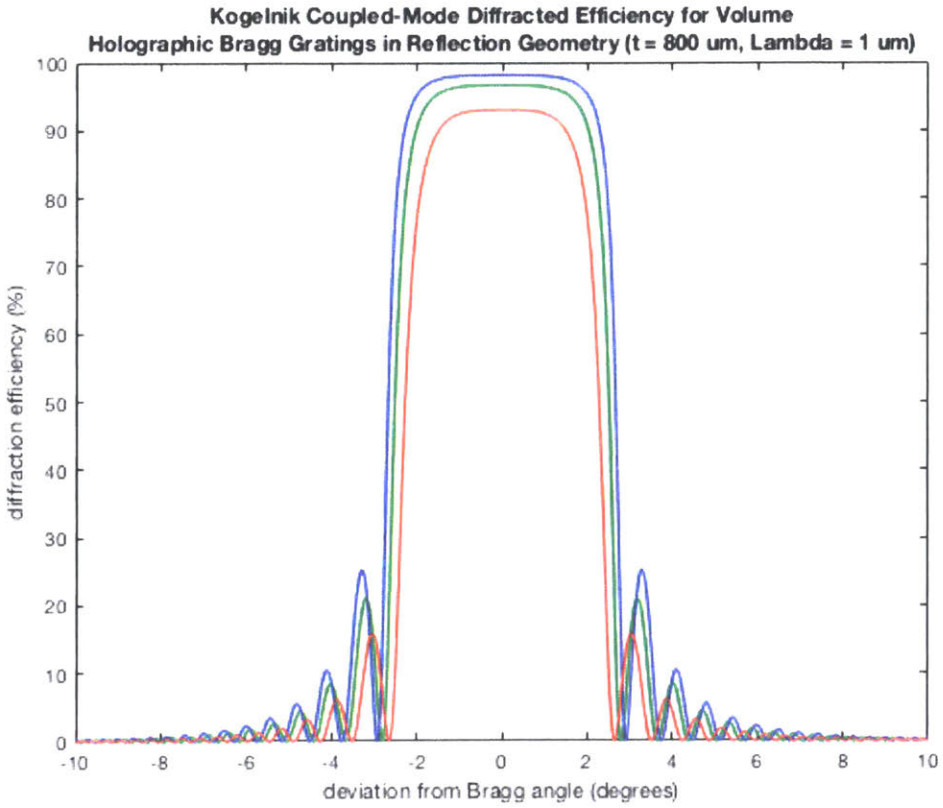

Figure 57: Diffraction efficiency for red, green, and blue wavelengths vs. angular deviation from the Bragg angle for a reflection-mode volume holographic Bragg grating with $\Lambda = 1$ μm and thickness of 800 μm as indicated by Kogelnik's coupled-mode theory.

Fig. 57 depicts the calculated diffraction efficiency for red, green, and blue wavelengths vs. angular deviation from the Bragg angle for a reflection-mode volume holographic Bragg grating with $\Lambda = 1$ μm and thickness of 800 μm as indicated by Kogelnik's coupled-mode theory [44, 73]. Note the wide angular acceptance range, which allows for the total angular extent of a leaky mode to be reflected with high efficiency. Furthermore, wavelength mutliplexing of several Bragg holograms can enable full-color operation [74].

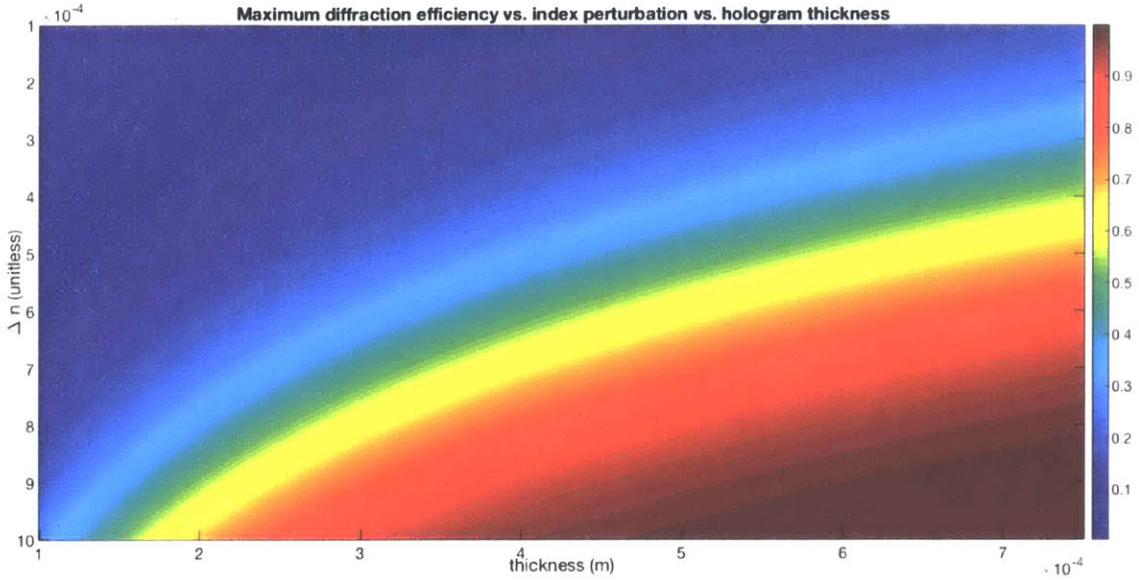

Figure 58: Maximum diffraction efficiency observed in the Bragg selectivity curve as a function of index contrast and grating thickness for a $\Lambda = 1$ μm grating.

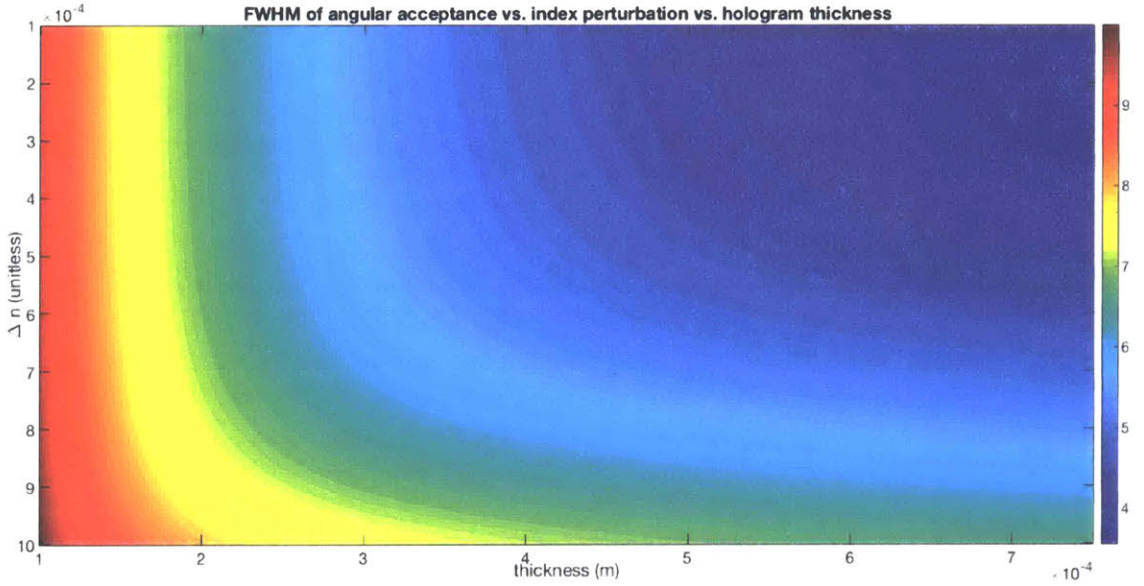

Figure 59: Angular acceptance range observed in the Bragg selectivity curve as a function of index contrast and grating thickness for a $\Lambda = 1$ μm grating.

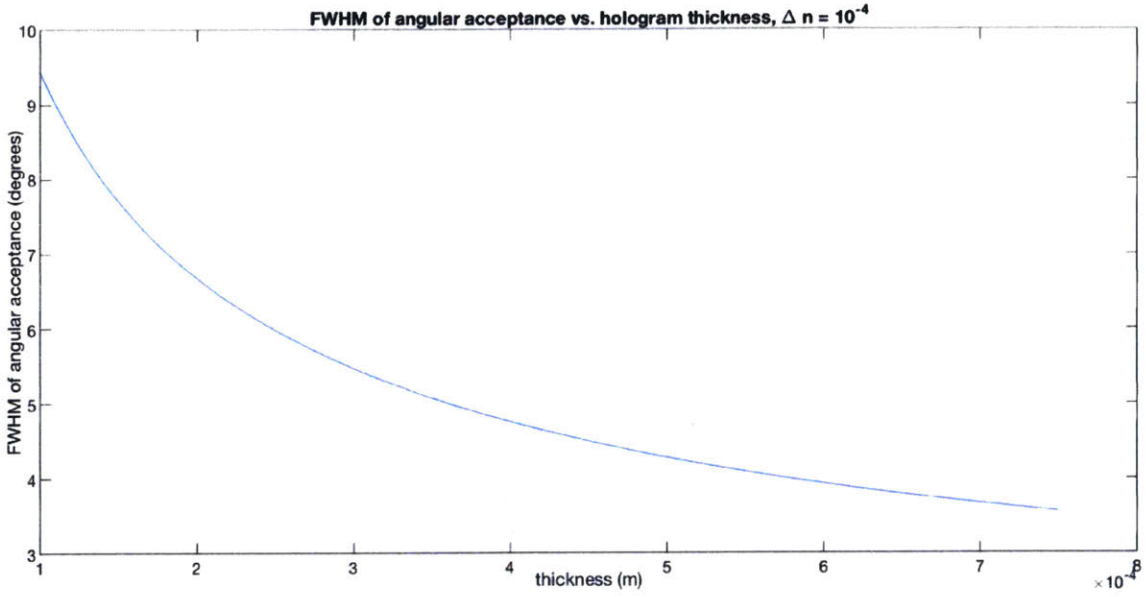

Figure 60: Angular acceptance range observed in the Bragg selectivity curve as a function of grating thickness for a $\Lambda = 1$ μm grating with $\Delta n = 10^{-4}$.

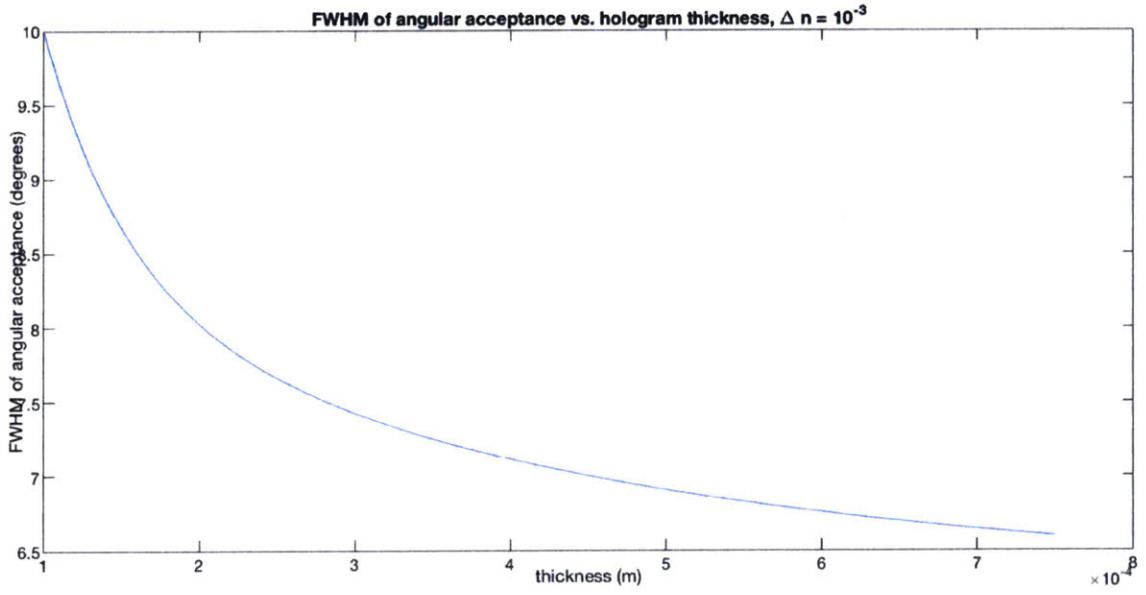

Figure 61: Angular acceptance range observed in the Bragg selectivity curve as a function of grating thickness for a $\Lambda = 1$ μm grating with $\Delta n = 10^{-3}$.

Fig. 57 depicts the diffracted efficiency as a function of the incidence angle's deviation from the Bragg (i.e., nominal reference beam) angle of a slanted volume holographic Bragg grating having maximum index contrast relative to bulk index of $\Delta n = 10^{-3}$, $\Lambda = 1$ μm, and thickness of 800 μm in undoped lithium niobate, considering diffraction of polarized light of wavelengths $\lambda = 473$ nm, $\lambda = 532$ nm, and $\lambda = 633$ nm experiencing an ordinary index of $n = n_0 + \Delta n(x, y, z)$, where $n_0 = 2.28$. Note that diffraction efficiencies above 90% are observed for so-called *Bragg incidence* (i.e., the incident angle of the replay light equals the Bragg angle of the volume holographic grating) and for a wide range of angles around Bragg incidence. This is the *angular acceptance range* of the volume

holographic grating; for incidence angles falling within the angular acceptance range, light will be reflected with very high diffracted efficiencies. These efficiencies fall off sharply at the edges of the angular acceptance range. The plot depicted in Fig. 57 is often termed the *angular Bragg selectivity* of the volume grating.

It should be noted that the shape of the angular Bragg selectivity curve depicted in Fig. 57 varies widely as a function of both the thickness of the grating as well as the maximal index contrast. Fig. 58 and Fig. 59 provide some intuition as to how these parameters influence the maximum achievable diffraction efficiency and the achievable angular acceptance ranges. In Fig. 58, the maximum diffraction efficiency of the Bragg selectivity curve is plotted as a joint function of the index contrast and grating thickness. Note that the highest diffraction efficiencies are observed for thicker gratings (e.g., $t > 500\ \mu$m) and high index modulation values (e.g., $\Delta n > 7 \times 10^{-3}$). In Fig. 59, the full-width at half-maximum of the Bragg selectivity curve (i.e., the angular acceptance range) is plotted as a joint function of the index contrast and grating thickness. Note that the highest ranges are observed for high index contrast values but for low thickness (i.e., the volume gratings are increasingly angularly selective with increasing thickness). Fig. 60 and Fig. 61 depict cross-sections in index contrast of Fig. 59 (plotting angular acceptance range vs. grating thickness) and this increasing selectivity is readily observed. Viewed in combination, Fig. 58 and Fig. 59 indicate that a grating with high angular acceptance and high diffraction efficiency necessitates both a high index modulation and a moderate grating thickness.

5.2.2 *Multiplexing for Angular Acceptance Range Increase*

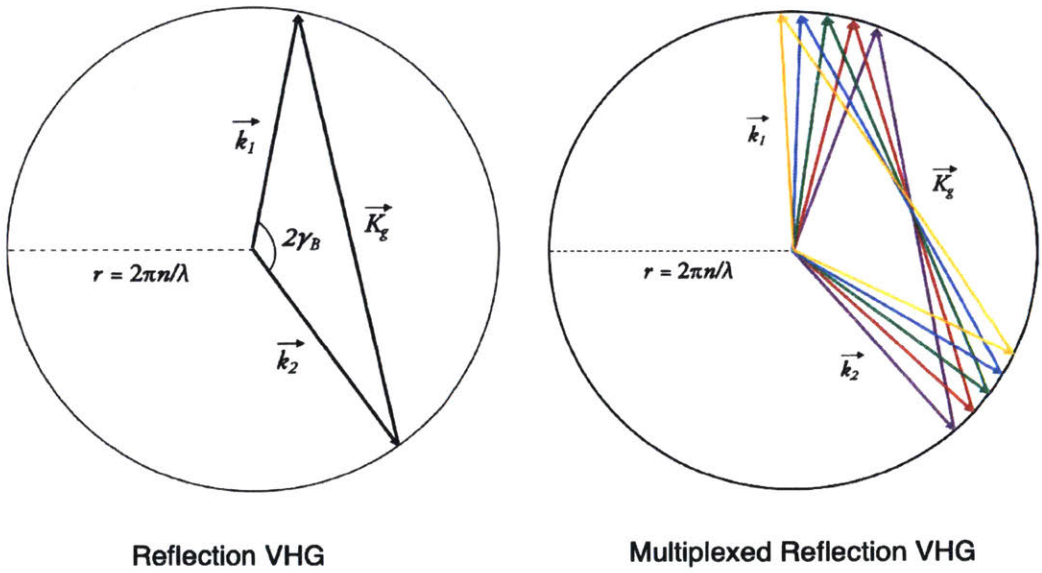

Figure 62: Ewald sphere for multiplexed gratings.

It should also be noted that volume holographic multiplexing [74,76] can also increase angular acceptance range while maintaining a uniform diffraction efficiency. This is depicted in momentum space in Fig. 62, where the different colored grating vectors correspond to Bragg matching conditions at different incident angles. These grating vectors are superim-

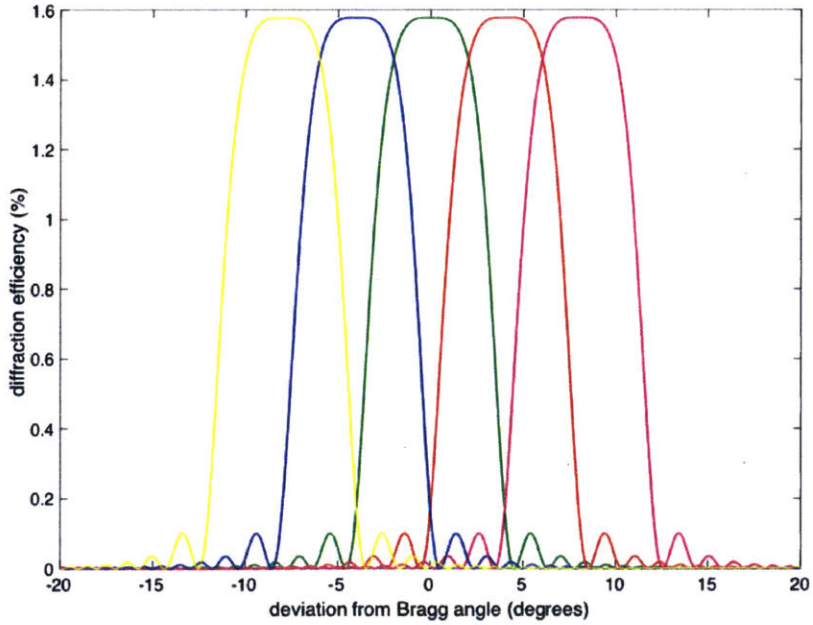

Figure 63: Simulated diffraction efficiency for multiplexed gratings.

posed into the same volume of material. Sample computed diffraction efficiency plots for superimposed gratings are depicted in Fig. 63. Note that the overall angular acceptance range exhibits uniform diffraction efficiency over a much wider range relative to the single grating case. It should be noted that such a multiplexed structure can be computed and written in the volume of the integrated device via femtosecond laser micromachining [100, 102, 103].

6

PHOTONIC MODELING: SYSTEMS ENGINEERING CONSIDERATIONS

The information presented in this chapter draws from work initially presented in Sundeep Jolly, Nickolaos Savidis, Bianca Datta, Daniel Smalley, and V. Michael Bove, Jr., "Progress in transparent, flat-panel holographic displays enabled by guided-wave acousto-optics," Proc. SPIE Practical Holography XXXII: Displays, Materials, and Applications, 10558, 2018 [77].

In this chapter, an analysis of the beam-strobing drive scheme to provide intuition as to achievable resolution, expressible depth, and overall expected image quality is presented. Furthermore, an analysis of expected addressable angular volumes is presented.

6.1 STROBED ILLUMINATION AND NYQUIST-LIMITED KERNEL BLUR

Due to the non-stationarity of traveling acoustic modulation signals, holographic display architectures based around acoustic-optic modulators have historically employed temporally-modulated de-scanning elements, such as polygonal mirrors, to produce stationary image outputs for the viewer. In order to eliminate the need for discrete de-scanning elements, our display architecture employs strobed illumination to enforce some degree of image stationarity in the display output. Such operation has been presented as a solution to overcoming non-stationarity when acousto-optic modulators have been used in beam shaping applications [42]. An example timing diagram for strobed operation of the proposed device is depicted in Fig. 32. τ_{fill} is the time duration over which the aperture is filled by the acoustic pixel stream and τ_{pixel} is the time duration over which a single pixel is acoustically drawn. The duty cycle is then $D = \tau_{pixel}/\tau_{fill}$. τ_{fill} can be found as $\tau_{fill} = l/v$, where l is the interaction length and v is the velocity of the propagating surface acoustic wave. For x-cut $LiNbO_3$, $v = 3909$ m/s; assuming an interaction length $l = 1$ cm, $\tau_{fill} = 2.558$ μs. For a 400 Mpixel/s pixel clock from a modern graphics processing unit, $\tau_{pixel} = 1/400$ Hz = 2.5 ns. Note that each illumination pulse is tied to the time taken for the graphics processing unit to output one filled aperture's worth of pixels.

Given a pixel time $\tau_{pixel} = 2.5$ ns, the effective spatial pitch of an acousto-optically induced pixel is $p = v \times \tau_{pixel} = 3909$ m/s $\times$ 2.5 ns $= 9.77$ μm. Note that this value influences the number of effective acoustic pixels that fit within the interaction length of a single transducer and therefore imposes a bound on the best possible resolution (system MTF) achievable as well as imposing a bound on achievable angular sweep on a per-hogel basis; it should be noted that the pixel clock of the driving signal (i.e., the *RF Nyquist rate*) dictates the cutoff spatial frequency. The pulse duration and timing has also influence over the effective display resolution (i.e., perceptible image blur). As pulses are triggered when the acoustic aperture has been fully filled, the effective perceived intensity results from the eye's integration of all diffracted Fresnel field intensities over the time window of the illumination pulse (as depicted in Fig. 64) [43]. More precisely, the perceived intensity pattern as integrated by the eye resulting from illumination of a traveling acoustic signal

with an illumination pulse of finite duration can be expressed via the superposition of Fresnel-diffracted intensities as

$$I(x) = \int_{-\tau/2}^{\tau/2} \left| \frac{e^{jkz}}{j\lambda z} e^{\frac{jk}{2z}x^2} \int_{X'} f(v*t) e^{\frac{jk}{2z}x'^2} e^{\frac{-j2\pi}{\lambda z}xx'} dx' \right|^2 dt \tag{14}$$

where $I(x)$ is the perceived one-dimensional intensity, t is time with $t = 0$ dictating the time that the aperture has been fully filled, τ is the pulse duration, v is the acoustic propagation velocity, $f(x)$ is the spatial (temporally-variant) acousto-optic modulation signal, z is the observation distance, X' is the space of all positions, and λ is the illumination wavelength.

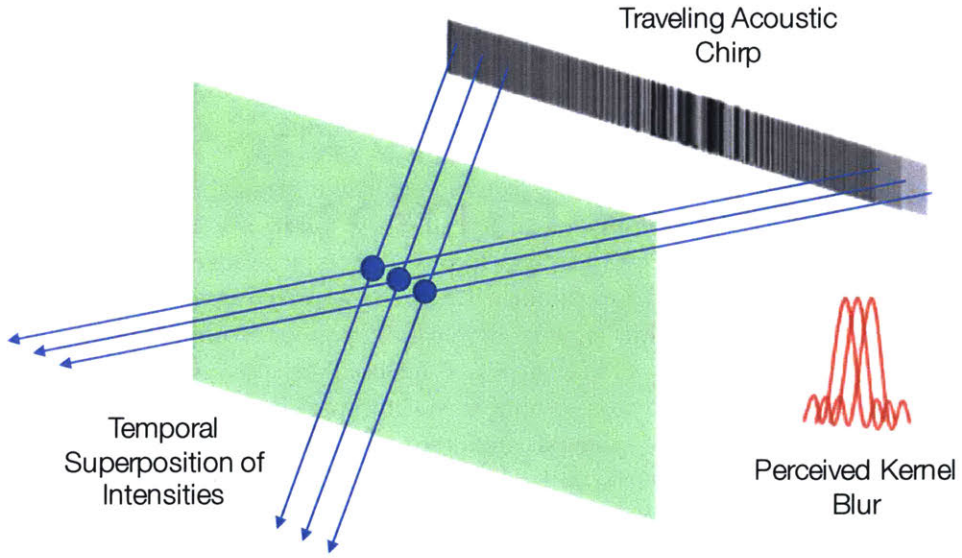

Figure 64: Kernel blur when illuminating a traveling acousto-optic chirped grating with a pulse of finite duration.

In addition to bounds on system resolution due to the RF Nyquist rate of the driving signal, the limited interaction length available for the coherent aperture, and the non-infinitesimal pulse duration of the illumination, our display architecture is also limited in achievable resolutions as a function of the depth at which a scene point is reconstructed by the display. Effective PSF "broadening" occurs as the depths at which points are reconstructed increases relative to the hologram plane; this phenomenon is depicted in Fig. 66, in which the PSF is "baseline-limited" due to the RF Nyquist rate of the driving source for points close to the hologram plane, then broadens as the chirped lenslets required for progressively deeper points begin to "overfill" the available spatial aperture and are low-pass filtered.

To provide intuition for display performance, diffraction from an acousto-optically driven chirp signal is numerically considered here. Fig. 65 depicts the effect of an increased RF Nyquist rate on achievable display resolutions. Fig. 66 depicts increasing broadening of the diffractively-generated point-spread function with increasing point depth due to the limited 5mm interaction length of the device. Fig. 67 depicts the increasing broadening

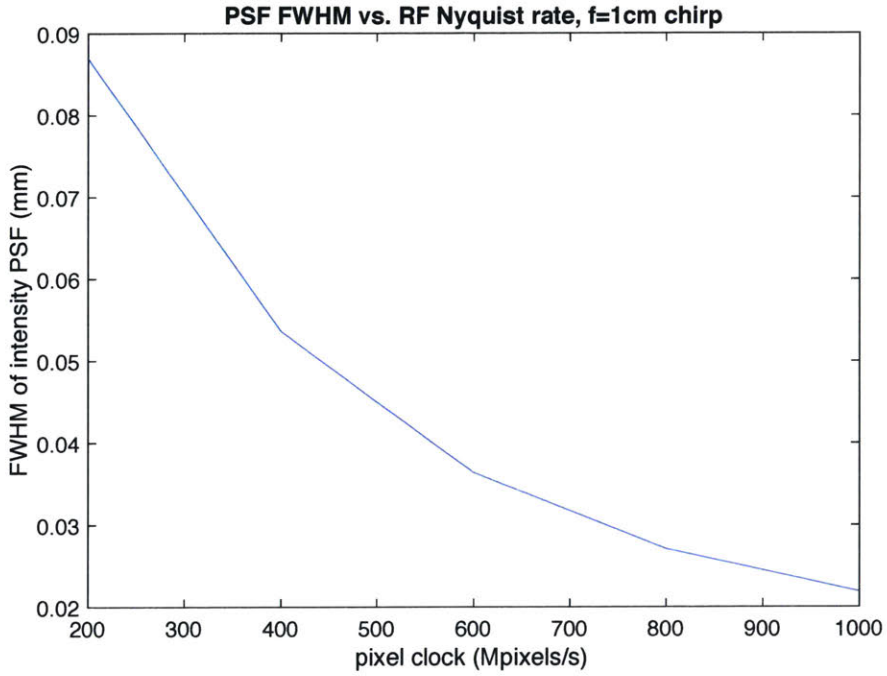

Figure 65: Full-width at half-maximum of the intensity point-spread function of a diffractive chirp lenslet as a function of maximal pixel clock.

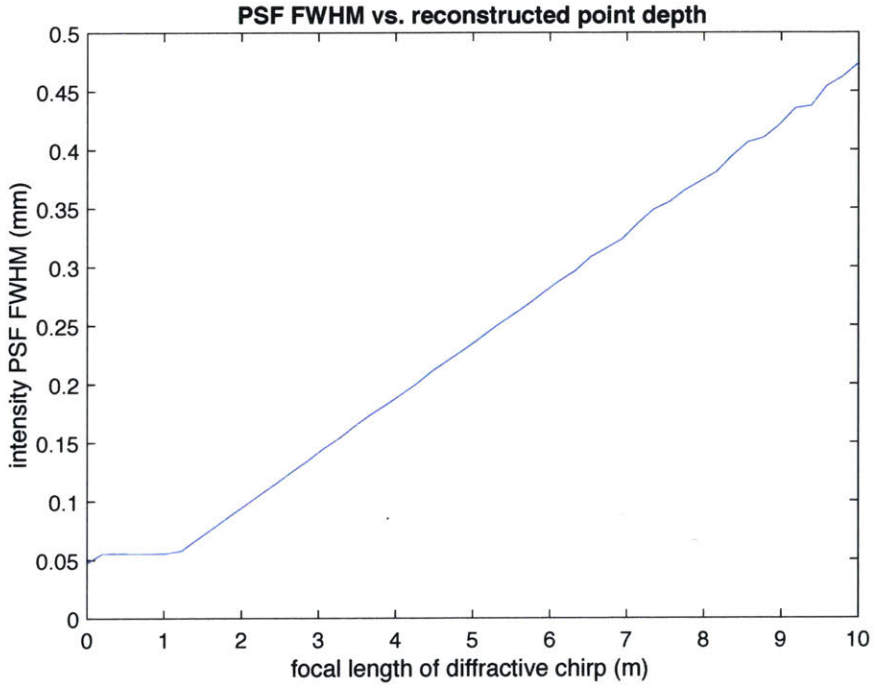

Figure 66: Full-width at half-maximum of the intensity point-spread function of a diffractive chirp lenslet as a function of chirp focal length.

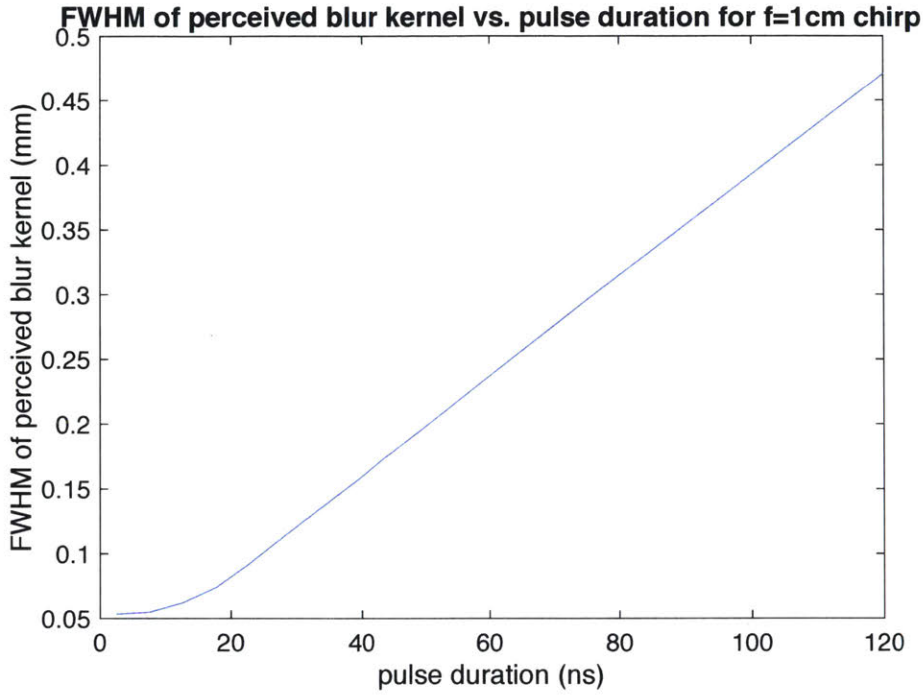

Figure 67: Full-width at half-maximum of the perceived intensity spread function of an acousto-optically driven diffractive chirp lenslet with focal length 1cm as a function of pulse illumination duration, for a drive signal with pixel clock 400 Mpixel/s (pixel time 2.5 ns). Note that this function represents the temporal integral taken by the viewer's eye in Eq. 14.

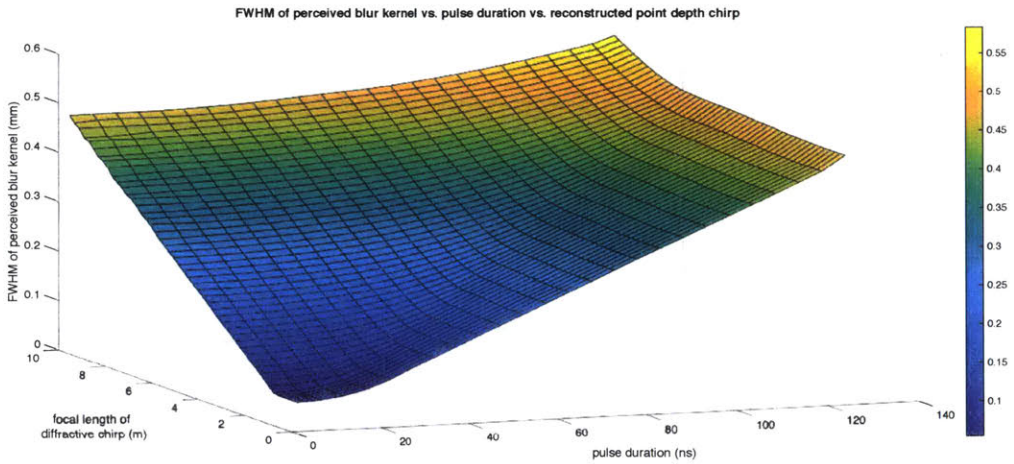

Figure 68: Full-width at half-maximum of the perceived intensity spread function of an acousto-optically driven diffractive chirp lenslet as a joint function of chirp focal length and pulse illumination duration, for a drive signal with pixel clock 400 Mpixel/s (pixel time 2.5 ns). Note that this function represents the temporal integral taken by the viewer's eye in Eq. 14.

of the effective intensity spread perceived by the eye over its integration time as a function of illumination pulse duration for an acoustically-traveling diffractive chirp lenslet in $LiNbO_3$. Fig. 68 depicts the effective intensity spread perceived by the eye over its integration time as a joint function of illumination pulse duration and point depth. It should be noted that the best achievable resolutions are jointly provided for short illumination pulses, scene points close to the hologram plane, and high RF pixel clock rates. The choice of display parameters is likely to be scene- and application-dependent, and should be informed by constraints on required resolution for particular depth ranges, light throughput, and tolerable fidelity.

6.2 DISPLAY ASTIGMATISM

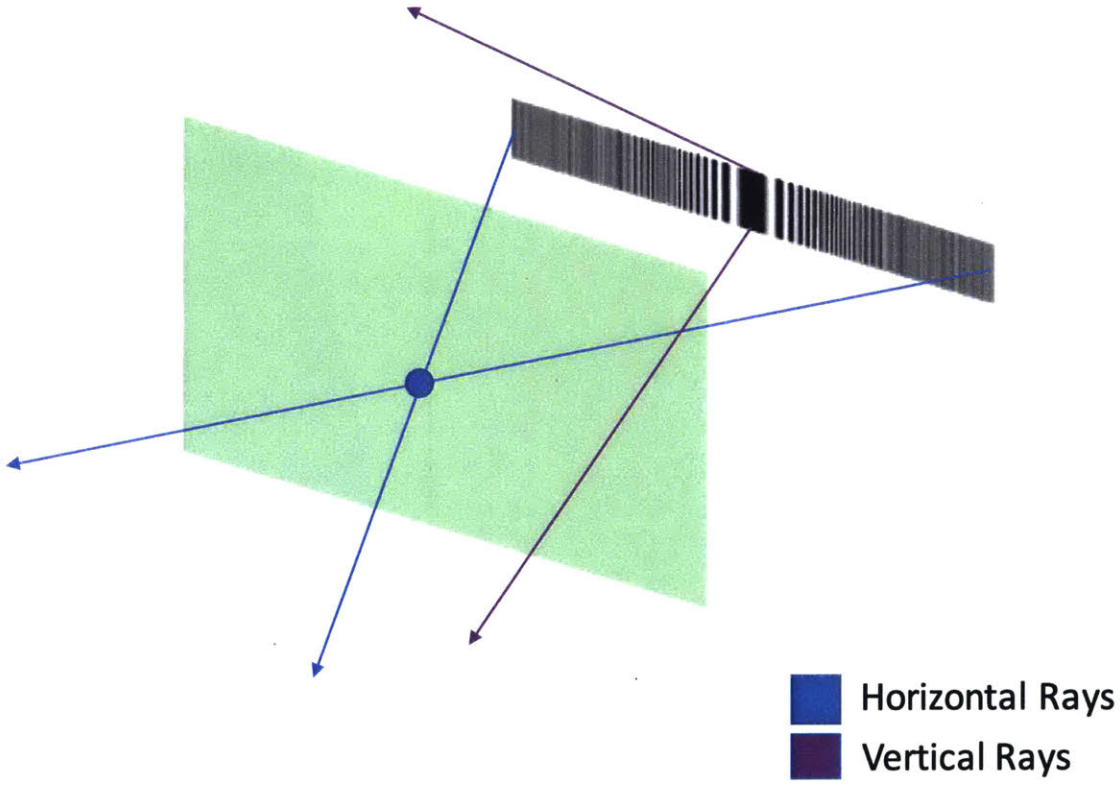

Figure 69: Origin of astigmatism in HPO holographic display systems. Horizontal rays converge to a point at the specific focal distance due to Fresnel diffraction, while vertical rays diverge due to Fraunhofer diffraction from the vertical rectangular aperture.

Horizontal-parallax only (or vertical-parallax only) displays are naturally astigmatic due either to the use of cylindrical optics or 1-D line holograms to form points in depth. For HPO holographic displays, this phenomenon is depicted in Fig. 69 in which horizontal rays from the diffractive chirp converge to a point due to Fresnel diffraction and vertical rays diverge away from the rectangular aperture due to Fraunhofer diffraction.

6.3 SPACE-BANDWIDTH PRODUCT CONSIDERATIONS FOR TILED DISPLAY

The multi-hogel, multi-line instantiation of a holographic display device depicted in Fig. 34 can be envisioned as being implemented as part of a larger, "tiled" display architecture system, in which each "tile" - hereafter referred to as a modulation unit - has some addressable region in both spatial position and angular spectrum over the composite field of view and eyebox. Individual hogels within a single modulation unit can address angles corresponding to and consistent with their individual frequency passbands and necessarily have passband cutoffs. Furthermore, individual hogels within a single modulation unit are separated by spatial gaps due to the limited interaction lengths of the AO interaction. In order to analyze the effects of tiling and gaps on the jointly addressable space/angle space for the 3-D display application, we employ a phase-space description depicted in Figs. 70, 71, 72, and 73.

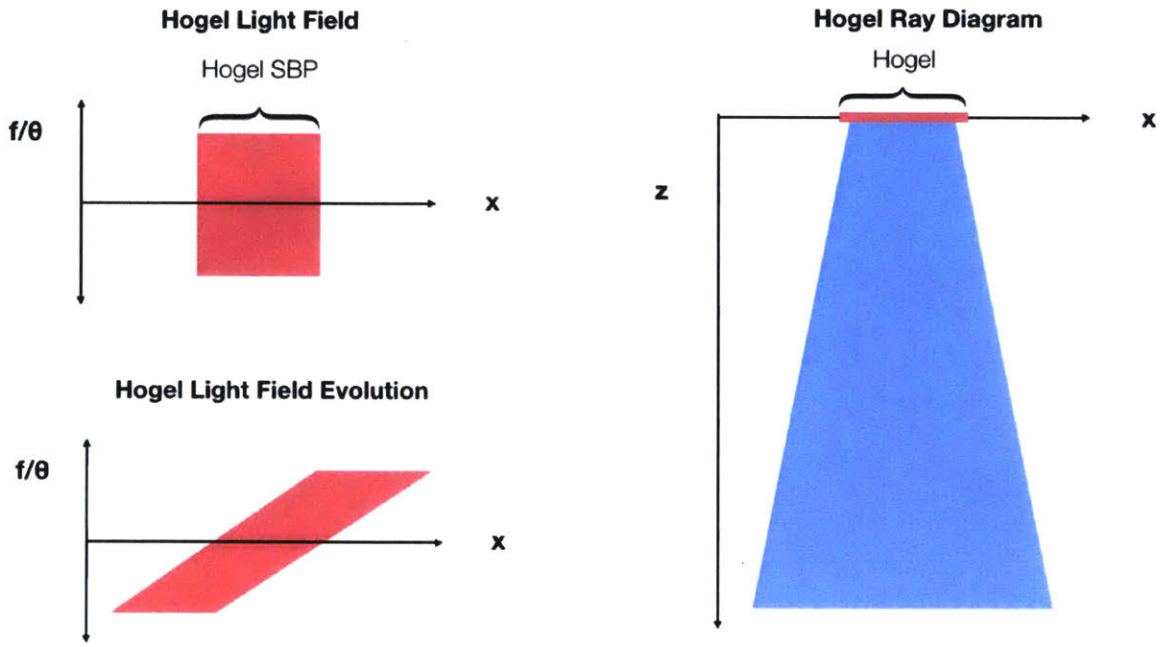

Figure 70: Single hogel space-bandwidth product in phase-space, with associated ray diagram.

In Fig. 70, the "Hogel Light Field" space-bandwidth product is depicted in ray phase-space in which the shaded pink region depicts addressable regions in angle and spatial extent. At the hogel plane, this region is rectangular - indicating that all angles within the angular passband are addressable at every point along the hogel active area. The "Hogel Ray Diagram" indicates the addressable angular and spatial regions of the composite device as light propagates away from the device plane. After propagation away from the device plane, the SBP shears to indicate that the contributions to the composite angular spectrum are no longer uniformly distributed over the spatial extent of the overall optical field, as shown in the "Hogel Light Field Evolution."

In Fig. 71, several hogels with inter-hogel gaps are considered together in the joint light field space. The ray diagram reveals that after a certain distance of propagation, the individual hogels' angular subtense begin to overlap with each other. This is also indicated in

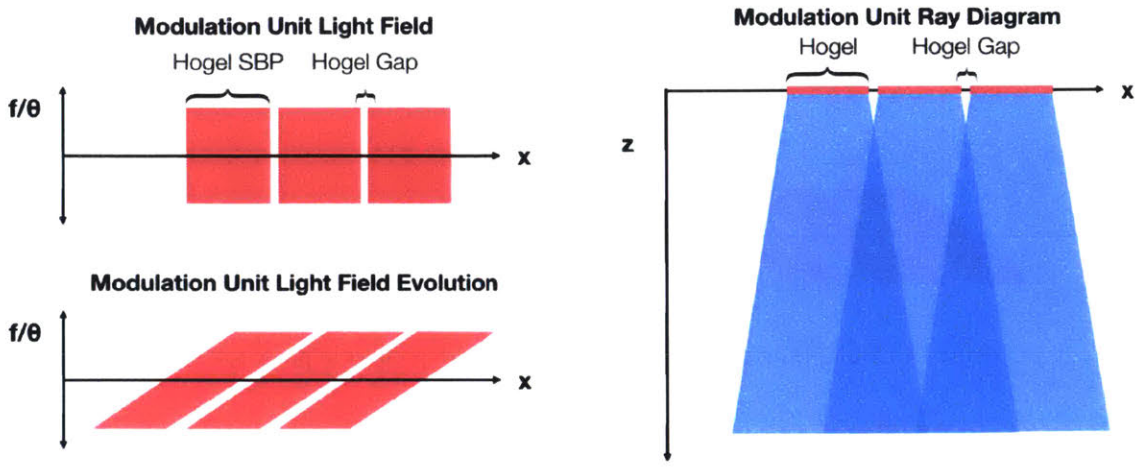

Figure 71: Single modulation unit space-bandwidth product in phase-space, with associated ray diagram.

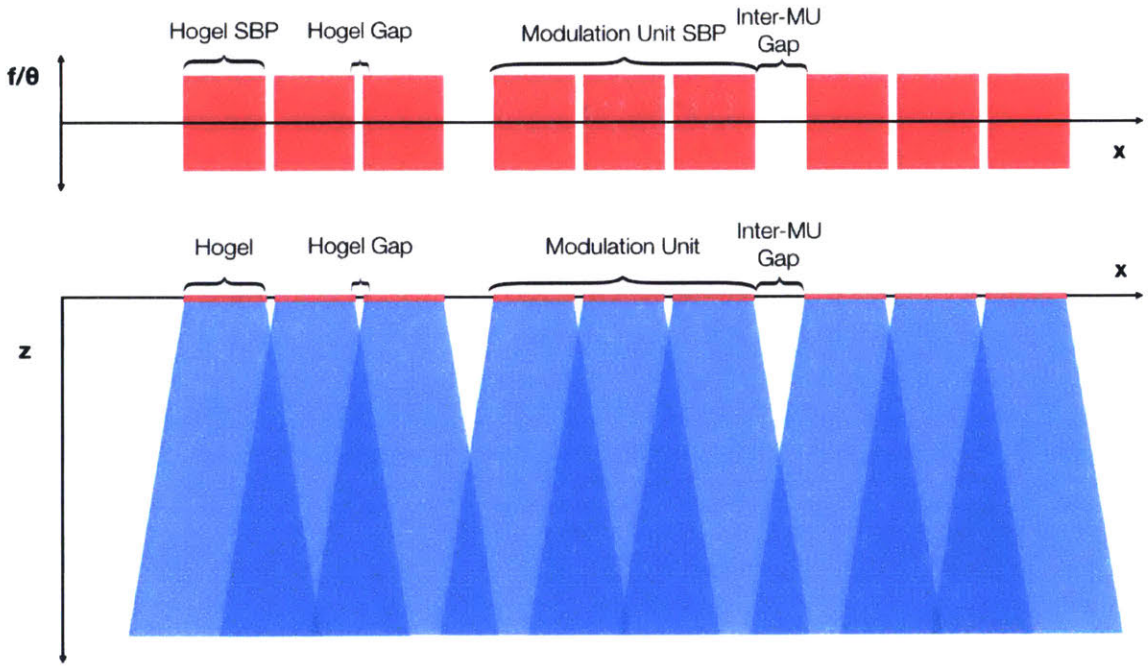

Figure 72: Multiple modulation unit space-bandwidth product in phase-space, with associated ray diagram.

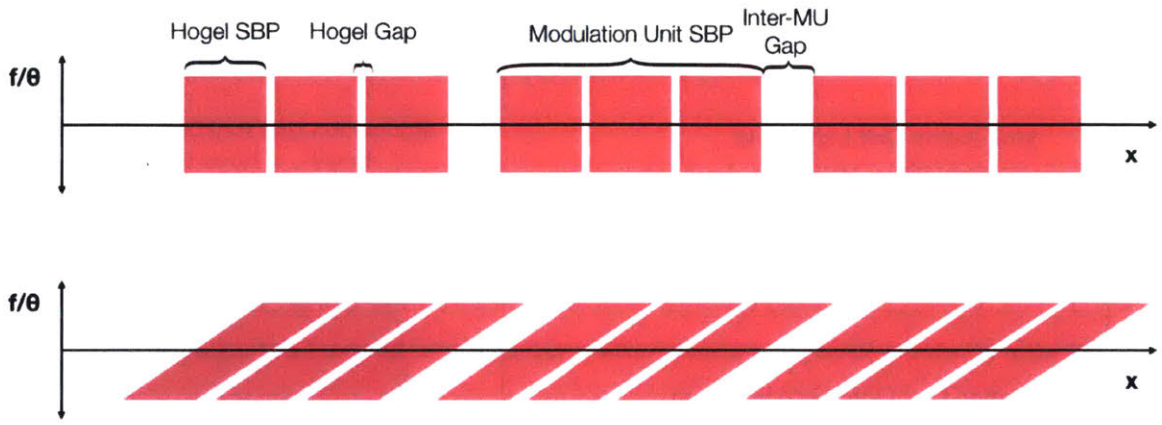

Figure 73: Multiple modulation unit space-bandwidth product in phase-space after propagation.

the light field evolution picture, depicting that the same spatial regions start to become addressable by multiple hogels. The "gap" regions in the light field evolution picture indicate regions of jointly unaddressable space and angle due to the physical limitations on the modulation unit device hogel spacing. Fig. 72 depicts similar behavior in the ray picture when multiple modulation units are tiled together, and Fig. 73 depicts similar behavior in the phase-space after evolution.

Sample MATLAB code for analyzing the evolution of the light field under different instantiations of hogel and modulation unit arrangements is provided in Appendix A.

7

COMPUTATIONAL METHODS FOR NEAR-TO-EYE AND WAVEGUIDE HOLOGRAPHIC DISPLAYS

The information presented in this chapter draws from work initially presented in S. Jolly, D. E. Smalley, J. Barabas, and V. M. Bove, Jr., "Computational architecture for full-color holographic displays based on anisotropic leaky-mode modulators," Proc. SPIE Practical Holography XXVIII, 9006, 2014. [78].

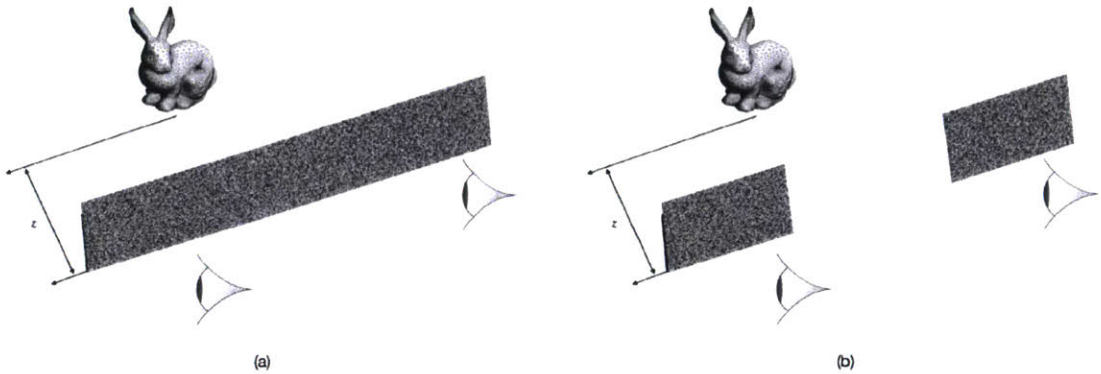

Figure 74: Computational considerations for "double-window-based" display architectures for near-to-eye binocular holographic video displays. (a) Full Fresnel hologram. (b) Windowed Fresnel holograms.

In a general holographic viewing scenario, rays emanating from a single Fresnel hologram or holographic stereogram enter both eyes according to the spatial-spectral distribution of the CGH. In a near-to-eye viewing scenario, however, each eye is effectively perceiving only a small "window" of a larger hologram distribution but the viewer still needs to perceive the correct 3-D distribution. This scenario is depicted in Fig. 74, in which both (a) the presentation of a full Fresnel hologram in a near-to-eye viewing configuration and (b) the presentation of a truncated version of the same Fresnel hologram "windowed" to mirror near-to-eye display geometries. This consideration applies to the computation of computer-generated near-eye holograms over "windowed" regions corresponding to the display eyebox available for each eye. Such windowed holograms per eyebox can be computed either by truncating a larger Fresnel hologram encompassing both eyeboxes, selectively computing said hologram in the eyebox regions of interest, or alternatively, using perspective rendering techniques to selectively sample the scene rays subtended by the eyeboxes and using such subtense to compute the selected holograms via ray-based CGH techniques.

7.1 COMPUTATIONAL METHODS FOR FULL-COLOR DISPLAY

The display architecture depicted in Ch. 3 (accounting for considerations on per-wavelength, acoustic frequency-dependent radiative decay coefficients) can be engineered to be amenable

to full-color display via frequency-division multiplexing, akin to earlier anisotropic leaky-mode devices exhibiting such capability [19]. Here, we present computational techniques for single-sideband modulation of computer-generated holograms also applicable to the near-eye instantiation of anisotropic leaky-mode modulators described here.

Simultaneous and superimposed modulation of red, green, and blue light is accomplished via a frequency-division multiplexing scheme, in which three non-overlapping, multiplexed Fourier-domain sidebands contain the holographic fringe information corresponding to each color channel. This approach requires the generation of single-sideband modulated fringe patterns per color and their Fourier-domain multiplexing in forming an analog signal appropriate for input to the leaky-mode device.

7.2 SINGLE-SIDEBAND MODULATION FOR A FULL-COLOR GENERAL CGH

Holographic fringe information per color channel is appropriately band-limited and translated in frequency to match the multiplexed passbands. We will note that in this context, "band-limited" refers to a computed holographic fringe pattern in which spatial frequencies above a certain threshold (corresponding to the bandwidth of a color passband in the mode-coupling frequency response) are rejected or otherwise not computed. Assuming that this criterion is met during the computation of a general (Fresnel or other interference-based) CGH for display on a leaky-mode modulator supporting frequency division multiplexing, the requisite analog signal for input to the electronic subsystem is formed via single-sideband modulation per color channel and frequency-division multiplexing. The overall process is depicted in Fig. 75.

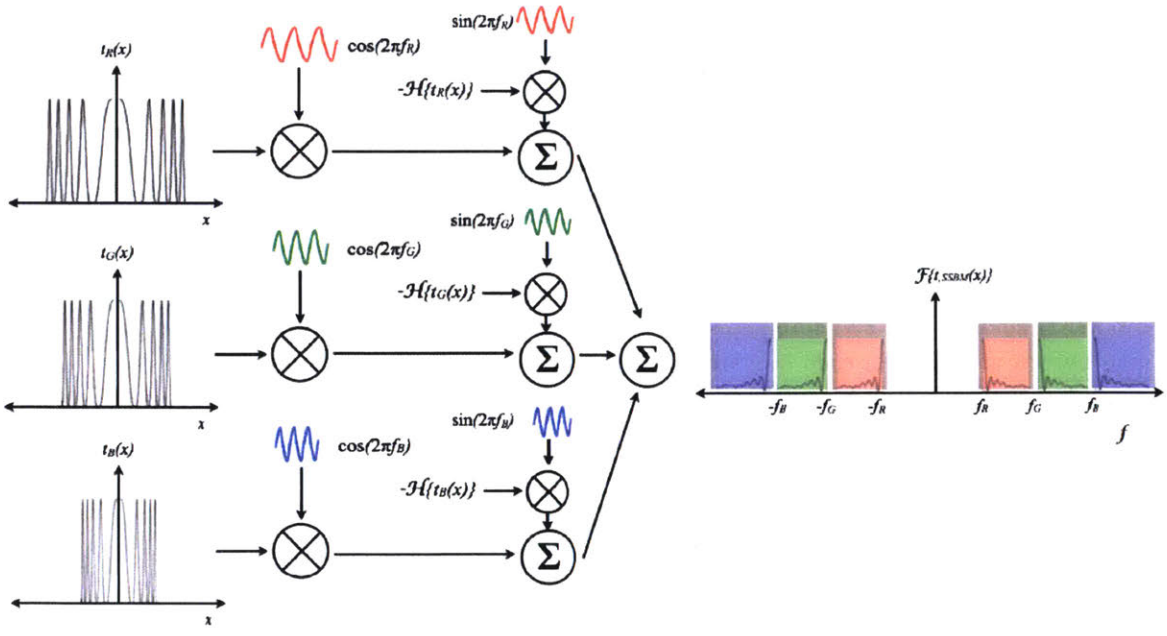

Figure 75: Depiction of single-sideband modulation process and frequency-division multiplexing scheme for generation of appropriate signal for input to a leaky-mode modulator in the case of a general Fresnel CGH.

For a one-dimensional fringe pattern $t(x)$, the single-sideband modulated form $t_{ssb}(x)$ with carrier frequency f_0 is given by

$$t_{ssb}(x) = t(x)\cos(2\pi f_0 x) - \mathcal{H}\{t(x)\}\sin(2\pi f_0 x) \tag{15}$$

where $\mathcal{H}$ denotes Hilbert transformation. The Hilbert transform $\mathcal{H}\{t(x)\}$ is defined as

$$\mathcal{H}\{t(x)\} = \frac{1}{\pi}\,\text{p.v.}\int_{-}\frac{t(x')}{x-x'}dx' \tag{16}$$

where p.v. denotes the Cauchy principal value. Note that Eq. 16 can be expressed as a convolution of the signal $t(x)$ with the kernel $1/\pi x$. Because of numerical issues associated with directly computing the integral in Eq. 16, software-based implementation of single-sideband modulation is often accomplished via a Fourier-domain method in which the Hilbert transform operator $\sigma_H = \mathcal{F}\{1/\pi x\} = j\text{sgn}(2\pi f)$ (where sgn is the Signum function) is multiplicative upon the Fourier transform of $t(x)$. Therefore,

$$\mathcal{F}\left[\mathcal{H}\{t(x)\}\right] = j\text{sgn}(2\pi f)\mathcal{F}\{t(x)\} \tag{17}$$

where $\mathcal{F}$ denotes Fourier transformation and

$$t_{SSB}(x) = t(x)\cos(2\pi f_0 x) - \mathcal{F}^{-1}\left[j\text{sgn}(2\pi f)\mathcal{F}\{t(x)\}\right]\sin(2\pi f_0 x) \tag{18}$$

where $\mathcal{F}^{-1}$ denotes inverse Fourier transformation. This modulation scheme is amenable to software implementation via the Fast Fourier transform.

For computed fringe patterns corresponding to red, green, and blue color channels (e.g., $t_R(x)$, $t_G(x)$, and $t_B(x)$, as shown on the left side of Fig. 75), single-sideband modulation with carrier frequencies corresponding to the lower cutoff frequencies of the color passbands in the mode-coupling device frequency response (e.g., f_R, f_G, and f_B) produces the correctly translated passbands (e.g., $t_{SSB,R}(x)$, $t_{SSB,G}(x)$, and $t_{SSB,B}(x)$). Summation of these three single-sideband modulated fringe patterns as $t_{FDM}(x) = t_{SSB,R}(x) + t_{SSB,G}(x) + t_{SSB,B}(x)$ then produces the composite, frequency-division multiplexed fringe signal for input to the electronic subsystem, as shown on the right side of Fig. 75.

7.3 SINGLE-SIDEBAND MODULATION FOR A FULL-COLOR DIFFRACTION-SPECIFIC COHERENT PANORAMAGRAM

Diffraction-specific stereogram approaches to hologram computation employ hologram discretization in space and spectrum, commonly utilizing holographic elements (or hogels) as primitives. Such a primitive is an analytical or pre-computed 1-D chirped grating (or 2-D Fresnel zone plate, in the case of full-parallax) that is modulated with view information corresponding to the luminance of a scene over the angle space; a fully-populated light field representation of a scene is therefore readily converted to a diffraction-specific holographic stereogram.

The *diffraction-specific coherent panoramagram* is a diffraction-specific approach to multi-view holographic stereogram generation that retains a high degree of the wavefront curvature of a given 3-D scene [94]. The algorithm uses scene depth information, either from

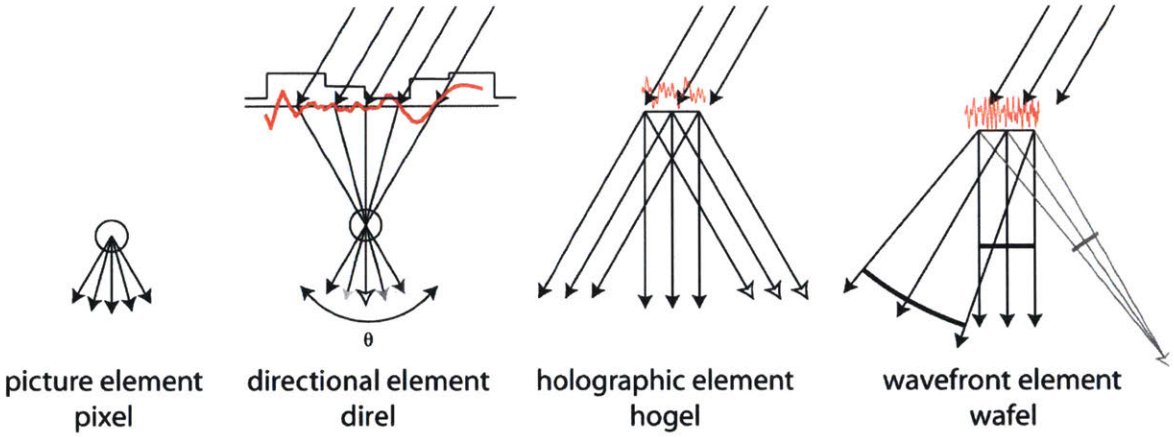

Figure 76: Adapted from [94]. Comparative affordances of the pixel, direl, hogel, and wafel.

a synthetic graphics model or captured via a rangefinding camera [95], to select appropriately chirped holographic gratings for modulation with scene luminance information. Such an approach generates wavefront element primitives, or wafels. The comparative affordances of the wafel relative to those of the pixel, direl, and hogel are depicted in Fig. 76. Relative to conventional holographic elements (hogels) which are limited to producing planar wave curvature with intensity variation per view direction, wafels can produce a higher degree of wavefront curvature per view direction.

Following our earlier derivation [94], the equation specifying the transmittance function $t(x)$ of an unmodulated, chirped holographic grating defining a wafel is

$$t(x) = \cos\left[\frac{2\pi}{\lambda}\left(\sqrt{(x-x_0)^2+z_0^2} - x_0 + x\sin\theta_r\right)\right] \tag{19}$$

where x is the position on the composite hologram transmittance function, (x_0, z_0) is the position of a scene point to be reconstructed, and θ_r is the angle of the reconstruction beam relative to the normal of the hologram plane. Examination of this function reveals that the square root term produces a chirped frequency distribution along x whose chirp rate $\partial f/\partial x$ depends on z_0, the x_0 term produces a phase shift such that $t(x)$ has zero phase at $x = x_0$, and that the $x\sin\theta_r$ term produces a constant frequency dependent on the angle of the reconstruction beam θ_r.

Because the holographic grating is defined by a single cosine functional composition, translating the positive and negative halves of the frequency spectrum by $\pm f_0$ can be accomplished by the addition of an $x\lambda f_0$ term in the cosine argument. The single-sideband modulated form of the chirped grating is then

$$t_{SSB}(x) = \cos\left[\frac{2\pi}{\lambda}\left(\sqrt{(x-x_0)^2+z_0^2} - x_0 + x(\sin\theta_r + \lambda f_0)\right)\right] \tag{20}$$

Computation of the overall wafel proceeds in the normal diffraction-specific fashion, with the wafel's transmittance computed as the multiplication of the single-sideband chirped grating $t_{SSB}(x)$ with a view modulation function $m(x)$. A full-color, frequency-division multiplexed wafel for is computed via a summation as $t_{FDM}(x) = m_R(x)\cdot t_{SSB,R}(x) + m_G(x)\cdot t_{SSB,G}(x) + m_B(x)\cdot t_{SSB,B}(x)$, where $t_{SSB,R}(x)$, $t_{SSB,G}(x)$, and $t_{SSB,B}(x)$ are single-sideband modulated chirped gratings computed for the appropriate illumination

wavelengths λ and (as above, in the case of a general CGH) employing carrier frequencies corresponding to the lower cutoff frequencies of the color passbands in the mode-coupling device frequency response (e.g., f_R, f_G, and f_B). $m_R(x)$, $m_G(x)$, and $m_B(x)$ are view modulation functions per color. Many such frequency-division multiplexed wafels are then spatially multiplexed to form a composite holographic line.

It should furthermore be noted that the process for computing a FDM, full-color wafel depicted above and in Eq. 20 is significantly less computationally expensive than the Hilbert transform method described in the preceding section, and additionally, almost equivalent in computational complexity to the operations required for a non-modulated chirp. The additional benefit of modulation is therefore, almost "free," from a computational perspective.

7.4 SINGLE-SIDEBAND MODULATED HOGEL DERIVATION

The transmittance function of an unmodulated, chirped holographic grating defining a wafel aperture is given as

$$t(x) = \cos\left[\frac{2\pi}{\lambda}\left(\sqrt{(x-x_0)^2+z_0^2} - x_0 + x\sin\theta_r\right)\right] \tag{21}$$

where x is the position on the composite hologram transmittance function, (x_0, z_0) is the position of a scene point to be reconstructed, and θ_r is the angle of the reconstruction beam relative to the normal of the hologram plane.

We derive the single-sideband modulated form of this chirped grating with carrier frequency f_0 from the viewpoint of the analytic signal representation. Given the transmittance function $t(x)$, the analytic signal $t_a(x)$ is given by

$$t_a(x) = t(x) + j\mathcal{H}\{t(x)\} = A(x)e^{j\phi(x)} \tag{22}$$

where $A(x)e^{j\phi(x)}$ is the phasor representation of $t_a(x)$ (comprised of an *instantaneous amplitude* $A(x)$ and *instantaneous phase* $\phi(x)$) and $\mathcal{H}$ denotes Hilbert transformation. We note that this representation allows the Hilbert transform of the signal $t(x)$ to be interpreted as the imaginary part of the phasor $t_a(x)$ and that the relationship

$$\angle t_a(x) = \phi(x) = \tan^{-1}\left(\frac{\mathcal{H}\{t(x)\}}{t(x)}\right) \tag{23}$$

allows for $\mathcal{H}\{t(x)\}$ to be expressed as

$$\mathcal{H}\{t(x)\} = t(x)\tan\phi(x). \tag{24}$$

Noting that the instantaneous phase $\phi(x)$ of $t_a(x)$ is already provided in closed form as

$$\phi(x) = \arg t(x) = \frac{2\pi}{\lambda}\left(\sqrt{(x-x_0)^2+z_0^2} - x_0 + x\sin\theta_r\right), \tag{25}$$

$\mathcal{H}\{t(x)\}$ can be written as

$$\mathcal{H}\{t(x)\} = \cos\left[\frac{2\pi}{\lambda}\left(\sqrt{(x-x_0)^2+z_0^2} - x_0 + x\sin\theta_r\right)\right] \tan\left[\frac{2\pi}{\lambda}\left(\sqrt{(x-x_0)^2+z_0^2} - x_0 + x\sin\theta_r\right)\right]. \quad (26)$$

This reduces to

$$\mathcal{H}\{t(x)\} = \sin\left[\frac{2\pi}{\lambda}\left(\sqrt{(x-x_0)^2+z_0^2} - x_0 + x\sin\theta_r\right)\right]. \quad (27)$$

Given a signal $t(x)$, the single-sideband modulated form $t_{SSB}(x)$ with carrier frequency f_0 is given by

$$t_{SSB}(x) = t(x)\cos(2\pi f_0 x) - \mathcal{H}\{t(x)\}\sin(2\pi f_0 x). \quad (28)$$

Substituting, the relationship becomes

$$t_{SSB}(x) = \cos\left[\frac{2\pi}{\lambda}\left(\sqrt{(x-x_0)^2+z_0^2} - x_0 + x\sin\theta_r\right)\right]\cos(2\pi f_0 x) - \sin\left[\frac{2\pi}{\lambda}\left(\sqrt{(x-x_0)^2+z_0^2} - x_0 + x\sin\theta_r\right)\right]\sin(2\pi f_0 x) \quad (29)$$

which simplifies into the final form of a single-sideband modulated wafel chirp

$$t_{SSB}(x) = \cos\left[\frac{2\pi}{\lambda}\left(\sqrt{(x-x_0)^2+z_0^2} - x_0 + x(\sin\theta_r + \lambda f_0)\right)\right]. \quad (30)$$

8

RESULTS AND CHARACTERIZATION: FEMTOSECOND LASER MICROMACHINED DEVICE ELEMENTS

The information presented in this chapter draws from work initially presented in

1. *Nickolaos Savidis, Sundeep Jolly, Bianca Datta, Michael Moebius, Thrasyvoulos Karydis, Eric Mazur, Neil Gershenfeld, and V. Michael Bove, Jr., "Progress in fabrication of waveguide spatial light modulators via femtosecond laser micromachining," Proc. SPIE Advanced Fabrication Technologies for Micro/Nano Optics and Photonics X, 10115, 2017 [50].*

2. *Bianca C. Datta, Nickolaos Savidis, Michael Moebius, Sundeep Jolly, Eric Mazur, and V. Michael Bove, Jr., "Direct-laser metal writing of surface acoustic wave transducers for integrated-optic spatial light modulators in lithium niobate," Proc. SPIE Advanced Fabrication Technologies for Micro/Nano Optics and Photonics X, 10115, 2017 [79].*

3. *Sundeep Jolly, Nickolaos Savidis, Bianca Datta, Thrasyvoulos Karydis, Will Langford, Neil Gershenfeld, and V. Michael Bove, Jr., "Progress in fabrication of anisotropic Bragg gratings in lithium niobate via femtosecond laser micromachining," Proc. SPIE Advanced Fabrication Technologies for Micro/Nano Optics and Photonics XI, 10554, 2018 [51].*

4. *Sundeep Jolly, Bianca Datta, Vik Parthiban, Daniel Smalley, and V. Michael Bove, Jr., "Experimental characterization of leaky-mode spatial light modulators fabricated by direct laser writing," Proc. SPIE Practical Holography XXXIII: Displays, Materials, and Applications, 10944, 2019 [53].*

8.1 VOLUME BRAGG GRATINGS IN GLASS AND LITHIUM NIOBATE

8.1.1 *Embedding Multilayer Gratings in Glass*

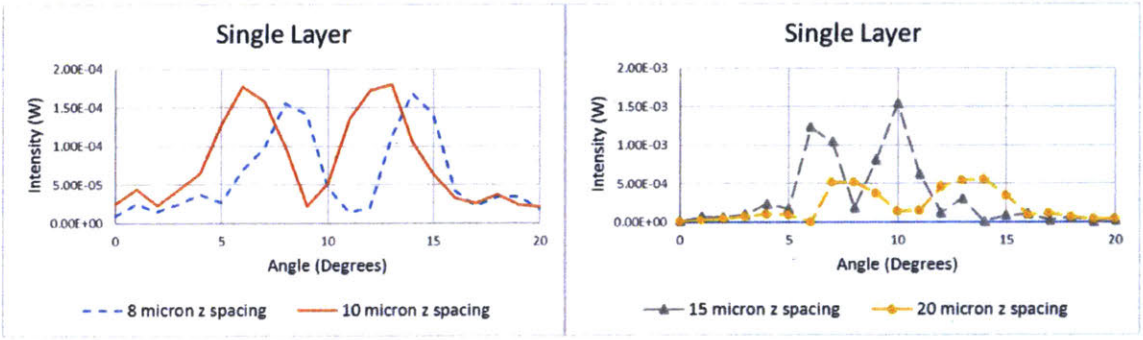

Figure 77: Adapted from [50]. Angular characterization of a single grating layer fabricated in glass.

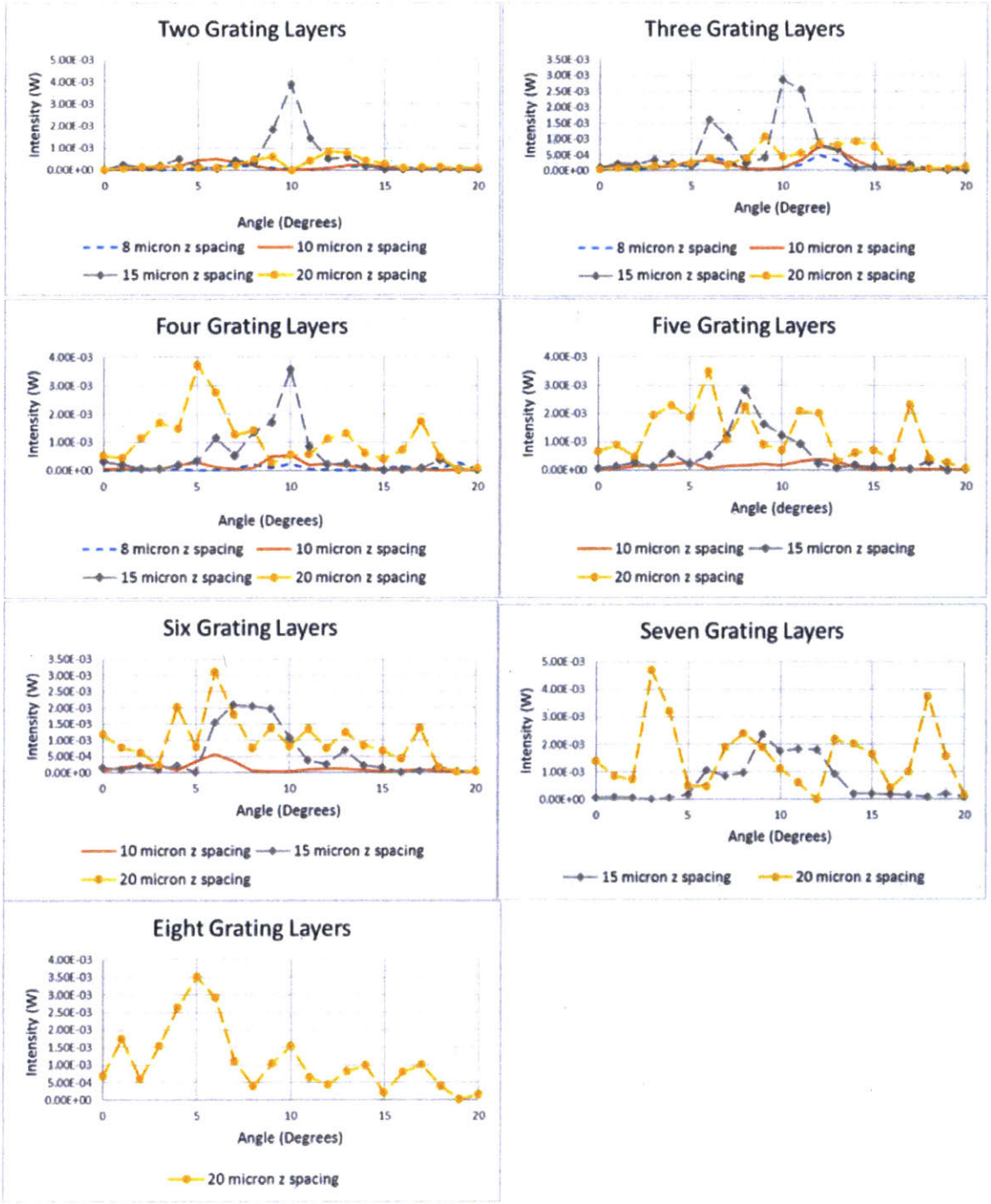

Figure 78: Adapted from [50]. Angular characterization of multilayer gratings fabricated in glass.

As a first order validation of our approach to volumetrically integrate multilayer gratings in transparent media, we integrated volume modifications into glass rather than $LiNbO_3$, with varying inter-layer spacings and number of layers overall, to examine whether a multilayer approach to generating a volume grating is feasible for approximating Bragg-like behavior from an optical volume hologram [50]. These results are depicted in Figs. 77 and 78.

8.1.2 *Embedding Surface and Volume Phase Gratings in Lithium Niobate*

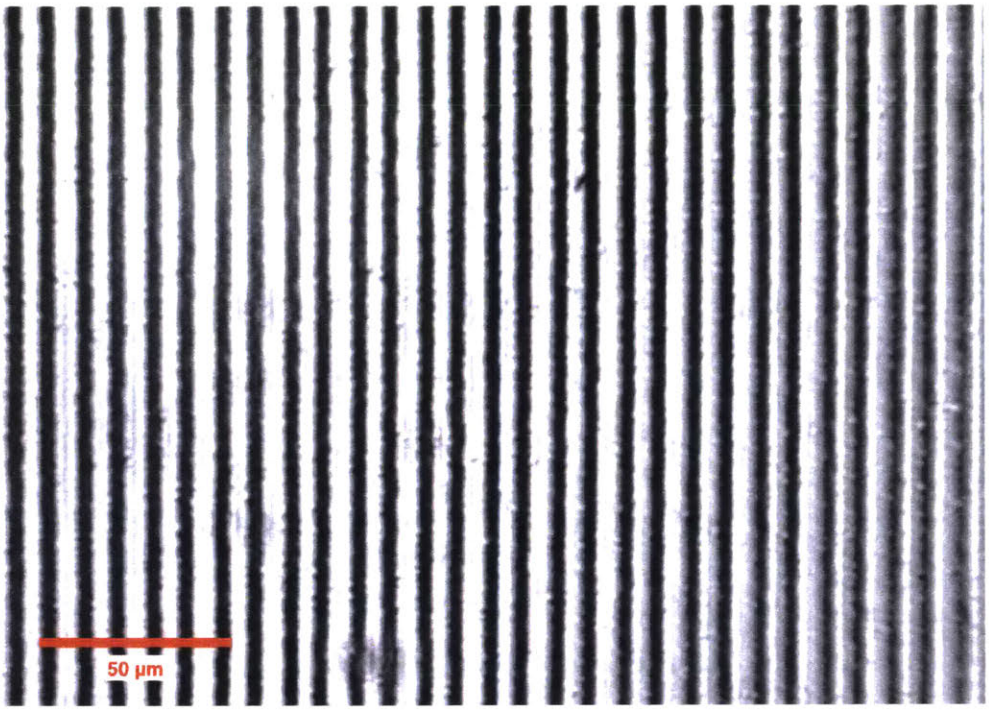

Figure 79: Optical micrograph of surface grating with $\Lambda = 10\ \mu$m fabricated on $LiNbO_3$ surface.

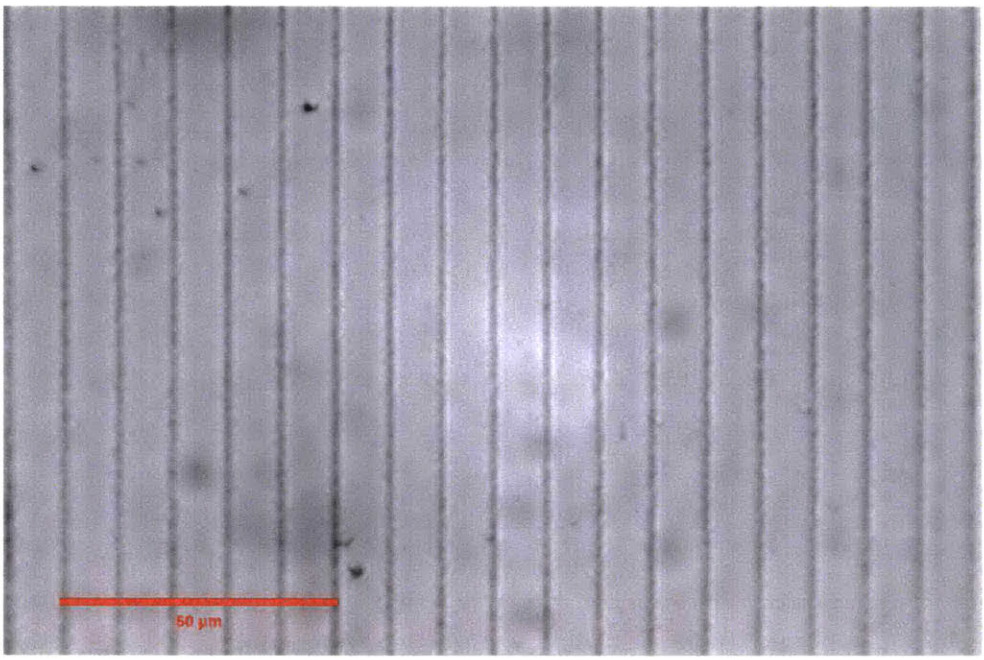

Figure 80: Optical micrograph of volume phase grating with $\Lambda = 10\ \mu$m and thickness $t = 50\ \mu$m fabricated 150 μm below the $LiNbO_3$ surface.

Fig. 79 depicts an optical micrograph of a surface grating with $\Lambda = 10$ μm and Fig. 80 depicts the top surface of a volume transmission phase grating with $\Lambda = 10$ μm and thickness $t = 50$ μm fabricated 150 μm below the $LiNbO_3$ surface, with layer thickness chosen to be 5 μm to correspond to a longer axial spot size. The $1/e^2$ lateral spot size emerging at the focus of the objective is measured to be 2.5 μm.

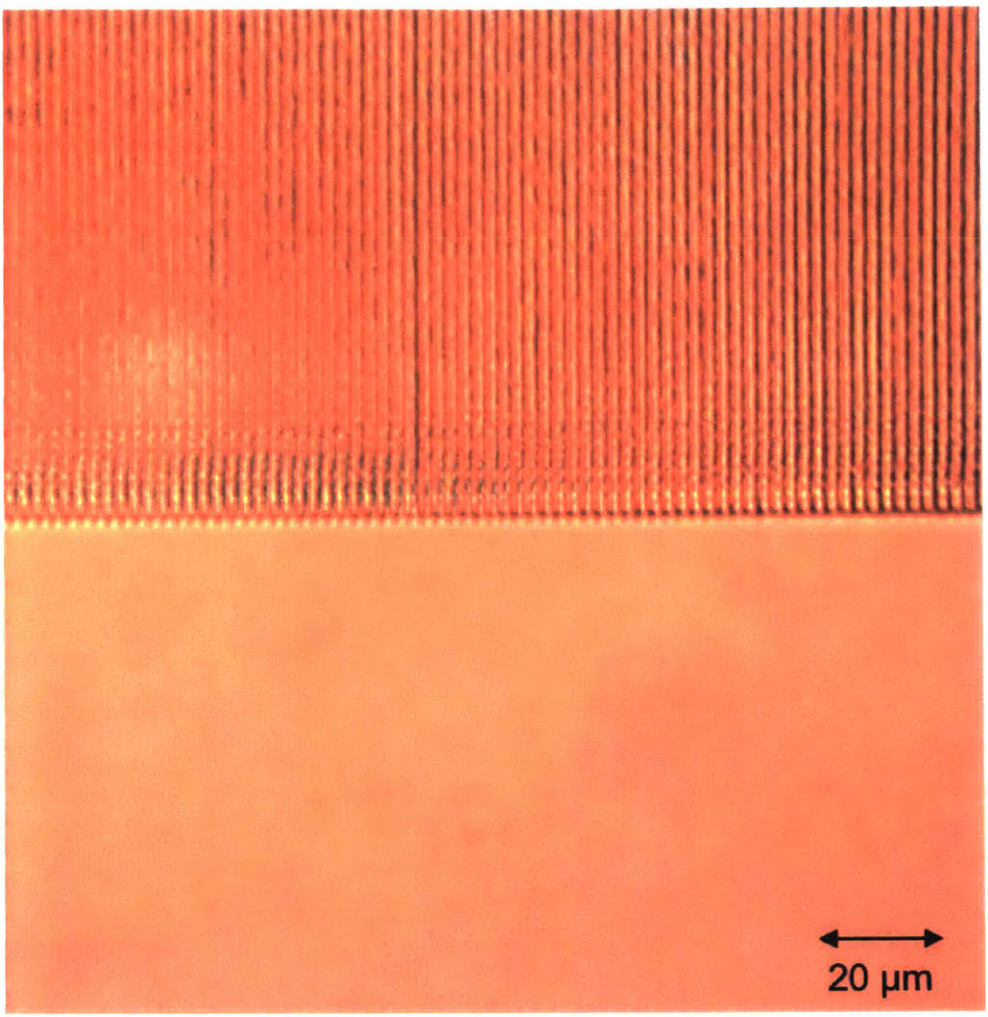

Figure 81: Fabricated volume Bragg gratings with $\Lambda = 2$ μm, $N = 20$ layers, and layer spacing 2.5 μm.

For the current experiments, we operate the fs laser at the operating wavelength $\lambda = 515$ nm, with a pulse repetition rate of 100 kHz, a pulse energy of 2 μJ (average laser power $P = 200$ mW), and a stage translation velocity of 5 mm/s. For finely pitched gratings (e.g., $\Lambda < 5$ μm), a high-resolution NA=0.7 microscope objective is used. For volume Bragg gratings, grating layers are spaced in depth by 2.5 μm, and gratings are fabricated 100 μm below the $LiNbO_3$ surface.

Figs. 81 and 82 depict fabricated volume Bragg gratings, with $\Lambda = 2$ μm. These gratings are comprised of 20 layers, written in a bottom-to-top fashion, with a nominal "line" feature dimension < 1 μm (dictated by the nominal diffraction-limited spot size indicated

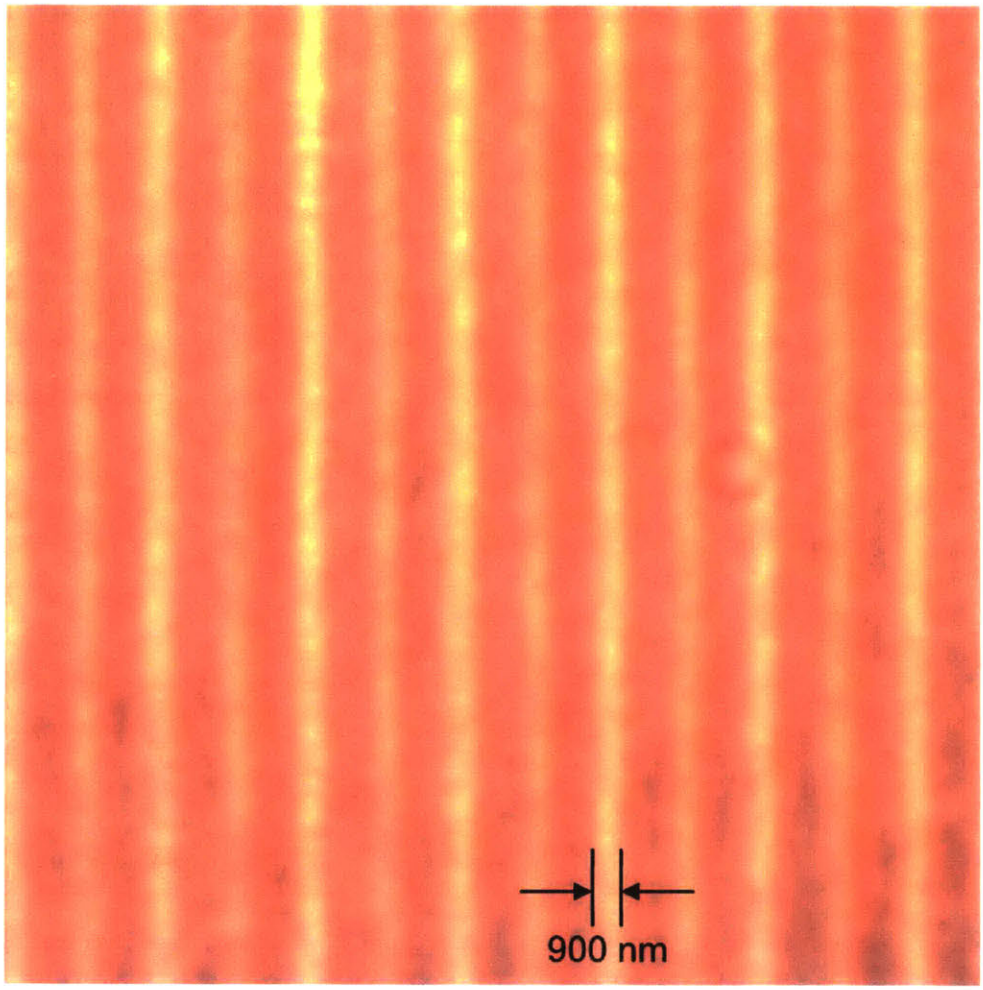

Figure 82: Fabricated volume Bragg gratings with $\Lambda = 2\ \mu$m, $N = 20$ layers, and layer spacing $2.5\ \mu$m.

by the numerical aperture of the writing objective).

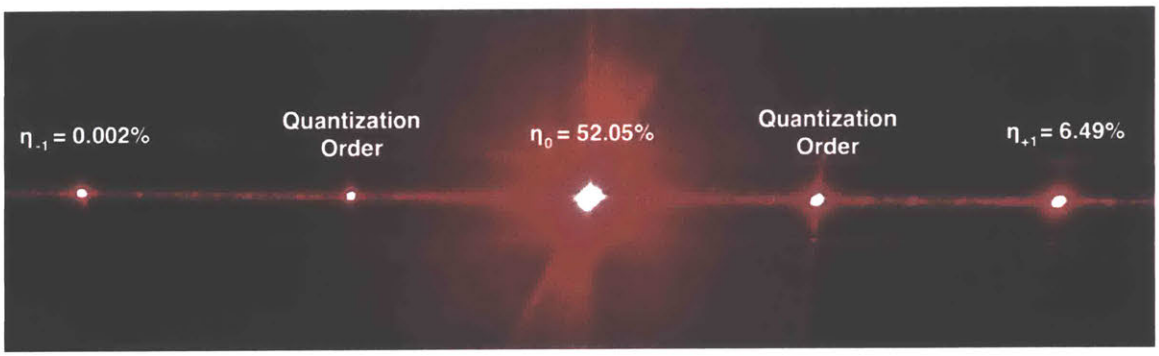

Figure 83: Bragg grating characterization with laser beam incident at Bragg angle and resulting asymmetric diffraction profile, depicting very strong energy transfer into the +1st diffracted order at the expense of energy transferred into other orders.

Fig. 83 depicts characterization of the fabricated Bragg gratings, showing asymmetric effects in volume diffraction when a laser beam at $\lambda = 633$ nm is incident upon the grating at the Bragg angle $\gamma_B = \sin^{-1}\left(\frac{\lambda}{2\Lambda}\right) = 9.1°$. Note that the diffraction pattern observed is strongly asymmetric at Bragg incidence for the input beam direction, consistent with a thick grating exhibiting diffraction in the Bragg regime.

8.2 SAW TRANSDUCERS

8.2.1 *LIFT and Ablation Morphology Results*

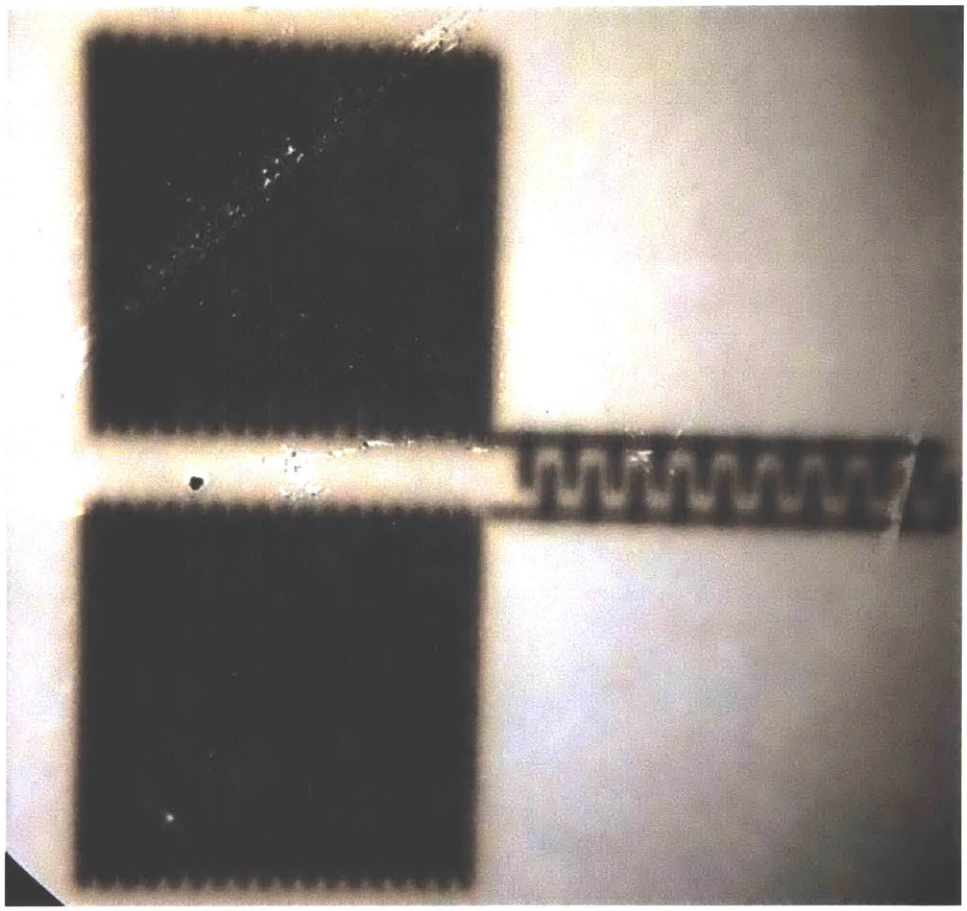

Figure 84: Optical micrograph of a gold transducer deposited via LIFT.

Fig. 84 depicts a fabricated transducer using laser-induced forward transfer with a gold alloy as the thin film to be transferred. Note that the metal edges are relatively ill-defined, and regions between adjacent laser passes appear somewhat disjoint, possibly affecting the functionality of such a device. In practice, the use of LIFT generated structures with poor adhesive properties to the acceptor substrate with a tendency to fall off when probed [79].

Fig. 85 depicts a fabricated transducer using femtosecond laser ablation. Here, the transducer period is $\Lambda = 25\mu$m. Note that, in contrast to using LIFT-based methods, this transducer has excellent surface morphology and retains good adhesion to the carrier substrate.

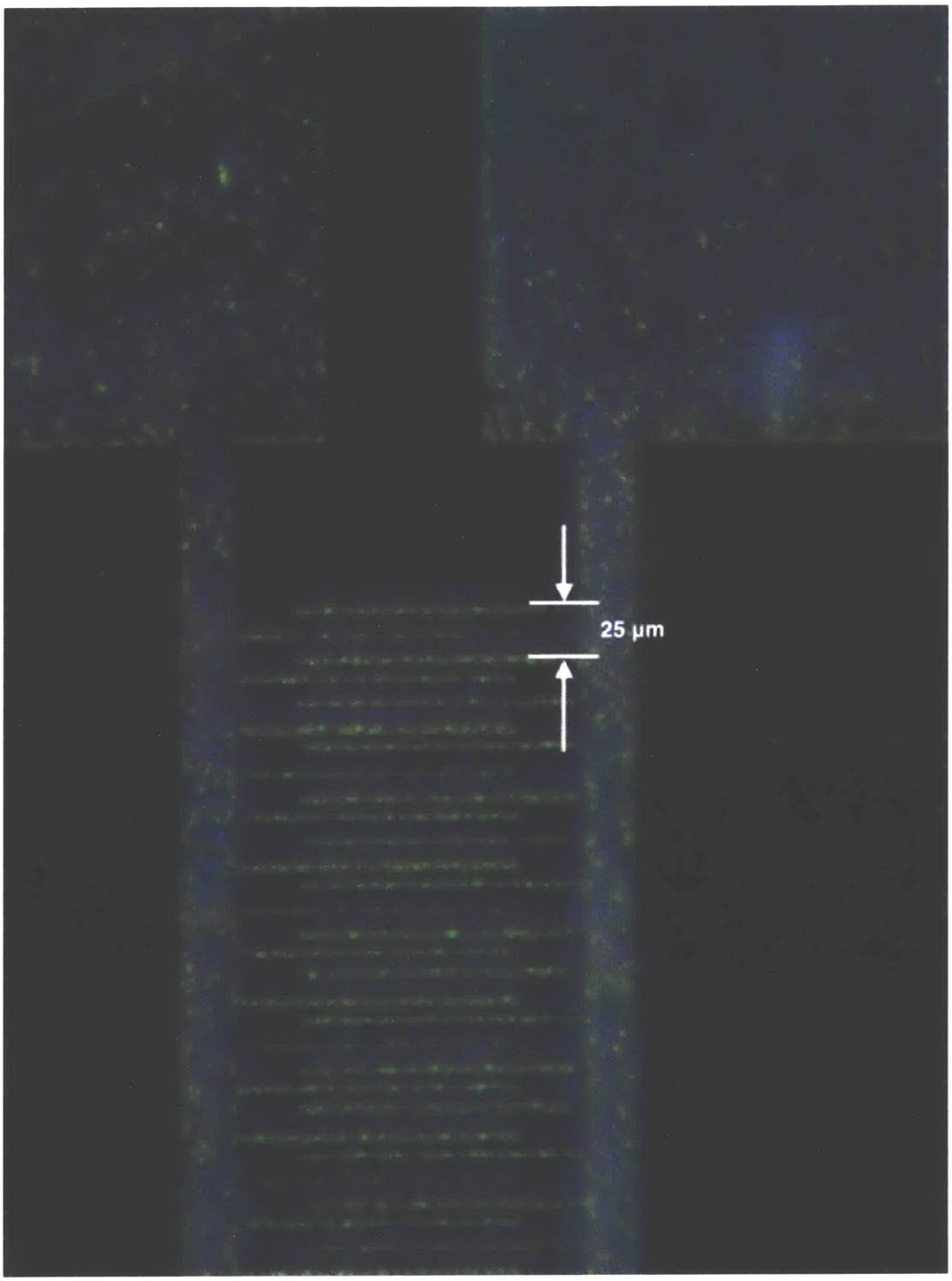

Figure 85: Optical micrograph of an ablated aluminum transducer on lithium niobate.

8.3 WAVEGUIDES

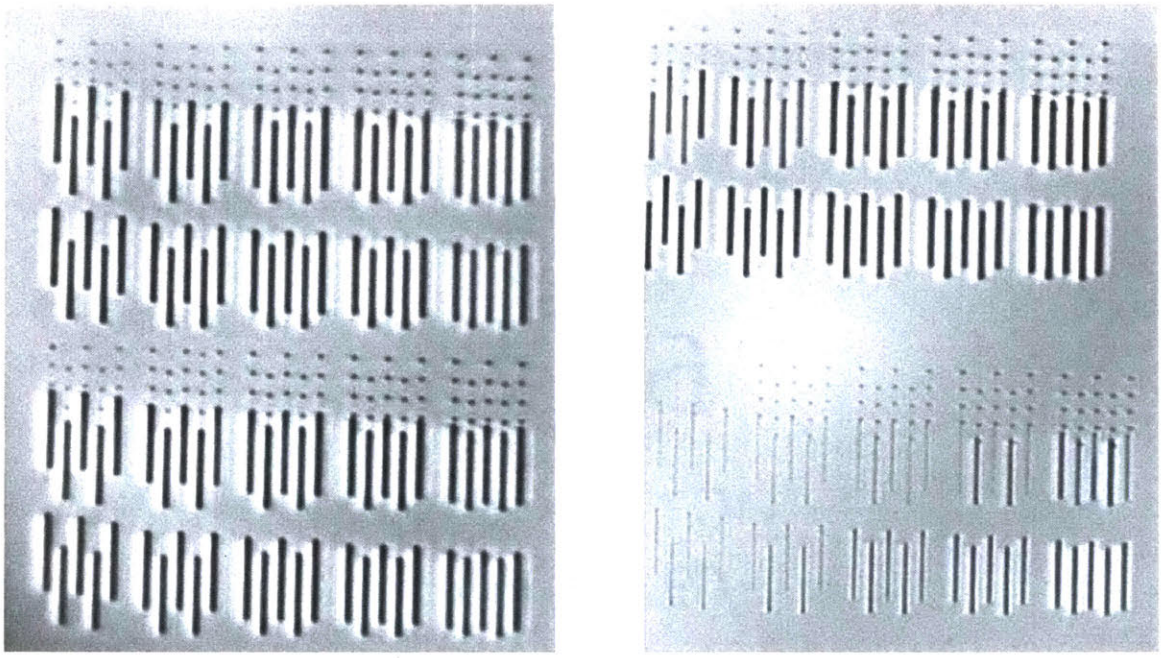

Figure 86: Adapted from [50]. Femtosecond laser micromachined waveguides in lithium niobate.

Fig. 86 depicts results of waveguides directly patterned in x-cut lithium niobate [51]. Details of the fabrication methodology are presented in Savidis, *et. al.*„ but it should be noted that we did not directly measure index contrast. The results indicated for surface and volume gratings above are also indicative of the index contrast and waveguide channel morphology achievable with this fabrication methodology (as a single grating line can be interpreted as a waveguide channel).

9

CONCLUSIONS AND FUTURE WORK

This thesis has presented a new modality for transparent, flat-panel electroholographic display requiring no supporting optics and has depicted motivations and methodologies for fabricating scalable displays of this manner via femtosecond laser micromachining. In this chapter, a discussion of current results and avenues for future work with respect to device-scale feature integration, validation, and systems-level scale-up is presented.

9.1 DISCUSSION ON FEMTOSECOND LASER MICROMACHINING TECHNIQUES FOR DEVICE FABRICATION

9.1.1 *Components - Direct Laser Writing Not Useful or Practical*

1. *LIFT-based metal transfer.* Our experimentation with the LIFT process has shown that the patterned structure morphology is easily damaged, making electrical contact with the written structures via wirebonding or other contact methods extremely difficult or impossible [79]. Furthermore, although this work does not present experimentation for validation, the poor surface adhesion may influence the electromechanical coupling performance of the IDT for SAW transduction. Lastly, LIFT for aluminum (the preferred material for IDTs) patterning is usually problematic due to oxidation.

2. *Laser-written waveguides.* Our analysis of the mode-coupling performance of laser-written waveguides, assuming the highest achievable index contrast reported in the literature, indicates several disadvantages of directly-written guides vs. those fabricated via proton exchange methods: 1) a roughly order-of-magnitude decrease in the radiative decay coefficient, and thereby much less theoretically-predicted diffraction efficiency in the guided-to-leaky mode transition, and 2) an overlap of the acoustic frequency-dependence of the coupling coefficients for red, green, and blue light - making earlier proven frequency-division multiplexing techniques impractical for laser-written guides.

9.1.2 *Proven Success or Promise*

1. *Ablative metal patterning.* We have successfully demonstrated the ablative metal patterning of aluminum via the femtosecond laser process, with good morphology in IDTs with periods up to 25 μm. However, smaller features for ablation are currently unproven - either in this work or in the existing literature - using femtosecond lasers having a minimum pulse duration > 200 fs. The initial experimentation with using higher-NA objectives for smaller feature dimensions in the metal patterning proved unsuccessful, with the ablated surfaces exhibiting poor morphology. It should be noted that since metal ablation is largely a thermal process, the pulse duration has a strong effect on the precision of the ablated region [107] and it is possible that our current experimental setup is limited in its ability to achieve smaller ablated

features due to the 210 fs minimum pulse duration of the Pharos laser used. Further optimization of ablated metal features will require a detailed study of the influence of pulse duration and peak energy on the ablation performance. Also note that acoustic frequency ranges most efficient in mode-coupling interactions for proton-exchanged waveguides are on the order of several hundred MHz, and therefore necessitate a transducer period $\Lambda < 15\mu$m - smaller than the proven period of ablated transducers in this thesis and elsewhere in the literature [69].

2. *Volume Bragg grating fabrication.* Direct laser writing, aside from two-beam holographic recording, is a key method for integrating refractive index features into the volume of transparent media, like $LiNbO_3$. We have demonstrated the volumetric integration of simple, planar volume gratings in lithium niobate via femtosecond laser micromachining, and our results indicate a strongly asymmetric angular spectrum response. It should be noted that direct laser writing for volume gratings in this fashion is not restricted to planar gratings, however; as shown in Fig. 39, arbitrary (even aperiodic) structures can be fabricated in this fashion, opening up the possibility for several post-processing optical functions, such as pupil expansion or polarization mode-selection.

3. *Proton-exchanged waveguides.* Because of the superior index contrast and smooth profile achievable with proton-exchanged waveguides, mode-coupling performance, waveguide losses and field confinement, and in-guide scattering are all greatly improved relative to direct laser-written guides. We therefore make the argument that while direct laser ablation can be used to generate a suitable metal mask for patterning the channel waveguide prior to the indiffusion process, it is much less advantageous to use direct laser writing for the waveguide contrast directly.

9.2 FUTURE WORK

This thesis has laid out a motivation for considering near-to-eye holovideo displays for augmented reality and depicted a sample guided-wave acousto-optic architecture for realizing such a display in a completely monolithic fashion requiring no discrete elements like lenses, projectors, or pixelated spatial light modulators. Additionally, it depicts theoretical examinations into device and system performance and presents a sample device fabrication modality based entirely around femtosecond laser micromachining. However, the complete demonstration of the monolithic device scale integration is unproven at the time of this writing.

Based on the fabrication recommendations above, future work should encompass device-level integration of all features using a mix of conventional techniques (electron-beam lithography for IDT patterning and proton exchange for waveguide indiffusion, as depicted in [19]) combined with direct laser-write techniques (femtosecond structuring of volume gratings inside the volume of the media, and possibly for patterning of masks for the waveguide indiffusion process). It should also be noted that this thesis does not definitely recommend against the use of ablative metal femtosecond writing for IDT fabrication, but that a more careful study of ablative performance in resulting IDT morphology based on *e.g.*, pulse duration, is required.

After hogel-level device performance has been validated, future work should include investigations into systems integration depicted in Ch. 3 of this thesis, including: optimization of illumination, drive schemes for large-scale displays, monolithic fabrication of large-scale displays, and optimization of power consumption and display uniformity.

9.3 CONCLUSION

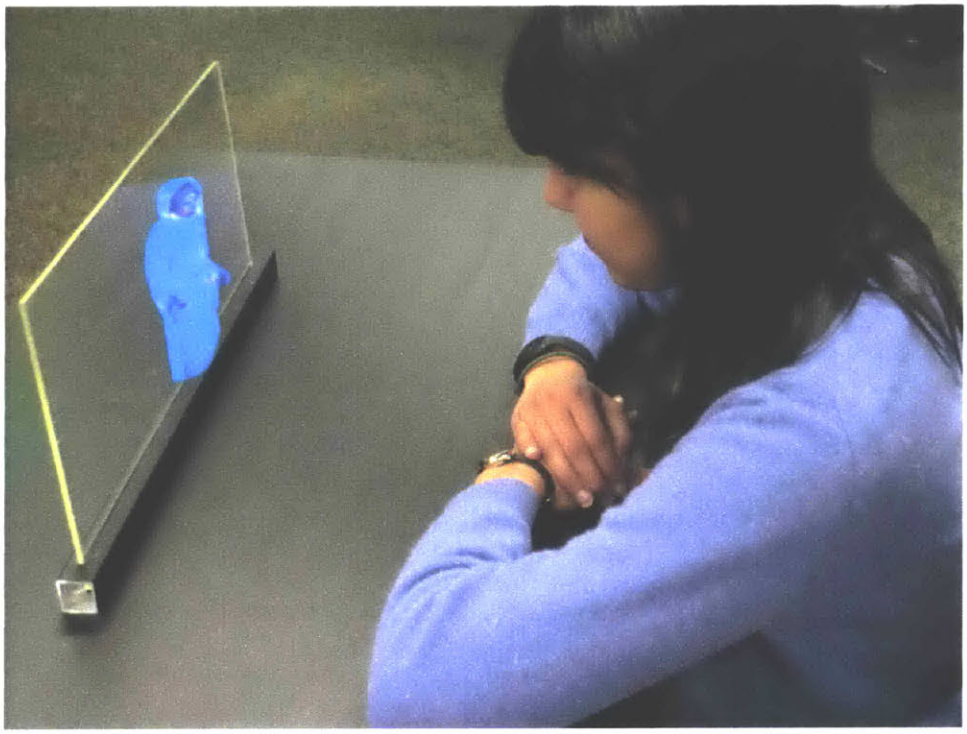

Figure 87: Simulated depiction of holographic transparent flat-panel display requiring no supporting optics.

Electroholographic displays have the potential to alleviate vergence-accommodation conflicts in near-to-eye display systems. Of competing enabling technologies for near-to-eye electroholography, guided-wave acousto-optics with face-emitting, holographically reconstructed outputs can potentially provide the requisite space-bandwidth product required for a comfortable viewing eyebox and large field-of-view while simultaneously reducing overall system bulk and complexity by employing completely monolithic platforms for light modulation and processing.

In this work, we have depicted, theoretically analyzed, and laid out a path for scalable fabrication of such a face-emitting platform for spatial light modulation in electroholography, having several key advantages over edge-emitting or other face-emitting instantiations.

It is hoped that the work presented in this thesis will eventually lead to progress in the development of scalable, transparent, flat-panel holographic displays in a variety of instantiations, including desktop-class displays of the type pictured in Fig. 87.

a

MATLAB SCRIPTS FOR ANALYSIS AND DESIGN

A.1 FRESNEL-TRANSFORMING GERCHBERG-SAXTON ALGORITHM

Listing 1: Fresnel-Transforming Gerchberg Saxton Algorithm

```
close all; clear all;

lambda = 532e-9;
k = 2*pi/lambda;

% Define hologram plane + pupil windows
pixelPitch = 5e-6;
pixelsPerHologramX = 8192;
pixelsPerHologramY = 8192;
totalSamplesX = pixelsPerHologramX;
totalSamplesY = pixelsPerHologramY;
totalArray = zeros(totalSamplesY, totalSamplesX);
Tx = totalSamplesX * pixelPitch;
Ty = totalSamplesY * pixelPitch;
xDomain = -(Tx/2):pixelPitch:(Tx/2-pixelPitch);
yDomain = -(Ty/2):pixelPitch:(Ty/2-pixelPitch);
fxDomain = (-1/Tx * totalSamplesX/2):(1/Tx):(1/Tx * totalSamplesX/2 - 1/Tx);
fyDomain = (-1/Ty * totalSamplesY/2):(1/Ty):(1/Ty * totalSamplesY/2 - 1/Ty);

% Define object point cloud
plane1 = (imread('logo1.png'));
plane2 = (imread('logo2.png'));
plane3 = (imread('logo3.png'));
plane1Rescale = imresize(plane1,0.5);
plane2Rescale = imresize(plane2,0.5);
plane3Rescale = imresize(plane3,0.5);
paddedPlane1 = padarray(plane1Rescale,[(totalSamplesY-size(plane1Rescale,1))
    /2,ceil((totalSamplesX-size(plane1Rescale,2))/2)],'both');
paddedPlane2 = padarray(plane2Rescale,[(totalSamplesY-size(plane1Rescale,1))
    /2,ceil((totalSamplesX-size(plane1Rescale,2))/2)],'both');
paddedPlane3 = padarray(plane3Rescale,[(totalSamplesY-size(plane1Rescale,1))
    /2,ceil((totalSamplesX-size(plane1Rescale,2))/2)],'both');
paddedPlane1 = paddedPlane1(:,1:8192);
paddedPlane2 = paddedPlane2(:,1:8192);
paddedPlane3 = paddedPlane3(:,1:8192);

numIterations = 100;

zPlane1 = 0.3333333;
zPlane2 = 0.6666666;
zPlane3 = 1;

initPhase = (rand(pixelsPerHologramX, pixelsPerHologramY)*2*pi)-pi;
complexFieldPlane3 = exp(j.*initPhase);
complexFieldPlane3 = fresnelProp(complexFieldPlane3,0,lambda,fxDomain,fyDomain
    ,0);

hologramPhaseVideoObject = VideoWriter('hologramPhaseEvolution.avi');
intensityPlane1VideoObject = VideoWriter('intensityEvolutionPlane1.avi');
intensityPlane2VideoObject = VideoWriter('intensityEvolutionPlane2.avi');
intensityPlane3VideoObject = VideoWriter('intensityEvolutionPlane3.avi');
hologramPhaseVideoObject.FrameRate = 10;
intensityPlane1VideoObject.FrameRate = 10;
intensityPlane2VideoObject.FrameRate = 10;
```

```
intensityPlane3VideoObject.FrameRate = 10;
open(hologramPhaseVideoObject);
open(intensityPlane1VideoObject);
open(intensityPlane2VideoObject);
open(intensityPlane3VideoObject);

for iterationIndex = 1:numIterations
    disp(['Computing iteration ' num2str(iterationIndex) '...']);
    complexFieldPlane3 = double(paddedPlane3).*exp(j.*angle(complexFieldPlane3
    ));
    disp('Backpropagating to plane 2...');
    complexFieldPlane2 = fresnelProp(complexFieldPlane3,-abs(zPlane3-zPlane2),
    lambda,fxDomain,fyDomain,1);
    disp('Done!');
    disp('Amplitude enforcement at plane 2...')
    complexFieldPlane2 = double(paddedPlane2).*exp(j.*angle(complexFieldPlane2
    ));
    disp('Done!');
    disp('Backpropagating to plane 1...');
    complexFieldPlane1 = fresnelProp(complexFieldPlane2,-abs(zPlane2-zPlane1),
    lambda,fxDomain,fyDomain,1);
    disp('Done!');
    disp('Amplitude enforcement at plane 1...');
    complexFieldPlane1 = double(paddedPlane1).*exp(j.*angle(complexFieldPlane1
    ));
    disp('Done!');
    disp('Backpropagating to hologram plane...');
    complexFieldPlaneH = fresnelProp(complexFieldPlane1,-abs(zPlane1),lambda,
    fxDomain,fyDomain,1);
    disp('Done!');
    disp('Equalization at hologram plane...');
    complexFieldPlaneH = exp(j.*angle(complexFieldPlaneH));
    disp('Done!');
    figure(1); imagesc(xDomain,yDomain,angle(complexFieldPlaneH)); xlabel('x(m
    )'); ylabel('y(m)'); title('Phase distribution of optimized hologram');
    colormap gray;
    disp('Forward propagating to plane 1...');
    complexFieldPlane1 = fresnelProp(complexFieldPlaneH,abs(zPlane1),lambda,
    fxDomain,fyDomain,1);
    disp('Done!');
    % Compute statistics @ plane 1, save intensity to file
    figure(2); imagesc(xDomain,yDomain,abs(complexFieldPlane1).^2); xlabel('x
    (m)'); ylabel('y(m)'); title('Intensity arriving at plane 1'); colormap
    gray;
    disp('Amplitude enforcement at plane 1...');
    complexFieldPlane1 = double(paddedPlane1).*exp(j.*angle(complexFieldPlane1
    ));
    disp('Done!');
    disp('Forward propagating to plane 2...');
    complexFieldPlane2 = fresnelProp(complexFieldPlane1,abs(zPlane2-zPlane1),
    lambda,fxDomain,fyDomain,1);
    % Compute statistics @ plane 2, save intensity to file
    figure(3); imagesc(xDomain,yDomain,abs(complexFieldPlane2).^2); xlabel('x
    (m)'); ylabel('y(m)'); title('Intensity arriving at plane 2'); colormap
    gray;
    disp('Done!');
    disp('Amplitude enforcement at plane 2...');
    complexFieldPlane2 = double(paddedPlane2).*exp(j.*angle(complexFieldPlane2
    ));
    disp('Done!');
    disp('Forward propagating to plane 3...');
    complexFieldPlane3 = fresnelProp(complexFieldPlane2,abs(zPlane3-zPlane2),
    lambda,fxDomain,fyDomain,1);
    % Compute statistics @ plane 3, save intensity to file
    figure(4); imagesc(xDomain,yDomain,abs(complexFieldPlane3).^2); xlabel('x
    (m)'); ylabel('y(m)'); title('Intensity arriving at plane 3'); colormap
    gray;
    disp('Done!');
    saveas(1,['hologramPhase_' num2str(iterationIndex) '.png']);
    saveas(2,['intensityPlane1_' num2str(iterationIndex) '.png']);
```

```
    saveas(3,['intensityPlane2_' num2str(iterationIndex) '.png']);
    saveas(4,['intensityPlane3_' num2str(iterationIndex) '.png']);
    writeVideo(hologramPhaseVideoObject,getframe(1));
    writeVideo(intensityPlane1VideoObject,getframe(2));
    writeVideo(intensityPlane2VideoObject,getframe(3));
    writeVideo(intensityPlane3VideoObject,getframe(4));
    disp(['Done with iteration ' num2str(iterationIndex) '!']);
end

close(hologramPhaseVideoObject);
close(intensityPlane1VideoObject);
close(intensityPlane2VideoObject);
close(intensityPlane3VideoObject);

hologramPhaseNormalized = (angle(complexFieldPlaneH) - min(min(angle(
    complexFieldPlaneH)))) ./ max(max((angle(complexFieldPlaneH) - min(min(
    angle(complexFieldPlaneH))))));
imwrite(hologramPhaseNormalized,'hologramPhaseNormalizedGS.png');

function [outField] = fresnelProp(inField,z,lambda,fx_u,fy_u,s)
    H = zeros(size(inField));
    for index1 = 1:size(inField,1)
        for index2 = 1:size(inField,2)
            H(index1,index2) =  exp(1i*2*pi*(z/lambda)*sqrt(1.-(lambda.*fx_u(
    index2)).^2-(lambda.*fy_u(index1)).^2));
        end
    end
    if s==0
        fft_field=fftshift(fft2(inField));
    else
        fft_field=fft2(inField);
    end
    h=H.*fft_field;
    for index1=1:size(inField,1)
        for index2=1:size(inField,2)
            % check for evanescent wave components
            constraint=sqrt(fx_u(index2).^2+fy_u(index1).^2);
            if constraint>(1/lambda);
                h(index1,index2)=0;
            end
        end
    end
    outField=ifft2(h);
end
```

A.2 MODE COUPLING ANALYSIS

Listing 2: Mode-Coupling Analysis

```
clear all; close all;

eps0 = 8.85e-12; % F/m, vacuum permittivity
mu0 = 4*pi*1e-7; % N/m^2, vacuum permeability
c = 2.998e8; % m/s, free space speed of light

v = 3909; % x-cut, y-propagating
lambda = [476e-9 532e-9 633e-9];
nAir = 1;
nLeaky = 2.28; % substrate ordinary index
nExtraordinary = 2.20; % substrate extraordinary index
nGuidedPE = 2.32; % waveguide extraordinary index, proton exchange
nGuidedDLW = 2.32; % waveguide extraordinary index, laser writing
nGuidedOrdinaryPE = 2.24; % waveguide ordinary index, proton exchange
nGuidedOrdinaryDLW = nLeaky; % waveguide ordinary index, laser writing
w = 2.5e-6; % waveguide depth
acousticFrequency = 300e6:1e6:700e6; % temporal acoustic frequencies
acousticWavevector = 2*pi/v.*acousticFrequency;
numGuidedModes = 4; % arbitrary
L = 50e-3; % dummy interaction length
K = zeros(length(acousticFrequency),numGuidedModes,length(lambda),2);
alpha = zeros(length(acousticFrequency),numGuidedModes,length(lambda),2);
betaLeakyArray = zeros(length(acousticFrequency),numGuidedModes,length(lambda)
    ,2);

numSamples = 1000;
depthVector = linspace(0,w,numSamples);
permittivityModulationSAW_PE = linspace(0,-0.3,1000).*10^-4; % comes from Rust
    /Strake
permittivityModulationSAW_DLW = linspace(0,-0.3,1000).*10^-4;

for lambdaIndex = 1:3 % iterate over wavelengths
    kLeaky = 2*pi*nLeaky/lambda(lambdaIndex);
    omega = 2*pi*c/lambda(lambdaIndex);
    for waveguideIndex = 1:2 % compute for both PE and laser-written
    waveguides
        if waveguideIndex == 1
            nGuided = nGuidedPE;
            nGuidedOrdinary = nGuidedOrdinaryPE;
            permittivityModulationSAW = permittivityModulationSAW_PE;
        else
            nGuided = nGuidedDLW;
            nGuidedOrdinary = nGuidedOrdinaryDLW;
            permittivityModulationSAW = permittivityModulationSAW_DLW;
        end
        kGuided = 2*pi*nGuided/lambda(lambdaIndex);
        for mIndex = 1:numGuidedModes
            nGuidedEffective = nGuided*sin(acos(mIndex*lambda(lambdaIndex)/(2*
    nGuided*w))); % waveguide effective extraordinary index
            betaGuided = 2*pi*nGuidedEffective/lambda(lambdaIndex);
            kyGuided = sqrt(kGuided^2-betaGuided^2);
            guidedangle = asind(kyGuided/kGuided);

            kappaAir = sqrt(betaGuided^2-(2*pi*nAir/lambda(lambdaIndex))^2); %
     Marcuse 1.2-15
            kappaSubstrate = sqrt(betaGuided^2-(2*pi*nExtraordinary/lambda(
    lambdaIndex))^2); % Marcuse 1.2-14
            wEffective = w+1/kappaAir+1/kappaSubstrate;
            betaLeaky = abs(betaGuided-acousticWavevector);
            betaLeakyArray(:,mIndex,lambdaIndex,waveguideIndex) = betaLeaky;
            qLeaky = sqrt(kLeaky^2-betaLeaky.^2);
            gamma = acosd(betaLeaky/kLeaky);
```

```
            guidedField = cos(kyGuided.*depthVector);
            guidedFieldNormalized = guidedField.*sqrt(omega*mu0/(betaGuided*
    wEffective)); % Marcuse 1.3-47

            for betaIndex = 1:length(betaLeaky)
                DeltaAir = sqrt((2*pi*nAir/lambda(lambdaIndex))^2 - betaLeaky(
    betaIndex)^2); % Marcuse 1.4-7
                sigmaGuide = sqrt((2*pi*nGuidedOrdinary/lambda(lambdaIndex))^2
     - betaLeaky(betaIndex)^2); % Marcuse 1.4-8
                rhoSubstrate = sqrt((2*pi*nLeaky/lambda(lambdaIndex))^2 -
    betaLeaky(betaIndex)^2);
                normalizationFactor = sqrt( ...
                    (4*omega*eps0*nGuidedOrdinary^4*nLeaky^2*nAir^4*
    rhoSubstrate^2*sigmaGuide^2/(pi*abs(betaLeaky(betaIndex)))) * conj(
    betaLeaky(betaIndex))/betaLeaky(betaIndex) * -1 * ...
                    (nGuidedOrdinary^4*rhoSubstrate^2*(nAir^2*sigmaGuide*cos(
    sigmaGuide*w)-nGuidedOrdinary^2*j*DeltaAir*sin(sigmaGuide*w))^2 + ...
                    nLeaky^4*sigmaGuide^2*(nAir^2*sigmaGuide*sin(sigmaGuide*w)
    -nGuidedOrdinary^2*j*DeltaAir*cos(sigmaGuide*w))^2)^-1 ...
                    ); % Marcuse 1.4-36
                leakyFieldH = cos(qLeaky(betaIndex).*depthVector);
                leakyFieldNormalizedH = leakyFieldH.*normalizationFactor;
                leakyFieldNormalized = betaLeaky(betaIndex)/(nLeaky^2*omega*
    eps0).*leakyFieldNormalizedH; % Marcuse 1.3-51
                F = guidedFieldNormalized.*(permittivityModulationSAW).*
    leakyFieldNormalized;
                K(betaIndex,mIndex,lambdaIndex,waveguideIndex) = omega*eps0/4*
    trapz(depthVector,F); % Matteo 11.1
                alpha(betaIndex,mIndex,lambdaIndex,waveguideIndex) = abs(K(
    betaIndex,mIndex,lambdaIndex,waveguideIndex))^2*pi*cotd(gamma(betaIndex))
    ; % Matteo 21
            end
        end
    end
end

eta = (1-exp(-2*alpha*L))*100;

%%% Plot results
acousticFrequency = acousticFrequency./10^6;

for mIndex = 3:3
    %%% Jointly plot results for laser-written and PE waveguides
    figure;
    plot(acousticFrequency,betaLeakyArray(:,mIndex,1,1),'b');
    hold on;
    plot(acousticFrequency,repmat(nGuidedOrdinaryPE*2*pi/lambda(1), [1 length(
    acousticFrequency)]),'b','LineWidth',2);
        hold on;
    plot(acousticFrequency,betaLeakyArray(:,mIndex,2,1),'g');
    hold on;
    plot(acousticFrequency,repmat(nGuidedOrdinaryPE*2*pi/lambda(2), [1 length(
    acousticFrequency)]),'g','LineWidth',2);
    hold on;
    plot(acousticFrequency,betaLeakyArray(:,mIndex,3,1),'r');
    hold on;
    plot(acousticFrequency,repmat(nGuidedOrdinaryPE*2*pi/lambda(3), [1 length(
    acousticFrequency)]),'r','LineWidth',2);
    xlabel('acoustic frequency (MHz)');
    ylabel('\beta_{leaky} (\mu m^{-1})');
    title(['\beta_{leaky} vs. acoustic frequency, proton exchanged guides, m =
     ' num2str(mIndex) ' mode'])

    figure;
    plot(acousticFrequency,betaLeakyArray(:,mIndex,1,2),'b');
    hold on;
    plot(acousticFrequency,repmat(nGuidedOrdinaryDLW*2*pi/lambda(1), [1 length
    (acousticFrequency)]),'b','LineWidth',2);
    hold on;
    plot(acousticFrequency,betaLeakyArray(:,mIndex,2,2),'g');
```

```
hold on;
plot(acousticFrequency,repmat(nGuidedOrdinaryDLW*2*pi/lambda(2), [1 length
(acousticFrequency)]),'g','LineWidth',2);
hold on;
plot(acousticFrequency,betaLeakyArray(:,mIndex,3,2),'r');
hold on;
plot(acousticFrequency,repmat(nGuidedOrdinaryDLW*2*pi/lambda(3), [1 length
(acousticFrequency)]),'r','LineWidth',2);
xlabel('acoustic frequency (MHz)');
ylabel('\beta_{leaky} (\mu m^{-1})');
title(['\beta_{leaky} vs. acoustic frequency, laser-written guides, m = '
num2str(mIndex) ' mode'])

%%% Plot results for PE waveguides only
figure;
plot(acousticFrequency,betaLeakyArray(:,mIndex,1,1),'b');
hold on;
plot(acousticFrequency,betaLeakyArray(:,mIndex,2,1),'g');
hold on;
plot(acousticFrequency,betaLeakyArray(:,mIndex,3,1),'r');
xlabel('acoustic frequency (MHz)');
ylabel('\beta_{leaky} (\mu m^{-1})');
title(['\beta_{leaky} vs. acoustic frequency, proton exchanged guides, m =
 ' num2str(mIndex) ' mode'])
figure;
plot(acousticFrequency,alpha(:,mIndex,1,1),'b');
hold on;
plot(acousticFrequency,alpha(:,mIndex,2,1),'g');
hold on;
plot(acousticFrequency,alpha(:,mIndex,3,1),'r');
xlabel('acoustic frequency (MHz)');
ylabel('radiative decay coefficient (\alpha)');
title(['\alpha_R vs. acoustic frequency, proton exchanged guides, m = '
num2str(mIndex) ' mode'])
figure;
plot(acousticFrequency,eta(:,mIndex,1,1),'b');
hold on;
plot(acousticFrequency,eta(:,mIndex,2,1),'g');
hold on;
plot(acousticFrequency,eta(:,mIndex,3,1),'r');
xlabel('acoustic frequency (MHz)');
ylabel('mode coupling efficiency (\eta, %)');
title(['\eta vs. acoustic frequency, proton exchanged guides, m = '
num2str(mIndex) ' mode'])

%%% Plot results for laser-written waveguides only
figure;
plot(acousticFrequency,betaLeakyArray(:,mIndex,1,2),'b');
hold on;
plot(acousticFrequency,betaLeakyArray(:,mIndex,2,2),'g');
hold on;
plot(acousticFrequency,betaLeakyArray(:,mIndex,3,2),'r');
xlabel('acoustic frequency (MHz)');
ylabel('\beta_{leaky} (\mu m^{-1})');
title(['\beta_{leaky} vs. acoustic frequency, laser-written guides, m = '
num2str(mIndex) ' mode'])
figure;
plot(acousticFrequency,alpha(:,mIndex,1,2),'b');
hold on;
plot(acousticFrequency,alpha(:,mIndex,2,2),'g');
hold on;
plot(acousticFrequency,alpha(:,mIndex,3,2),'r');
xlabel('acoustic frequency (MHz)');
ylabel('radiative decay coefficient (\alpha)');
title(['\alpha_R vs. acoustic frequency, PE + laser-written guides, m = '
num2str(mIndex) ' mode'])
figure;
plot(acousticFrequency,eta(:,mIndex,1,2),'b');
hold on;
plot(acousticFrequency,eta(:,mIndex,2,2),'g');
```

```
    hold on;
    plot(acousticFrequency,eta(:,mIndex,3,2),'r');
    xlabel('acoustic frequency (MHz)');
    ylabel('mode coupling efficiency (\eta, %)');
    title(['\eta vs. acoustic frequency, laser-written guides, m = ' num2str(
    mIndex) ' mode'])
end
```

A.3 KOGELNIK ANALYSIS

Listing 3: MATLAB Code for Transmission Kogelnik Analysis

```
close all; clear all; clc;

thetaDev = linspace(-10,10,1000000);
thetaDevRad = thetaDev .* pi / 180;
t = 50e-6;
centerLambda = 532e-9;
gratingPeriod = 10e-6;
gratingFrequency = 1 / gratingPeriod;
n_av = 2.28;
delta_n = 5e-4;
slantFactor = sqrt(1 - ((centerLambda * gratingFrequency) / (2 * n_av))^2);

eta1 = sin(pi * t * sqrt((delta_n / (centerLambda * slantFactor))^2 + (
    gratingFrequency .* thetaDevRad).^2)) .^2 ./ (1 + (centerLambda *
    gratingFrequency * slantFactor .* thetaDevRad / delta_n).^2);

thetaDev = linspace(-10,10,1000000);
thetaDevRad = thetaDev .* pi / 180;
t = 100e-6;
centerLambda = 532e-9;
gratingPeriod = 10e-6;
gratingFrequency = 1 / gratingPeriod;
n_av = 2.28;
delta_n = 5e-4;
slantFactor = sqrt(1 - ((centerLambda * gratingFrequency) / (2 * n_av))^2);

eta2 = sin(pi * t * sqrt((delta_n / (centerLambda * slantFactor))^2 + (
    gratingFrequency .* thetaDevRad).^2)) .^2 ./ (1 + (centerLambda *
    gratingFrequency * slantFactor .* thetaDevRad / delta_n).^2);

thetaDev = linspace(-10,10,1000000);
thetaDevRad = thetaDev .* pi / 180;
t = 250e-6;
centerLambda = 532e-9;
gratingPeriod = 10e-6;
gratingFrequency = 1 / gratingPeriod;
n_av = 2.28;
delta_n = 5e-4;
slantFactor = sqrt(1 - ((centerLambda * gratingFrequency) / (2 * n_av))^2);

eta3 = sin(pi * t * sqrt((delta_n / (centerLambda * slantFactor))^2 + (
    gratingFrequency .* thetaDevRad).^2)) .^2 ./ (1 + (centerLambda *
    gratingFrequency * slantFactor .* thetaDevRad / delta_n).^2);

plot(thetaDev,eta1*100,':');
hold on
plot(thetaDev,eta2*100,'-');
hold on
plot(thetaDev,eta3*100);
legend
ylabel('diffraction efficiency (%)');
xlabel('deviation from Bragg angle (degrees)');
title({'Kogelnik Coupled-Mode Diffracted Efficiency for Volume', ['Holographic
     Bragg Gratings in Transmission Geometry (t = 800 um, Lambda = 1 um)']});
```

Listing 4: MATLAB Code for Reflection Kogelnik Analysis

```
close all; clear all; clc;

slantAngle = 0 * pi / 180;
```

```
thetaDev = linspace(-15,15,1000);
thetaDevRad = thetaDev .* pi / 180;
thetaMCenter = 0 * pi / 180;
lambdaDev = 0e-9;
% t = 800e-6;
centerLambda = 532e-9;
gratingPeriod = 5e-6;
gratingFrequency = 1 / gratingPeriod;
n_av = 2.28;
delta_n = 10e-4;
deltaNArray = logspace(-4,-3,500);
tArray = linspace(10e-6,1000e-6,990);
etaArray = zeros(length(deltaNArray),length(tArray),length(thetaDev));
etaMaxArray = zeros(length(deltaNArray),length(tArray));
etaFWHMArray = zeros(length(deltaNArray),length(tArray));

slantFactor = sqrt(-cos(slantAngle - thetaMCenter) .* cos(slantAngle +
    thetaMCenter));

for deltaNIndex = 1:length(deltaNArray)
    disp(['Computing deltaN ' num2str(deltaNIndex) ' of ' num2str(length(
    deltaNArray)) '...']);
    for tIndex = 1:length(tArray)
        S = (j * pi * tArray(tIndex) * deltaNArray(deltaNIndex)) / (
    centerLambda .* slantFactor);
        zeta = (pi * gratingFrequency * tArray(tIndex) * cos(thetaMCenter)) /
    (cos(slantAngle - thetaMCenter) - (gratingFrequency * centerLambda / n_av
    ) * cos(slantAngle)) .* (thetaDevRad .* tan(thetaMCenter) + thetaDevRad
    .^2 / 2 + lambdaDev / centerLambda);
            etaArray(deltaNIndex,tIndex,:) = (sin(sqrt(zeta.^2 - S.^2)))
    .^2 ./ (zeta.^2 ./ S.^2 - (cos(sqrt(zeta.^2 - S.^2))).^2);
        etaMaxArray(deltaNIndex,tIndex) = max(squeeze(etaArray(deltaNIndex,
    tIndex,:)));
        etaFWHMArray(deltaNIndex,tIndex) = fwhm(thetaDev,squeeze(etaArray(
    deltaNIndex,tIndex,:))');
    end
end

figure; imagesc(tArray,deltaNArray,etaMaxArray); colorbar; colormap jet;
    ylabel('\Delta n (unitless)'); xlabel('thickness (m)'); title('Maximum
    diffraction efficiency vs. index perturbation vs. hologram thickness');
figure; imagesc(tArray,deltaNArray,etaFWHMArray); colorbar; colormap jet;
    ylabel('\Delta n (unitless)'); xlabel('thickness (m)'); title('FWHM of
    angular acceptance vs. index perturbation vs. hologram thickness');
figure; imagesc(tArray,deltaNArray,etaMaxArray.*etaFWHMArray); colorbar;
    colormap jet; ylabel('\Delta n (unitless)'); xlabel('thickness (m)');
    title('Eta-FWHM vs. index perturbation vs. hologram thickness');
figure; plot(tArray,etaFWHMArray(1,:)); ylabel('FWHM of angular acceptance (
    degrees)'); xlabel('thickness (m)'); title('FWHM of angular acceptance vs
    . hologram thickness, \Delta n = 10^-^4');
figure; plot(tArray,etaFWHMArray(500,:)); ylabel('FWHM of angular acceptance (
    degrees)'); xlabel('thickness (m)'); title('FWHM of angular acceptance vs
    . hologram thickness, \Delta n = 10^-^3');
layerArray = tArray ./ 1e-6;
figure; plot(layerArray,etaMaxArray(1,:)); ylabel('diffraction efficiency');
    xlabel('number of layers'); title('Diffraction efficiency vs. number of
    layers, \Delta n = 10^-^4');
figure; plot(layerArray,etaMaxArray(250,:)); ylabel('diffraction efficiency');
     xlabel('number of layers'); title('Diffraction efficiency vs. number of
    layers, \Delta n = 5x10^-^4');
figure; plot(layerArray,etaMaxArray(500,:)); ylabel('diffraction efficiency');
     xlabel('number of layers'); title('Diffraction efficiency vs. number of
    layers, \Delta n = 10^-^3');
layerArray = tArray ./ 5e-6;
figure; plot(layerArray,etaMaxArray(1,:)); ylabel('diffraction efficiency');
    xlabel('number of layers'); title('Diffraction efficiency vs. number of
    layers, \Delta n = 10^-^4');
figure; plot(layerArray,etaMaxArray(250,:)); ylabel('diffraction efficiency');
     xlabel('number of layers'); title('Diffraction efficiency vs. number of
    layers, \Delta n = 5x10^-^4');
```

```
figure; plot(layerArray,etaMaxArray(500,:)); ylabel('diffraction efficiency');
     xlabel('number of layers'); title('Diffraction efficiency vs. number of
    layers, \Delta n = 10^-^3');

imagesc(deltaNArray,tArray,etaArray);

plot(thetaDev,eta*100);
ylabel('diffraction efficiency (%)');
xlabel('deviation from Bragg angle (degrees)');
title({'Kogelnik Coupled-Mode Diffracted Efficiency for Volume', ['Holographic
     Bragg Gratings in Reflection Geometry (t = 800 um, Lambda = 1 um)']});
hold on;
```

A.4 WIGNER SPACE ANALYSIS

Listing 5: MATLAB Code for Space-Bandwidth Product Analysis

```
% Space-frequency analysis of hologram diffraction
close all;
clear all;

% Define physical and mathematical constants
eps_0 = 8.85e-12;           % Permittivity of free space
c_0 = 299792458;            % Speed of light in vacuum (m/s)
e = 2.718281828;            % Natural logarithmic base

% Define beam parameters
lambda = 532e-9;            % operating wavelength (m)
k = (2*pi)/lambda;      % wavevector magnitude (1/m)

% Define grid
Nx = 6000;                  % number of pixels defined in x-dimension

% Create spatial domain
Tx_u1 = 50e-3;
dx_u1 = Tx_u1/Nx;
vx_u1 = -Tx_u1/2:dx_u1:(Tx_u1/2-dx_u1);
% Create spatial frequency domain
fx_v_u1 = (-1/Tx_u1 * Nx/2):(1/Tx_u1):(1/Tx_u1 * Nx/2 - 1/Tx_u1);
theta_v_u1 = asind(lambda.*fx_v_u1);

s = 0; % fftshift initialization parameter

% Set up WDF distribution
wignerHologramPlane = zeros(Nx);
vx_u1 = -Tx_u1/2:dx_u1:(Tx_u1/2-dx_u1);
numHogelsPerUnit = 1;
numUnits = 1;
hogelLength = 5e-3;
hogelGap = 500e-6;
unitGap = 5e-3;
unitLength = numHogelsPerUnit.*hogelLength+(numHogelsPerUnit-1).*hogelGap;
unitCenters = [];
hogelCenters = [];
if mod(numUnits,2) == 0
    unitNumbers = [-numUnits/2:-1 1:numUnits/2];
else
    unitNumbers = [ceil(-numUnits/2):-1 0 1:floor(numUnits/2)];
end
if mod(numHogelsPerUnit,2) == 0
    hogelNumbers = [-numHogelsPerUnit/2:-1 1:numHogelsPerUnit/2];
else
    hogelNumbers = [ceil(-numHogelsPerUnit/2):-1 0 1:floor(numHogelsPerUnit/2)
    ];
end
for unitIndex = 1:numUnits
    if mod(numUnits,2) == 0 % even case - 1,3,5,...
        unitCenter = (abs(unitNumbers(unitIndex)*2)-1).*sign(((unitNumbers(
    unitIndex)))).*(unitGap/2+unitLength/2);
    else % odd case - 0,2,4,...
        unitCenter = (abs(unitNumbers(unitIndex)*2)).*sign(((unitNumbers(
    unitIndex)))).*(unitGap/2+unitLength/2);
    end
    unitCenters = [unitCenters unitCenter];
    for hogelIndex = 1:numHogelsPerUnit
        if mod(numHogelsPerUnit,2) == 0
            hogelCenter = unitCenter+((abs(hogelNumbers(hogelIndex)*2)-1).*
    sign(((hogelNumbers(hogelIndex)))).*(hogelGap/2+hogelLength/2));
        else
```

```
            hogelCenter = unitCenter+((abs(hogelNumbers(hogelIndex)*2)).*sign
    (((hogelNumbers(hogelIndex)))).*(hogelGap/2+hogelLength/2));
        end
        hogelCenters = [hogelCenters hogelCenter];
    end
end
hogelDistribution = zeros(1,Nx);
for hogelIndex = 1:length(hogelCenters)
    hogelDistribution = hogelDistribution + rectangularPulse(hogelCenters(
    hogelIndex)-hogelLength/2,hogelCenters(hogelIndex)+hogelLength/2,vx_u1);
end

cutoffFrequency = abs(sind(1)/lambda);
dummy = abs(cutoffFrequency-fx_v_u1);
minDummy = min(dummy);
cutoffFrequencyIndex = find(dummy==minDummy);
clear dummy; clear minDummy;
cutoffIndexLength = abs(cutoffFrequencyIndex-ceil(Nx/2));
hogelWDFdummy = repmat(hogelDistribution,[cutoffIndexLength*2,1]);
hogelWDF = padarray(hogelWDFdummy,[Nx/2-floor(size(hogelWDFdummy,1)/2),0]);
hogelWDF = hogelWDF';

% Plot Wigner distribution of initial SBP
figure(1);
imagesc(vx_u1,theta_v_u1,abs(hogelWDF'));
xlabel('x (m)');
%ylabel ('u (m^-1)');
ylabel ('diffraction angle (degrees)')
title('Wigner distribution of SBP');

z = 0;

for i = 1:1000

    % Propagate modulated field via Fresnel diffraction and find Fourier
    % transform
    z_L1 = 1e-4;

    % Propagate modulated field via Fresnel diffraction in Wigner space
    hogelWDF = wigner_x_shear(hogelWDF',z,lambda,vx_u1,fx_v_u1);

    % Plot Wigner distribution after propagation
    figure(1);
    imagesc(vx_u1,theta_v_u1,abs(hogelWDF));
    xlabel('x (m)');
    ylabel ('diffraction angle (degrees)')
    title('Wigner distrbution of SBP');

    hogelWDF = hogelWDF';

    z = z + z_L1;

    filename = ['./data/singleWDF-' num2str(i) '.mat'];
    save(filename,'hogelWDF');

end
```

A.5 TRANSDUCER DESIGN AND GENERATION

Listing 6: MATLAB Code for Generation of Transducer Design Files

```
close all; clear all;

inverse = 1;

period = 15e-6;
width = 100e-6;
N = 50;
gapDistance = 1e-6; % objective resolution

x = linspace(-width*5,width*5,5000);
dx = x(2)-x(1);
periodPixels = ceil(period/dx);
topMargin = ceil(100e-6/dx);

pads = rectangularPulse(-width*3/2,-width/6,x)+rectangularPulse(width/6,width
    *3/2,x);
padHeight = ceil((width*3/2-width/6)/dx);
padArray = repmat(pads,[padHeight 1]);

figure; imagesc(padArray);

fingerLeft = rectangularPulse(-width/2,width/4,x) + rectangularPulse(width
    *3/8,width/2,x);
fingerRight = rectangularPulse(-width/2,-width*3/8,x) + rectangularPulse(-
    width/4,width/2,x);
fingerGap = rectangularPulse(-width/2,-width*3/8,x) + rectangularPulse(width
    *3/8,width/2,x);

fingerPair = [repmat(fingerGap,[floor(periodPixels/4) 1]); ...
              repmat(fingerLeft,[floor(periodPixels/4) 1]); ...
              repmat(fingerGap,[floor(periodPixels/4) 1]); ...
              repmat(fingerRight,[floor(periodPixels/4) 1])];

figure; imagesc(fingerPair);
fingers = repmat(fingerPair,[N 1]);
figure; imagesc(fingers);

transducer = [zeros(topMargin,length(x)); ...
              padArray; ...
              repmat(fingerGap,[floor(ceil(width/dx)/3) 1]); ...
              fingers; ...
              zeros(topMargin,length(x))]; ...

gapOverlay = ones(size(transducer));

for i = 1:size(gapOverlay,1)
    if mod(i,ceil(gapDistance./dx)) == 0
        gapOverlay(i,:) = zeros(1,size(transducer,2));
    end
end

figure; imagesc(gapOverlay)

if inverse == 0
    for i = 1:size(transducer,1)
        for j = 1:size(transducer,2)
            if (transducer(i,j) == 1 && gapOverlay(i,j) == 0)
                transducer(i,j) = 0;
            end
        end
    end
else
    transducer = imcomplement(transducer);
```

```
    for i = 1:size(transducer,1)
        for j = 1:size(transducer,2)
            if (transducer(i,j) == 1 && gapOverlay(i,j) == 0)
                transducer(i,j) = 0;
            end
        end
    end
end

figure; imagesc(transducer);
imwrite(transducer,'transducer15-inverse-largeMargin-1um.png');

format long;
dpi = 0.0254 / dx
```

BIBLIOGRAPHY

[1] J. Rolland and H. Hua, "Head-Mounted Display Systems," *Encyclopedia of Optical Engineering*, Taylor & Francis, 2005.

[2] D. Lanman and D. Luebke, "Near-eye light field displays," *ACM Transactions on Graphics (TOG)*, vol. 32, no. 6, Nov. 2013.

[3] H. Hua and B. Javidi, "A 3D integral imaging optical see-through head-mounted display," *Optics Express*, vol. 22, no. 11, pp. 13484-13491, Jun. 2014.

[4] F.-C. Huang, K. Chen, and G. Wetzstein, "The light field stereoscope: immersive computer graphics via factored near-eye light field displays with focus cues," *ACM Transactions on Graphics (TOG)*, vol. 34, no. 4, Jul. 2015.

[5] ZSpace. Retrieved from: http://www.zspace.com.

[6] "Accommodation in the Eye and Camera," retrieved from http://hyperphysics.phy-astr.gsu.edu/hbase/geoopt/camacc.html.

[7] S. Reichelt, R. Haussler, G. Fatterer, and N. Leister, "Depth cues in human visual perception and their realization in 3-D displays," *Proc. SPIE*, 7690, 2010.

[8] M. Lambooij, W. IJsselsteijn, M. Fortuin, and I. Heynderickx, "Visual discomfort and visual fatigue of stereoscopic displays: a review," *Journal of Imaging Science and Technology*, vol. 53, 2009.

[9] J. L. Olson, D. M. Krum, E. A. Suma, and M. Bolas, "A design for a smartphone-based head mounted display," *Proc. 2011 IEEE Virtual Reality (VR)*, pp. 233-234, 2011.

[10] Oculus. Retrieved from: http://www.oculus.com.

[11] E. H. Adelson and J. R. Bergen, "The plenoptic function and the elements of early vision," *Computational Models of Visual Processing*, Chapter 1, Eds. Michael Landy and J. Anthony Movshon. The MIT Press, Cambridge, MA. 1991.

[12] T. Okoshi, *Three-Dimensional Imaging Techniques*, New York: Academic Press, 1976.

[13] Y. Takaki, K. Tanaka, and J. Nakamura, "Super multi-view display with a lower resolution flat-panel display," *Optics Express*, vol. 19, no. 5, pp. 4129-4139, Feb. 2011.

[14] A. Maimone, G. Wetzstein, M. Hirsch, D. Lanman, R. Raskar, and H. Fuchs, "Focus 3D: Compressive accommodation display," *ACM Transactions on Graphics (TOG)*, vol. 32, no. 5, Sep. 2013.

[15] S. A. Benton and V. M. Bove, Jr., *Holographic Imaging*. Hoboken, NJ: Wiley, 2008.

[16] M. Lucente, "Holographic bandwidth compression using spatial subsampling," *Optical Engineering*, vol. 35, no. 6 (1996).

[17] J. Barabas and V. M. Bove, Jr., "Visual Perception and Holographic Displays," *J. Phys.: Conf. Ser.*, vol. 415, no. 1, Feb. 2013.

[18] D. E. Smalley, *Holovideo on a Stick: Integrated Optics for Holographic Video Displays*, Ph. D. Thesis, Massachusetts Institute of Technology, 2013.

[19] D. E. Smalley, Q. Y. J. Smithwick, V. M. Bove, J. Barabas, and S. Jolly,"Anisotropic leaky-mode modulator for holographic video displays," *Nature*, vol. 498, no. 7454, pp. 313-317, Jun. 2013.

[20] P. St. Hilaire, *Scalable Optical Architectures for Electronic Holography*, Ph. D. Thesis, Massachusetts Institute of Technology, 1994.

[21] P. S. Hilaire, S. A. Benton, and M. Lucente, "Synthetic aperture holography: a novel approach to three-dimensional displays," *Journal of the Optical Society of America A*, vol. 9, no. 11, pp. 1969-1977, 1992.

[22] J. Hong, Y. Kim, S. Hong, C. Shin, and H. Kang, "Gaze contingent hologram synthesis for holographic head-mounted display," *Proceedings of SPIE Practical Holography XXX: Materials and Applications*, vol. 9771, pp. 97710K-97710K-?6, Mar. 2016.

[23] E. Moon, M. Kim, J. Roh, H. Kim, and J. Hahn, "Holographic head-mounted display with RGB light emitting diode light source," *Optics Express*, vol. 22, no. 6, pp. 6526-6534, Mar. 2014.

[24] H.-J. Yeom, H.-J. Kim, S.-B. Kim, H. Zhang, B. Li, Y.-M. Ji, S.-H. Kim, and J.-H. Park, "3D holographic head mounted display using holographic optical elements with astigmatism aberration compensation," *Optics Express*, vol. 23, no. 25, pp. 32025-?32034, Dec. 2015.

[25] A. Henrie, D. E. Smalley, S. Gneiting, and S. McLaughlin, "Backside emission leaky-mode modulators," *Optics Express*, vol. 25, no. 17, pp. 20622-20627, Aug. 2017.

[26] L. Onural, F. Yaras, and H. Kang, "Digital Holographic Three-Dimensional Video Displays," *Proceedings of the IEEE*, vol. 99, no. 4, 2011.

[27] D. A. Atchison and G. Smith, *Optics of the Human Eye*, Elsevier Health Sciences, New York, 2000.

[28] A. N. Putilin, V. N. Morozov, Q. Huang, and H. J. Caulfield, "Waveguide holograms with white light illumination," *Optical Engineering*, vol. 30, no. 10, pp. 1615-1619, Oct. 1991.

[29] H. J. Caulfield, Q. Huang, A. Putilin, V. Morozov, "Multimode waveguide holograms capable of using non-coherent light," Mar. 1994.

[30] M. Li, P. Modh, S. Kristjansson, A. Larsson, C. Silfvenius, and G. Landgren, "Demonstration of computer-generated waveguide hologram on InGaAsP-InP waveguide for 1550-nm optical wavelength," *IEEE Photonics Technology Letters*, vol. 9, no. 7, pp. 958-960, 1997.

[31] H. Mukawa, K. Akutsu, I. Matsumura, S. Nakano, T. Yoshida, M. Kuwahara, and K. Aiki, "A full-color eyewear display using planar waveguides with reflection volume holograms," *Journal of the Society for Information Display*, vol. 17, no. 3, pp. 185-193, Mar. 2009.

[32] S. Jolly, N. Savidis, N. Datta, V. M. Bove, Jr., and D. E. Smalley, "Progress in off-plane computer-generated waveguide holography for near-to-eye 3D display," Proc. SPIE Practical Holography XXX: Materials and Applications, 9771, 2016.

[33] R. W. Gerchberg and W. O. Saxton, "A Practical Algorithm for the Determination of Phase from Image and Diffraction Plane Pictures," *Optik*, vol. 35, no. 2, 1972.

[34] J. W. Goodman, *Introduction to Fourier Optics*, 3rd ed., Roberts & Company, Woodbury, NY. 2005.

[35] S. Jolly, N. Savidis, B. Datta, D. Smalley, and V. M. Bove, Jr., "Near-to-eye electroholography via guided-wave acousto-optics for augmented reality," Proc. SPIE Practical Holography XXXI: Materials and Applications, 10127, 2017.

[36] H.-E. Kim, N. Kim, H. Song, H.-S. Lee, and J.-H. Park, "Three-dimensional holographic display using active shutter for head mounted display application," *Proceedings of IS&T/SPIE Stereoscopic Displays and Applications XXII*, vol. 7863, pp. 78631Y-78631Y-8, Feb. 2011.

[37] J. Backlund, J. Bengtsson, and A. Larsson, "Waveguide hologram for outcoupling and simultaneous focusing into multiple arbitrary positions," *IEEE Photonics Technology Letters*, vol. 10, no. 9, pp. 1286-1288, 1998.

[38] D. V. Petrov and J. Ctyroky, "Acousto-optic conversion of a guided mode into a leaky wave in a Ti:LiNbO3 waveguide," *Pis'ma v Zhurnal Tekhnicheskoi Fiziki*, vol. 9, pp. 1120-1124, Sep. 1983.

[39] A. M. Matteo, C. S. Tsai, and N. Do, "Collinear guided wave to leaky wave acoustooptic interactions in proton-exchanged $LiNbO_3$ waveguides," *IEEE Trans. Ultrason., Ferroelect., Freq. Contr.*, vol. 47, no. 1, pp. 16-28, 2000.

[40] A. M. Matteo, N. Do, and C. S. Tsai, "Collinear acousto-optical interactions in proton-exchanged lithium niobate waveguides," *Proc. SPIE Ultrasonics and Ferroelectrics*, vol. 2695, pp. 325-334, 1996.

[41] C. S. Tsai, *Guided-Wave Acousto-Optics: Interactions Devices and Applications.* Springer-Verlag, 1990.

[42] W. Akemann, J.-F. Lager, C. Ventalon, B. Mathieu, S. Dieudonn, and L. Bourdieu, "Fast spatial beam shaping by acousto-optic diffraction for 3D non-linear microscopy," *Optics Express*, vol. 23, no. 22, pp. 28191-28205, Nov. 2015.

[43] P. Bechtold, R. Hohenstein, and M. Schmidt, "Beam shaping and high-speed, cylinder-lens-free beam guiding using acousto-optical deflectors without additional compensation optics," *Optics Express*, 21(12), 14627-14635, 2013.

[44] H. Kogelnik, "Coupled wave theory for thick hologram gratings," *The Bell System Technical Journal*, 1969.

[45] J. Hukriede, D. Runde, and D. Kip, "Fabrication and application of holographic Bragg gratings in lithium niobate channel waveguides," *J. Phys. D: Appl. Phys.*, vol. 36, no. 3, pp. R1-R16, Feb. 2003.

[46] B. T. Schowengerdt and E. J. Seibel, "Stereoscopic retinal scanning laser display with integrated focus cues for ocular accommodation," *Proceedings of SPIE/IS&T Stereoscopic Displays and Virtual Reality Systems XI*, vol. 5291, 2004.

[47] American National Standards Institute, *American National Standard for the Safe Use of Lasers, Standard Z136.1-2014*, 2014.

[48] D. E. Holmgren and W. Robinett, "Scanned Laser Displays for Virtual Reality: A Feasibility Study," *Presence: Teleoperators and Virtual Environments*, vol. 2, no. 3, pp. 171-184, Jan. 1993.

[49] R. R. Hainich and O. Bimber, *Displays: Fundamentals and Applications*. CRC Press, 2014.

[50] N. Savidis, S. Jolly, B. Datta, M. Moebius, T. Karydis, E. Mazur, N. Gershenfeld, and V. M. Bove, Jr., "Progress in fabrication of waveguide spatial light modulators via femtosecond laser micromachining," Proc. SPIE Advanced Fabrication Technologies for Micro/Nano Optics and Photonics X, 10115, 2017.

[51] S. Jolly, N. Savidis, B. Datta, T. Karydis, W. Langford, N. Gershenfeld, and V. M. Bove, Jr., "Progress in fabrication of anisotropic Bragg gratings in lithium niobate via femtosecond laser micromachining," Proc. SPIE Advanced Fabrication Technologies for Micro/Nano Optics and Photonics XI, 10554, 2018.

[52] N. Savidis, S. Jolly, B. Datta, T. Karydis, and V. M. Bove, Jr., "Fabrication of waveguide spatial light modulators via femtosecond laser micromachining," Proc. SPIE Advanced Fabrication Technologies for Micro/Nano Optics and Photonics IX, 9759, 2016.

[53] S. Jolly, B. Datta, V. Parthiban, D. Smalley, and V. M. Bove, Jr., "Experimental characterization of leaky-mode spatial light modulators fabricated by direct laser writing," *Proc. SPIE Practical Holography XXXIII: Displays, Materials, and Applications*, 10944, 2019

[54] R. R. Gattass and E. Mazur, "Femtosecond laser micromachining in transparent materials," *Nature Photonics*, vol. 2, no. 4, pp. 219-225, Apr. 2008.

[55] J. Burghoff, S. Nolte, and A. Tannermann, "Origins of waveguiding in femtosecond laser-structured LiNbO3," *Applied Physics A*, vol. 89, no. 1, pp. 127-132, 2007.

[56] D. Paipulas, V. Mizeikis, V. Purlys, A. Cerkauskaite, and S. Juodkazis, "Volumetric integration of photorefractive micromodifications in lithium niobate with femtosecond laser pulses," *Proc. SPIE 9374*,93740B-13, 2015.

[57] H. Hu, R. Ricken, W. Sohler, and R. B. Wehrspohn, "Lithium Niobate Ridge Waveguides Fabricated by Wet Etching," *IEEE Photonics Technology Letters*, 19(6), 417-419, 2007.

[58] M. Tamura and S. Yoshikado, "Etching characteristics of $LiNbO_3$ crystal by fluorine gas plasma reactive ion etching," *Surface and Coatings Technology*, 169, 203-207, 2003.

[59] E. H. Turner, R. C. Alferness, and R. V. Schmidt, "Characteristics of Ti-diffused lithium niobate optical directional couplers," *Applied Optics*, 18(23), 4012-4016, 1979.

[60] C. E. Rice and J. L. Jackel, "Structural changes with composition and temperature in rhombohedral $Li_{1-x}H_xNbO_3$," *Materials Research Bulletin*, 19(5), 591-597, 1984.

[61] V. Hinkov, "Proton exchanged waveguides for surface acoustic waves on $LiNbO_3$," *Journal of Applied Physics*, 62(9), 3573-3578, 1998.

[62] G. Noviello, M. N. Armenise, and V. M. N Passaro, "Lithium niobate guided-wave beam former for steering phased-array antennas," *Applied Optics*, 33(26), 6194-6209, 1994.

[63] H. T. Bookey, R. R. Thomson, N. D. Psaila, A. K. Kar, N. Chiodo, R. Osellame, and G. Cerullo, "Femtosecond Laser Inscription of Low Insertion Loss Waveguides in Z-Cut Lithium Niobate," *IEEE Photonics Technology Letters*, 19(12), 892-894, 2007.

[64] J. Thomas, M. Heinrich, P. Zeil, V. Hilbert, K. Rademaker, R. Riedel, S. Ringleb, C. Dubs, J. P. Ruske, S. Nolte, and A. Tannermann, "Laser direct writing: Enabling monolithic and hybrid integrated solutions on the lithium niobate platform," *Physica Status Solidi (a)*, 208(2), 276-283, 2011.

[65] M. Beresna and P. G. Kazansky, "Polarization diffraction grating produced by femtosecond laser nanostructuring in glass," *Optics Letters*, 35(10), 1662-1664, 2010.

[66] C. Denz, J. Herrmann, J. Imbrock, S. Kroesen, W. and Horn, "Electro-optical tunable waveguide Bragg gratings in lithium niobate induced by femtosecond laser writing," *Optics Express*, 20(24), 26922-26928, 2012.

[67] C. Dietrich, C. Denz, J. Imbrock, S. Kroesen, and W. Horn, "Femtosecond Laser-Induced Volume Gratings in Lithium Niobate for Noncollinear Second-Harmonic Generation," *Proceedings of CLEO 2014*, 2014.

[68] D. Paipulas, V. Kudriaov, M. Malinauskas, V. Smilgeviaius, and V. Sirutkaitis, "Diffraction grating fabrication in lithium niobate and KDP crystals with femtosecond laser pulses," *Applied Physics A*, vol. 104, no. 3, pp. 769–773, 2011.

[69] T. Gertus, P. Kazdailas, R. Rimeika, D. Ciplys, and V. Smilgevicius, "Surface acoustic wave transducers fabricated by femtosecond laser ablation," *Electronics Letters*, vol. 46, no. 17, pp. 1175-1176, Aug. 2010.

[70] J. Burghoff, H. Hartung, S. Nolte, and A. Tannermann, "Structural properties of femtosecond laser-induced modifications in $LiNbO_3$," *Applied Physics A*, vol. 86, no. 2, pp. 165-170, 2007.

[71] D. Grando, J. Yu, D. Ballarini, and P. Galinetto, "Femtosecond Laser Writing of Surface Microstructures in Lithium Niobate," *Nonlinear Guided Waves and Their Applications (2005)*, paper WD33, p. WD33, Sep. 2005.

[72] U. Rust and E. Strake, "Acoustooptical coupling of guided to substrate modes in planar proton-exchanged $LiNbO_3$-waveguides," *Integrated Photonics Research*, 1992.

[73] I. V. Ciapurin, L. B. Glebov, and V. I. Smirnov, "Modeling of Gaussian beam diffraction on volume Bragg gratings in PTR glass," *Proceedings of SPIE Practical Holography XIX: Materials and Applications*, vol. 5742, pp. 183-?194, Apr. 2005.

[74] G. Barbastathis and D. Psaltis, "Volume holographic multiplexing methods," in *Holographic Data Storage*, Eds: H. Coufal, D. Psaltis, and G. Sincerbox. Springer, New York, 2000.

[75] I. V. Ciapurin, D. R. Drachenberg, V. I. Smirnov, G. B. Venus, and L. B. Glebov, "Modeling of phase volume diffractive gratings, part 2: reflecting sinusoidal uniform gratings, Bragg mirrors," *Optical Engineering*, vol. 51, no. 5, May 2012.

[76] J. Han, J. Liu, X. Yao, and Y. Wang, "Portable waveguide display system with a large field of view by integrating freeform elements and volume holograms," *Optics Express*, vol. 23, no. 3, Feb. 2015.

[77] S. Jolly, N. Savidis, B. Datta, D. E. Smalley, and V. M. Bove, Jr., "Progress in transparent, flat-panel holographic displays enabled by guided-wave acousto-optics," *Proc. SPIE Practical Holography XXXII: Displays, Materials, and Applications*, 10558, 2018.

[78] S. Jolly, D. E. Smalley, J. Barabas, and V. M. Bove, Jr., "Computational architecture for full-color holographic displays based on anisotropic leaky-mode modulators," *Proc. SPIE Practical Holography XXVIII*, 9006, 2014.

[79] B. Datta, N. Savidis, M. Moebius, S. Jolly, E. Mazur, and V. M. Bove, Jr., "Direct-laser metal writing of surface acoustic wave transducers for integrated-optic spatial light modulators in lithium niobate," *Proc. SPIE Advanced Fabrication Technologies for Micro/Nano Optics and Photonics X*, 10115, 2017.

[80] G. A. Goetz, Y. Mandel, R. Manivanh, D. V. Palanker, and T. Cizmar, "Holographic display system for restoration of sight to the blind," *Journal of Neural Engineering*, vol. 10, no. 5, p. 056021, Oct. 2013.

[81] G. Li, D. Lee, Y. Jeong, and B. Lee, "Fourier holographic display for augmented reality using holographic optical element," *Proceedings of SPIE Advances in Display Technologies VI*, vol. 9770, pp. 97700D-97700D-6, Mar. 2016.

[82] Y. Takaki and N. Okada, "Hologram generation by horizontal scanning of a high-speed spatial light modulator," *Applied Optics*, vol. 48, no. 17, pp. 3255-3260, Jun. 2009.

[83] Y. Takaki and M. Yokouchi, "Accommodation measurements of horizontally scanning holographic display," *Optics Express*, vol. 20, no. 4, pp. 3918-3931, Feb. 2012.

[84] Y. Takaki, Y. Matsumoto, and T. Nakajima, "Color image generation for screen-scanning holographic display," *Optics Express*, vol. 23, no. 21, pp. 26986-26998, Oct. 2015.

[85] T. Levola, "Novel Diffractive Optical Components for Near to Eye Displays," *SID Symposium Digest of Technical Papers*, vol. 37, no. 1, pp. 64-67, Jun. 2006.

[86] R. Haussler, A. Schwerdtner, and N. Leister, "Large holographic displays as an alternative to stereoscopic displays," *Proceedings of SPIE Stereoscopic Displays and Applications XIX*, vol. 6803, 2008.

[87] Y. Takaki and K. Fujii, "Viewing-zone scanning holographic display using a MEMS spatial light modulator," *Optics Express*, vol. 22, no. 20, pp. 24713-24721, Oct. 2014.

[88] O. Bryngdahl and A. Lohmann, "Single-Sideband Holography," *Journal of the Optical Society America*, vol. 58, no. 5, p. 620, 1968.

[89] R. E. Hopkins and M. J. Buzawa, "Optics for Laser Scanning," *Optical Engineering*, vol. 15, no. 2, p. 150290, Apr. 1976.

[90] M. Dubov, S. Boscolo, and D. J. Webb, "Microstructured waveguides in z-cut $LiNbO_3$ by high-repetition rate direct femtosecond laser inscription," *Optical Materials Express*, vol. 4, no. 8, pp. 1708-1716, Aug. 2014.

[91] R. He, Q. An, Y. Jia, G. R. Castillo-Vega, J. R. V. de Aldana, and F. Chen, "Femtosecond laser micromachining of lithium niobate depressed cladding waveguides," *Optical Materials Express*, vol. 3, no. 9, pp. 1378-1384, Sep. 2013.

[92] V. Mizeikis, V. Purlys, D. Paipulas, and R. Buividas, "Direct Laser Writing: Versatile Tool for Microfabrication of Lithium Niobate," *Journal of Laser Micro/Nanomachining*, 2012.

[93] N. Savidis, S. Jolly, B. Datta, T. Karydis, and V. Michael Bove, Jr., "Fabrication of waveguide spatial light modulators via femtosecond laser micromachining," *Proc. SPIE Advanced Fabrication Technologies for Micro/Nano Optics and Photonics IX*, 9759, 2016.

[94] Q. Y. J. Smithwick, J. Barabas, D. E. Smalley, and V. M. Bove, Jr., "Interactive Holographic Stereograms with Accommodation Cues," *Proc. SPIE Practical Holography XXIV*, v. 7619, 2010.

[95] J. Barabas, S. Jolly, D. E. Smalley, and V. M. Bove, Jr., "Diffraction Specific Coherent Panoramagrams of Real Scenes," *Proc. SPIE Practical Holography XXV: Materials and Applications*, v. 7957, 2011.

[96] D. Marcuse, "Coupled-mode theory for anisotropic optical waveguides," *The Bell System Technical Journal*, vol. 54, no. 6, pp. 985-995, 1975.

[97] R. Magnusson and T. K. Gaylord, "Analysis of multiwave diffraction of thick gratings," *Journal of the Optical Society of America A*, vol. 67, no. 9, pp. 1165-1170, Sep. 1977.

[98] E. N. Glytsis and T. K. Gaylord, "Rigorous three-dimensional coupled-wave diffraction analysis of single and cascaded anisotropic gratings," *Journal of the Optical Society of America A*, vol. 4, no. 11, pp. 2061-2080, Nov. 1987.

[99] G. P. Nordin, R. V. Johnson, and A. R. Tanguay, Jr, "Diffraction properties of stratified volume holographic optical elements," *Journal of the Optical Society of America A*, vol, 9, no. 12, pp. 2206, 1992.

[100] W. Cai, T. Reber, and R. Piestun, "Computer generated volume holograms fabricated by femtosecond laser micromachining," *Optics Letters*, vol. 31, no. 12, 2006.

[101] G. Ye, S. Jolly, V. M. Bove, Jr., Q. Dai, R. Raskar, and G. Wetzstein, "Towards BxDF Display Using Multilayer Diffraction," *ACM Transactions on Graphics (Proc. SIGGRAPH Asia 2014)*, vol. 33, no. 6, 2014.

[102] T. D. Gerke and R. Piestun, "Aperiodic computer-generated volume holograms improve the performance of amplitude volume gratings," *Optics Express*, vol. 15, no. 23, p. 14954, 2007.

[103] T. D. Gerke and R. Piestun, "Aperiodic volume optics," *Nature Photonics*, vol. 4, pp. 188 - 193, 2010.

[104] M. Born and E. Wolf, *Principles of Optics*. 7th edition. Cambridge University Press, 1999.

[105] S. Jolly, E. Dreshaj, and V. M. Bove, Jr., "Computation of Fresnel holograms and diffraction-specific coherent panoramagrams for full-color holographic displays based on anisotropic leaky-mode modulators," *Proc. SPIE Practical Holography XXIX*, 9386, 2015.

[106] W. Lee and F. L. Degertekin, "Rigorous coupled-wave analysis of multilayered grating structures," *Journal of Lightwave Technology*, 22(10), 2004.

[107] A. Tunnermann, B. Wellegehausen, B. N. Chichkov, C. Momma, H. Jacobs, H. Welling, and S. Nolte, "Ablation of metals by ultrashort laser pulses," *Journal of the Optical Society of America B*, vol. 14, no. 10, pp. 2716-2722, Oct. 1997.